

Techniques of deconvolution, interpolation and super-resolution for high-resolution image reconstruction

Chen, Li

2006

Chen, L. (2006). Techniques of deconvolution, interpolation and super-resolution for high-resolution image reconstruction. Doctoral thesis, Nanyang Technological University, Singapore.

<https://hdl.handle.net/10356/3491>

<https://doi.org/10.32657/10356/3491>

Nanyang Technological University

Downloaded on 13 Mar 2024 15:53:48 SGT



**NANYANG
TECHNOLOGICAL
UNIVERSITY**

**TECHNIQUES OF DECONVOLUTION,
INTERPOLATION, AND SUPER-RESOLUTION
FOR HIGH-RESOLUTION IMAGE
RECONSTRUCTION**

CHEN LI

SCHOOL OF ELECTRICAL & ELECTRONIC ENGINEERING

2006

Techniques of Deconvolution, Interpolation, and Super-Resolution for High-Resolution Image Reconstruction

Chen Li

School of Electrical & Electronic Engineering

A thesis submitted to the Nanyang Technological University
in fulfilment of the requirement for the degree of
Doctor of Philosophy

2006

Statement of Originality

I hereby certify that the work embodied in this thesis is the result of original research and has not been submitted for a higher degree to any other University or Institution.

DATE

CHEN LI

To my family, for all your love.

Acknowledgements

I have had the pleasure of pursuing my postgraduate study and research under the guidance and direction of Assistant Professor Kim-Hui Yap, my supervisor, from whose intuition, wisdom, and constant encouragement I have greatly benefited. He is my role model, inside and outside of academics. Especially, I would like to convey my deepest gratitude for the freedom provided by him, which have made this work interesting and possible.

I would like to thank my parents, my brother, and all the members in my family for encouraging me to understand the value of hard work and supporting me during the last four years as well as the whole life. Their endless love and unselfish care are always the greatest inspiration for me from the first day I came to this colorful world. Special thanks to my girlfriend, a caring and supportive partner always.

I also would like to thank all of my colleagues in the Media Technology Laboratory (MTL) at the Nanyang Technological University. The staff in MTL has made it a joy for me to work in the lab every day. I learned a lot from our discussions and will cherish the friendship forever.

I dedicate this thesis to all of you.

Summary

This thesis investigates how to produce a high quality, high-resolution image from low quality, low-resolution images. In many visual applications, high quality images are desired but may fail to be obtained because of some degradation factors. Several images, which suffer from the degradations but consist of the overlapping content of a scene, are used to produce a single image of superior quality. Using high-resolution reconstruction, it is possible to restore high-frequency content, reduce noise, and even increase spatial resolution when hardware modification is unrealizable.

The generic name of high-resolution image reconstruction covers related subjects of deconvolution, interpolation, and super-resolution. Image deconvolution mainly deals with deblurring from blurred and noisy images, while the major goal of interpolation and super-resolution is to increase spatial resolution from the aliased images.

In the first part, a series of algorithms are proposed to solve different problems encountered in blind image deconvolution. In Chapter 2, several efficient discrete spatial techniques for blur support identification are derived and analyzed. A soft modeling algorithm is proposed to generate the manifold parametric blur models and determine the final blur estimate in Chapter 3. We attempt to address blind deconvolution by assessing the relevance of parametric blur information, and incorporating the knowledge into the parametric double regularization scheme. Further, an iterative algorithm based on multichannel recursive filtering is proposed to address multichannel image deconvolution.

In the second part, the image interpolation is formulated as a regularized least squares

solution of a cost function. It is processed as a whole-matrix computation rather than pixel-to-pixel estimation individually. The regularized least squares can achieve a well trade-off between edge preservation and noise suppression. We derive the optimal solution using a combined framework of Kronecker product and singular value decomposition to reduce the computational cost greatly.

The last part of this thesis deals with image resolution enhancement from several low-resolution observations. It includes subpixel registration in Chapter 6 and super-resolution in Chapter 7. For subpixel registration, a major shortcoming of conventional techniques is its sensitivity towards noise. The proposed bispectrum algorithm utilizes the characteristics of higher-order statistics to suppress Gaussian noise. A novel blind super-resolution algorithm is developed to enhance image resolution. The main contribution is the development of multichannel blind deconvolution to estimate the unknown point spread functions, and its integration into the super-resolution scheme to render high-resolution images.

The algorithms presented in this thesis can serve as foundation for further work. The future of high-resolution image reconstruction technology appears to be very bright, although much work remains to be done for it to reach a mature technology.

Key Abbreviations

1-D	One-dimensional
2-D	Two-dimensional
AM	Alternating minimization
AR	Autoregressive
ARMA	Autoregressive moving-average
AWGN	Additive white Gaussian noise
BCCB	Block-circulant circulant-block
BTTB	Block-Toeplitz Toeplitz-block
CCD	Charged-coupled device
CFT	Continues Fourier transform
CGO	Conjugate gradient optimization
CRLB	Cramer-Rao lower bound
DFT	Discrete Fourier transform
GCV	Generalized cross-validation
HR	High-resolution
IDFT	Inverse discrete Fourier transform
ITP	Iterative threshold pruning
K-NN	K -nearest-neighbor
LR	Low-resolution
MA	Moving-average
MAAD	Maximum average absolute difference
MAP	Maximum <i>a posteriori</i>
MASD	Maximum average square difference
MCSC	Minimum cyclic-shift correlation
MRF	Multichannel recursive filtering
MSPM	Manifold soft parametric modeling
PDR	Parametric double regularization
POCS	Projection-onto-convex-sets

PSF	Point-spread function or blur
PSNR	Peak signal-to-noise ratio
SDR	Symmetric double regularization
SIMO	Single-input multiple-output
SISO	Single-input single-output
SNR	Signal-to-noise ratio
SR	Super-resolution
SVD	Singular value decomposition
TV	Total variation

Key Symbols

For conciseness, the notation f , g and h are often used in this thesis to denote the original image, the degraded image, and the PSF, respectively. In matrix-vector equation, f and g represent lexicographically ordered column vector of the original image and the degraded image, respectively. For ease of notation, we omit the cap “ $\hat{}$ ” for the estimated variable in some chapters.

a, A	AR model, corresponding AR matrix
c, C	Regularization operator for image, corresponding regularization matrix
d, D	Decimation factor along the X- and Y-axis, corresponding decimation matrix
e, E	Regularization operator for PSF, corresponding regularization matrix
e_i	Regularization operator for the i th channel PSF
f	Original image or estimated HR image
$f^{(i)}$	Estimated image in the i th iteration
$f_{(m,n)}, \mathcal{F}$	Circularly shifted original image by $\text{shiftsize}(m,n)$, corresponding stacked array
g, g_i	Degraded image, degraded image in the i th channel
$g_{(m,n)}, \mathcal{G}$	Circularly shifted degraded image by $\text{shiftsize}(m,n)$, corresponding stacked array
h, H, \tilde{H}	PSF, corresponding PSF matrix, corresponding 2-D DFT
h_i, H_i	PSF in the i th channel or the i th K -NN, corresponding PSF matrix
$h^{(i)}$	Estimated PSF in the i th iteration
h_p	Parametric PSF estimate in MSPM
K	Number of degraded images or channels or nearest neighbors in K -NN
n, n_i	Noise, noise in the i th channel
$S_f : M \times N$	Size of degraded image

$S_h : P \times Q$	Support size of PSF
s_i, \mathbf{S}_i	Geometric warping vector in the i th channel, corresponding warping matrix
λ	Forgetting factor in MRF
$\alpha_i, \beta_i, \gamma_i$	Regularization parameters
$\mathbf{A}, \mathbf{\Psi}, \mathbf{\Gamma}$	Diagonal regularization matrices constructed from $\alpha_i, \beta_i, \gamma_i$
$\omega = (\omega_x, \omega_y)$	Frequency pair along the X - and Y -axis
$J(\mathbf{f}, \mathbf{h})$	Joint image and blur cost function
$J(\mathbf{f} \mathbf{h})$	Image-domain cost function
$J(\mathbf{h} \mathbf{f})$	Blur-domain cost function
$(\cdot)^H$	Hermitian transposition
$*$	2-D convolution
\otimes	Kronecker product
$tr(\cdot)$	Trace of a matrix
$diag(\cdot)$	Diagonal matrix
$vec(\cdot)$	Concatenating the columns of a matrix into a vector
$ivec(\cdot)$	Inverse process of rehashing the vector into the matrix
$\mathcal{F}[\cdot]$	DFT operation
$E[\cdot]$	Expectation
$\ \cdot\ $	L_2 -norm

Table of Contents

Acknowledgements	i
Summary	ii
Key Abbreviations	iv
Key Symbols	vi
List of Figures	xi
List of Tables	xiv
1 Introduction	1
1.1 Motivation.....	1
1.2 Objectives.....	4
1.2.1 Deconvolution	4
1.2.2 Interpolation	7
1.2.3 Super-Resolution	8
1.3 Contributions of Thesis	11
1.4 Organization of Thesis	13
2 Blur Support Identification for Deconvolution	15
2.1 Introduction.....	15
2.2 Literature Review.....	17
2.3 Preliminaries and Notations	20
2.3.1 ARMA Image Model.....	20
2.3.2 Kronecker Product.....	22
2.3.3 Characteristics of PSF	23
2.3.4 Cyclically Shifted Image.....	23
2.4 Discrete Spatial Techniques	24
2.5 AR Image Model Estimation	28
2.6 Experimental Results	30
2.6.1 Blur Support Identification of 2-D PSF.....	30
2.6.2 Image Restoration Using Various PSF Support Sizes	32
2.6.3 Blur Support Identification under Noisy Condition	33
2.6.4 Comparison with Other Blur Support Identification Methods.....	36
2.6.5 Blur Support Identification for Infinite- or Large-Support PSF.....	37
2.7 Summary	40

2.8	Appendix	40
3	Parametric Double Regularization Approach for Deconvolution	42
3.1	Introduction	42
3.2	Literature Review	43
3.3	Development of Cost Function	46
3.4	Manifold Soft Parametric Modeling	48
3.4.1	Nearest Neighbors Generation	49
3.4.2	Fuzzy Membership Estimation	51
3.4.3	Weighted Mean Filtering	52
3.5	Optimization Procedure	53
3.5.1	Minimization of Blur-Domain Cost Function	56
3.5.2	Minimization of Image-Domain Cost Function	57
3.6	Experimental Results	58
3.6.1	Blind Deconvolution of Image Degraded by a Uniform PSF	59
3.6.2	Blind Deconvolution of Image Degraded under Noisy Conditions	60
3.6.3	Blind Deconvolution of Image Degraded by Different PSFs	63
3.6.4	Blind Deconvolution of Real-Life Blurred Image	66
3.7	Summary	66
4	Multichannel Recursive Filtering for Deconvolution	68
4.1	Introduction	68
4.2	Literature Review	69
4.3	Development of Cost Function	71
4.4	Recursive Filtering for Multichannel Blind Deconvolution	73
4.4.1	Multichannel Recursive Filtering	73
4.4.2	Blur Identification	76
4.4.3	Schematic Overview	77
4.5	Issues on MRF Parameters	79
4.5.1	Regularization Parameters and Operators	79
4.5.2	Forgetting Factor	80
4.6	Experimental Results	81
4.6.1	Multichannel Blind Deconvolution under Noisy Conditions	81
4.6.2	Comparison with Other Multichannel Deconvolution Methods	84
4.7	Summary	86
4.8	Appendix A	86
4.9	Appendix B	88
5	Regularized Interpolation Using Kronecker Product	91
5.1	Introduction	91
5.2	Literature Review	93
5.3	Interpolation Model	95
5.4	Regularized Interpolation Using Kronecker Product	96
5.4.1	Kronecker Product of Matrices	97
5.4.2	Least Squares Minimization	98
5.4.3	Regularization Issue	99
5.5	Experimental Results	100
5.5.1	Comparison with Other Interpolation Methods	100

5.5.2	Effects of Regularization Parameter.....	103
5.5.3	Computational Complexity Reduction.....	104
5.6	Summary.....	104
5.7	Appendix.....	105
6	Bispectrum Subpixel Registration	108
6.1	Introduction.....	108
6.2	Literature Review.....	109
6.3	Problem Formulation.....	112
6.3.1	Subpixel Translation Estimation.....	112
6.3.2	Noise Effect.....	113
6.4	Subpixel Registration under Noisy Conditions.....	114
6.4.1	Proposed Cross Bispectrum Method.....	114
6.4.2	Complexity Reduction.....	118
6.5	Experimental Results.....	119
6.5.1	Image Degraded By AWGN.....	120
6.5.2	Image Degraded by Cross-Correlated Noise.....	121
6.5.3	Image Registration for Pixel and Subpixel Translations.....	122
6.6	Summary.....	123
6.7	Appendix.....	124
7	Blind Multiframe Super-Resolution	125
7.1	Introduction.....	125
7.2	Literature Review.....	126
7.3	Spatial-Domain Super-Resolution.....	129
7.4	Blind Multiframe Super-Resolution Scheme.....	131
7.4.1	Joint Interpolation-Restoration Framework.....	131
7.4.2	Channel Blur Identification.....	135
7.4.3	Recursive Multichannel Image Restoration.....	137
7.5	Experimental Results.....	137
7.5.1	Super-Resolution of Simulated Images.....	137
7.5.2	Super-Resolution of Real-Life Images.....	139
7.6	Summary.....	143
8	Conclusion and Recommendations	144
8.1	Conclusion.....	144
8.1.1	Image Deconvolution.....	144
8.1.2	Image Interpolation.....	146
8.1.3	Image Super-Resolution.....	146
8.2	Recommendations for Further Research.....	147
8.2.1	High-Resolution Reconstruction for Color Image.....	147
8.2.2	High-Resolution Reconstruction for Medical Imaging.....	148
8.2.3	Super-Resolution Considering Dynamic Scenes.....	149
8.3	Summary.....	150
	Author's Publications	151
	Bibliography	154

List of Figures

Figure 1.1 The effects of various imaging degradations. (a) Original image, (b) Blurred image, (c) Aliased and downsampled image, (d) Noisy image.....	2
Figure 1.2 Ultrasonic image of a fetus in uterus.	3
Figure 1.3 Image blurring process for deconvolution.	5
Figure 1.4 Illustration of image blurring. (a) Original image, (b) Gaussian PSF, (c) Blurred image.	6
Figure 1.5 Image degradation process for interpolation.	8
Figure 1.6 Super-resolution image reconstruction of a license plate.	9
Figure 1.7 Suspected terrorist in the failed bomb attacks in London on July 21,2005.	9
Figure 1.8 Image degradation process for super-resolution.....	10
Figure 2.1 Gaussian PSF (support size 5×5 , standard variance $\sigma = 2.5$). (a) Spatial profile, (b) Log-power spectrum.....	16
Figure 2.2 Blur support identification of 2-D PSF. (a) Original “Flower” image, (b) 2-D Gaussian PSF (size 7×7 , $\sigma = 3.2$), (c) Image degraded by Gaussian PSF, (d) MCSC, MASD and MAAD profiles in the vertical direction, (e) MCSC, MASD and MAAD profiles in the horizontal direction.	31
Figure 2.3 Blur support identification under 30dB noise level. (a) Original “Lena” image, (b) 2-D uniform PSF (size 5×7), (c) Image degraded by uniform PSF, (d) MCSC, MASD and MAAD profiles in the vertical direction, (e) MCSC, MASD and MAAD profiles in the horizontal direction.	34
Figure 2.4 Blur support identification of 2-D PSF. (a) Original “Woman” image, (b) 2-D	

uniform PSF (size 9×9), (c) Image degraded by uniform PSF, (d) MCSC, MASD and MAAD profiles in the vertical direction, (e) MCSC, MASD and MAAD profiles in the horizontal direction.	35
Figure 2.5 Different PSFs. (a) 2-D Gaussian PSF (size 5×5 , $\sigma = 3.0$), (b) 2-D Gaussian PSF (size 7×7 , $\sigma = 3.5$), (c) 2-D uniform PSF (size 7×9).	36
Figure 2.6 Blind deconvolution of image degraded by a PSF with large blur support size. (a) Original “Lena” image, (b) Gaussian mixture PSF, (c) Image degraded by PSF, (d) MCSC, MASD and MAAD profiles in the vertical direction, (e) MCSC, MASD and MAAD profiles in the horizontal direction, (f) 5×5 , (g) 5×7 , (h) 7×7 , (i) 7×9 , (j) 9×9 , (k) 11×11 , (l) 13×13 , (m) 15×15	39
Figure 3.1 Image blurring model and deconvolution process.	42
Figure 3.2 Manifold soft parametric modeling blur estimator.	49
Figure 3.3 Overview of parametric double regularization scheme.	55
Figure 3.4 Blind deconvolution of image degraded by a uniform PSF. (a) Original image, (b) Degraded Image, (c) PDR restored image, (d) SDR restored image, (e) MCSC, MASD and MAAD profiles in the vertical direction, (f) MCSC, MASD and MAAD profiles in the horizontal direction.	61
Figure 3.5 Blind deconvolution of image degraded by a Gaussian PSF with additive noise. (a) Original image, (b) Degraded Image, (c) PDR restored image, (d) SDR restored image.	62
Figure 3.6 Examples of blind image deconvolution results. (a) Original image, (b) Degraded image, (c) Restored image.	64
Figure 3.7 Blind deconvolution of real-life image. (a) Naturally blurred Image, (b) PDR restored image, (c) SDR restored image, (d) MCSC, MASD and MAAD profiles in the vertical direction, (e) MCSC, MASD and MAAD profiles in the horizontal direction.	65
Figure 4.1 Multichannel blurring model.	68
Figure 4.2 Schematic diagram of the proposed algorithm.	78

Figure 4.3 Multichannel blind image deconvolution results. (a) Original “Board” image, (b) A sampled blurred image out of the four degraded images, (c) Restored image using the proposed MRF algorithm, (d) The profile of PSNR versus the number of iterations.	83
Figure 4.4 Comparison of different deconvolution results in 30dB noise environment. (a) Original “Satellite” image, (b) One of the three degraded images, (c) Restored image using the proposed MRF algorithm, (d) Restored image using the SDR-AM algorithm, (e) Restored image using the TV-AM algorithm.	85
Figure 5.1 The relationship between HR and LR pixels.	92
Figure 5.2 Test Images. (a) “Lena” image, (b) “F16” image, (c) “Boat” image.	102
Figure 5.3 Enlarged sections of interpolated images under 40dB noise. (a) Low-resolution images, (b) Lagrange method, (c) Bicubic method, (d) Proposed method.	102
Figure 6.1 Two images of the same scene. (a) Reference image, (b) Shifted and rotated image.	109
Figure 6.2 Schematic diagram of the proposed algorithm.	119
Figure 6.3 Test Images. (a) “Pentagon” image, (b) “Castle” image, (c) “NTU” image.	120
Figure 7.1 Basic model for super-resolution.	126
Figure 7.2 Blind super-resolution image reconstruction results. (a) Original “Satellite” image, (b) Four LR images, (c) One of the upsampled LR frames, (d) Proposed algorithm, (e) Bicubic interpolation, (f) IBP method.	140
Figure 7.3 Blind super-resolution image reconstruction results. (a) Original “Singapore” image, (b) Section of LR frames, (c) One of the upsampled LR frames, (d) Proposed algorithm, (e) Bicubic interpolation, (f) IBP method.	141
Figure 7.4 Blind super-resolution image reconstruction results. (a) One of LR frame, (b) Section of LR frame, (c) Upsampled section, (d) Reconstruction result.	142

List of Tables

Table 2.1 Comparison of restored images with different support sizes	33
Table 2.2 Blur support identification by different methods	36
Table 2.3 Image deconvolution for large-support PSF.....	38
Table 3.1 Blind image deconvolution results	63
Table 4.1 Summary of conjugate gradient optimization for blur identification.....	77
Table 4.2 Comparison of different deconvolution algorithms	85
Table 5.1 Comparison of different interpolation methods in PSNR	103
Table 5.2 Comparison of different regularization parameters in PSNR.....	103
Table 6.1 Results of subpixel registration in AWGN	121
Table 6.2 Results of subpixel registration in correlated noise.....	122
Table 6.3 Results of pixel and subpixel registration	123
Table 7.1 Results of subpixel registration	143

Chapter 1

Introduction

1.1 Motivation

Nowadays, digital imaging devices are growing in popularity for image acquisition ranging from consumer electronics to industrial equipments. Digital images are made up of numerous pixels, which are tiny light-sensitive grids arranged in a matrix plane. Spatial resolution is a term that refers to the number of pixels utilized in construction of a digital scene. Broadly speaking, images with higher resolution should not only have higher spatial density of pixels, but also be visually sharper and clearer than those with lower resolution.

In many visual applications, high quality images are desired but may fail to be obtained because of some degradation factors. Blurring, noise, bandwidth limitation, quantization and frequency aliasing are common degradations found in imaging systems. The common web camera, for example, is an economic low-resolution (LR) video device, which records the scene in Figure 1.1(a) and implements real-time video communication over Internet. When the image experiences optical out-of-focus, relative motion between object and camera, and low bit rate video coding, the effect of blurring can be observed in Figure 1.1(b). During spatial sampling of the continuous scene, the highest spatial frequency is limited by the resolution of its imaging optics and transducer. This may potentially produce the aliased and downsampled image in Figure 1.1(c). Moreover, the imaging sensor array, usually the

charged-coupled device (CCD), is subject to various noise sources including the thermal and shot noise. The noisy effect is particularly evident under the environment of low lighting, as shown in Figure 1.1(d).

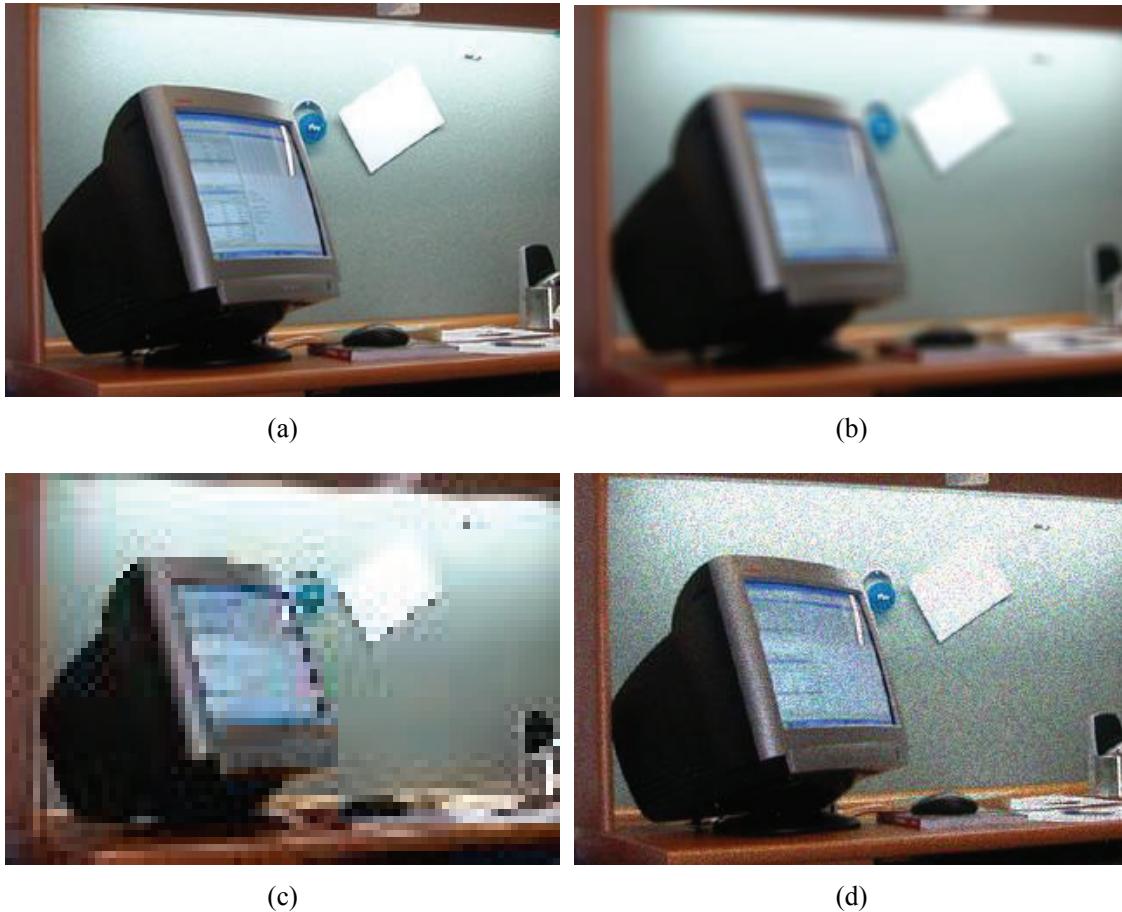


Figure 1.1 The effects of various imaging degradations. (a) Original image, (b) Blurred image, (c) Aliased and downsampled image, (d) Noisy image.

This thesis investigates how to produce a high quality, high-resolution (HR) image from low quality, low-resolution (LR) images. Several images, which suffer from the aforementioned degradations but consist of the overlapping content of a scene, are used to produce a single image of superior quality. This is known as HR image reconstruction that covers related subjects of deconvolution, interpolation, and super-resolution (SR). Image deconvolution

mainly deals with deblurring from blurred and noisy images, while the major goal of interpolation and SR is to increase spatial resolution from the aliased images.

Using HR reconstruction, it is possible to restore high-frequency content, reduce noise, and even increase spatial resolution when hardware modification is unrealizable. The ultrasound imaging, for example, is one of the most widely used imaging modality in the clinical examination. The resolution of ultrasonic image is not only limited by the dimensions of the sound beam from the acoustic aperture but also degraded by the speckle noise. Figure 1.2 illustrates one ultrasonic image of a fetus. Enhancing ultrasonic resolution can increase the accuracy of diagnostic decisions, and lessen the burden of well-trained radiographers as well. However, due to economic cost or physical limit, image quality cannot be improved by replacing the imaging hardware in some practical situations. HR image reconstruction using software is an appealing inexpensive alternative.



Figure 1.2 Ultrasonic image of a fetus in uterus.

1.2 Objectives

The aim of this thesis is to develop efficient, robust and automated HR reconstruction algorithms, which are useful for real-life applications. HR image reconstruction from low quality, LR images is one of the most intriguing challenges in image processing. It is a broad research area that covers image deconvolution, interpolation, and SR. It distinguishes itself from image enhancement in that it is based on models for the degradation process. The general mathematical model for the degradation process is

$$\mathbf{g}_i = \mathbb{C}_i \mathbf{f} + \mathbf{n}_i, \quad i = 1, 2, \dots, K \quad (1.1)$$

where K is the number of observed degraded images. \mathbf{f} , \mathbf{g}_i , \mathbf{n}_i denote the original image, the i th channel degraded image, and the noise, respectively. \mathbb{C}_i is the system matrix that represents relationship between the original image and degraded image.

Image reconstruction is an inverse process that attempts to estimate the original image from the degraded images. The problem can be mathematically stated as given \mathbf{g}_i , find a best estimate of \mathbf{f} , according to some optimality criteria. A key feature in this formulation is the assumption of a blind situation, where no knowledge of \mathbb{C}_i , e.g. optics parameters, relative motion, atmosphere turbulence, is assumed to be known *a priori*. It is a difficult ill-posed inverse problem as the uniqueness and stability of the solutions is not guaranteed [1]-[4].

1.2.1 Deconvolution

Image restoration, also known as image deconvolution, began primarily with the efforts of scientists involved in the *Space Race* between the United States and the former Soviet Union in the 1960s. The astronomical images obtained from the satellites were mainly blurred for

some reasons such as out-of-focus optics, spinning and tumbling of spacecraft, and atmospheric turbulence [1], [2]. In such situations, the relationship \mathbb{C}_i between the original image and degraded image can be modeled by a two-dimensional (2-D) filter, commonly referred to as blur or point-spread function (PSF). This leads to the following linear shift-invariant blurring model:

$$\begin{aligned} g(x, y) &= h(x, y) * f(x, y) + n(x, y) \\ &= \sum_{(m,n) \in S_h} h(m, n) f(x - m, y - n) + n(x, y) \end{aligned} \quad (1.2)$$

where $*$ stands for 2-D convolution. $f(x, y)$, $g(x, y)$, and $n(x, y)$ represent the original image, degraded image, and the additive noise, respectively. $h(x, y)$ and S_h denote the PSF and its support size.

Figure 1.3 illustrates the flowchart of the blurring process, where the original image is convoluted by PSF and degraded by noise to give the blurred image. The original image in Figure 1.4(a) displays a “Satellite” in the space. Figure 1.4(b) shows the shape of a Gaussian PSF. The degraded image in Figure 1.4(c) is produced by convoluting the original image with the PSF at 30dB noise level. It can be observed that a certain degree of detail information has been lost in the blurred image.

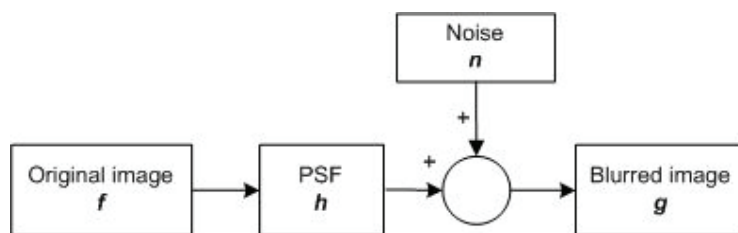


Figure 1.3 Image blurring process for deconvolution.

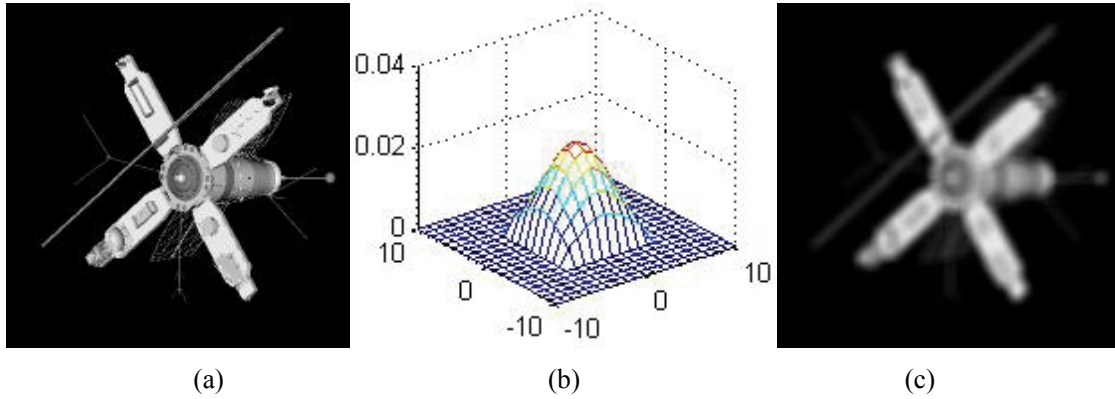


Figure 1.4 Illustration of image blurring. (a) Original image, (b) Gaussian PSF, (c) Blurred image.

The linear image degradation processes in (1.2) can be expressed in a matrix-vector formation:

$$\mathbf{g} = \mathbf{H}\mathbf{f} + \mathbf{n} \quad (1.3)$$

where \mathbf{f} , \mathbf{g} , and \mathbf{n} represent the lexicographically ordered column vectors of the original image, the blurred image, and the noise, respectively. \mathbf{H} is the matrix constructed from PSF \mathbf{h} .

Image deconvolution is an inverse process that attempts to deconvolute the blurred and noisy images to recover the original scene. Nevertheless, classical deconvolution needs the information of PSF, which is not available in many practical applications. Therefore, this motivates the studies of blind deconvolution where the primary objective is to estimate both the original image and PSF from the degraded image given little or no prior knowledge about the imaging system.

Due to the following reasons, blind image deconvolution is a difficult ill-posed inverse problem that the uniqueness and stability of the solutions is not guaranteed, i.e. (i) a trivial perturbation in \mathbf{g} can produce non-trivial perturbations in the restored image because the condition number of \mathbf{H} is large, (ii) a solution may not exist because the smallest eigenvalue of \mathbf{H} may equal or approach zero, and (iii) more than one solution may exist because \mathbf{H} is

unknown.

Conventional blind deconvolution methods only consider single-input single-output (SISO) model of (1.3). However, these are fundamentally limited by the inherent loss of information in single observation. A recent trend focuses on single-input multiple-output (SIMO) model:

$$\mathbf{g}_i = \mathbf{H}_i \mathbf{f} + \mathbf{n}_i, \quad i = 1, 2, \dots, K \quad (1.4)$$

The recovery of the original scene from its multiple observations is referred to as multichannel blind image deconvolution. By combining multiple observations of the same scene, the information lost in one channel may be compensated by the other channel. Therefore, the quality of the restored image through SIMO model is usually better than that of the SISO model.

1.2.2 Interpolation

To enlarge the image by increasing spatial resolution, the missing pixel information must be estimated from the surrounding pixels of the observed LR images. This problem is commonly referred to as image interpolation when only single LR image is available, or super-resolution (SR) when multiple LR images are available.

Image interpolation or image resizing are commonly used in digital photography. The interpolation model is similar to that of classical image deconvolution in (1.3) except for the additional decimation process:

$$\mathbf{g} = \mathbf{D}\mathbf{H}\mathbf{f} + \mathbf{n} \quad (1.5)$$

where \mathbf{H} represents the low-pass filtering process during the sensor array sampling. \mathbf{D} is the sampling matrix constructed from the decimation processes with the decimation rate d . \mathbf{g} and

f represent the observed image with size $M \times N$, and the desired original image with size $dM \times dN$.

Figure 1.5 illustrates the imaging process for interpolation. The task of interpolation is to recover the lost high-frequency information during the sampling process from only one available LR image.



Figure 1.5 Image degradation process for interpolation.

1.2.3 Super-Resolution

SR is the task of estimating HR images from a set of aliased, low quality LR images of the same scene. These LR observations are acquired either by multiple sensors imaging a single scene or using a single sensor capturing the scene over a period of time. SR is an active research area at present and has wide applications. For instance, a clear license plate image can be reconstructed from a video sequence in closed-circuit television (CCTV) system in Figure 1.6. Another important application in real-life is shown in Figure 1.7. After the failed bomb attacks in London on July 21, 2005, a CCTV image of the bomb suspect is issued by Scotland Yard [5]. If the technology of SR can successfully produce the suspect's frontal face, not only can it improve quality of surveillance but also reduce the cost of the camera hardware. Therefore, the major advantage of SR is that it is less costly than either improving the existing imaging systems or overcoming the physical resolution limitation that cannot be

achieved even by replacing the imaging hardware.

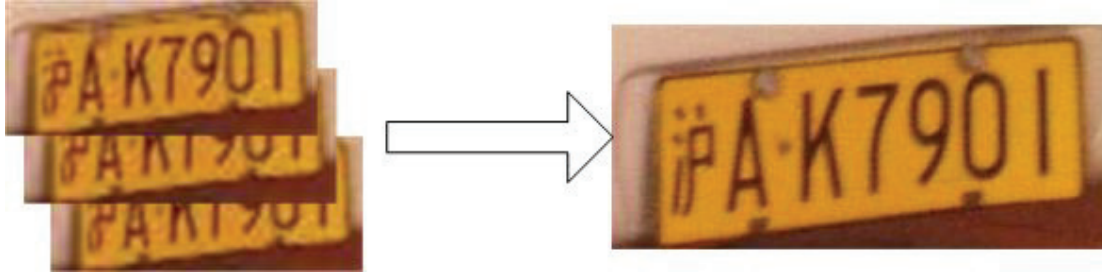


Figure 1.6 Super-resolution image reconstruction of a license plate.



Figure 1.7 Suspected terrorist in the failed bomb attacks in London on July 21, 2005.

Consider the general SR model that consists of K measured LR images, which are related to the desired HR image through a series of mappings comprising geometric warping (i.e. translation, rotation), blurring, and decimation, together with potential additive noise. The i th LR image can be modeled as:

$$\mathbf{g}_i = \mathbf{D}_i \mathbf{H}_i \mathbf{S}_i \mathbf{f} + \mathbf{n}_i, \quad i = 1, 2, \dots, K \quad (1.6)$$

where \mathbf{S}_i stands for the i th channel geometric warping by warping parameters \mathbf{s}_i .

Figure 1.8 illustrates the image degradation process for SR, which can be considered as

multichannel interpolation problem with additional warping process.

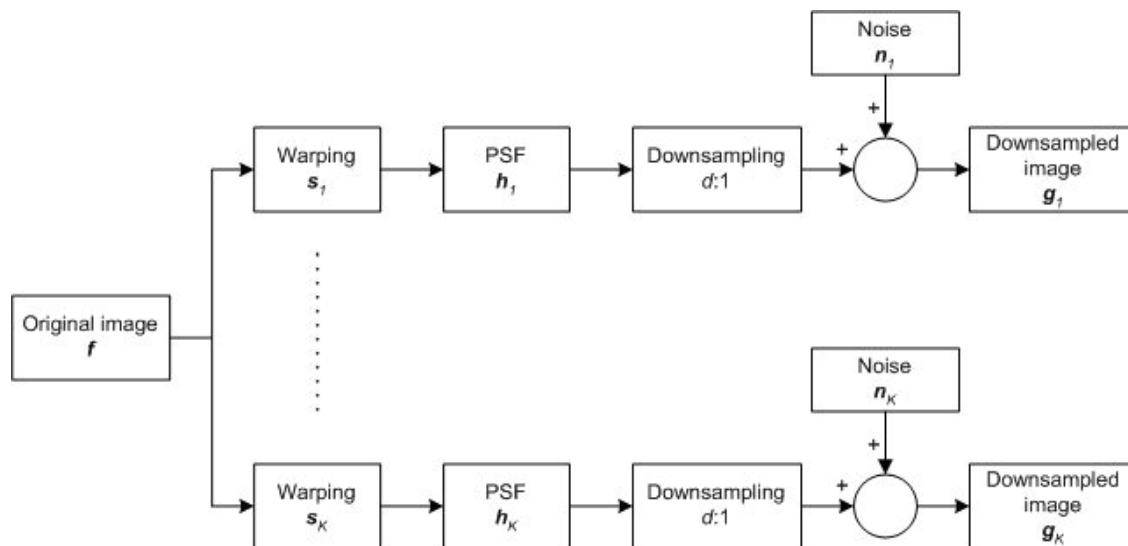


Figure 1.8 Image degradation process for super-resolution

The SR methodology contains two major components of image registration and data fusion. The objective of image registration is to identify the pixel-to-pixel and subpixel-to-subpixel mapping between LR images in their overlapping region. All the warping information retrieved by registration, including translations, rotation angle, and scaling factor, are used to fuse the original image in the data fusion step. Image fusion is closely related to restoration that should have proper balance between image detail recovery and noise suppression. Currently, there are relatively few works on blind SR image reconstruction. In other words, they assume that the PSFs are known *a priori*, which is not practical in many real-world applications. Therefore, it is necessary to incorporate blur identification into the SR image reconstruction.

Overall, a related problem to SR technologies is image deconvolution, which is to recover a blurred image, but does not increase the resolution. Another problem related to SR is image

interpolation that is to increase spatial resolution, but from a single image. For HR image reconstruction, SR is a more sophisticated technique which aims to restore poor quality image sequences by modeling and removing the degradations inherent in the imaging process, such as noise, blur and spatial-sampling.

1.3 Contributions of Thesis

The main contributions of this thesis are development of a set of complete and novel HR image reconstruction techniques, which cover image deconvolution, interpolation, and super-resolution. All the algorithms are developed towards HR image reconstructions along the way. For each respective topic, we develop efficient algorithms in theory and verify them by simulation.

In Chapter 2, we present several discrete spatial techniques for identifying blur support in blind image deconvolution. Blur identification is a challenging problem in blind image deconvolution. In particular, if the blur support can be estimated reliably in the beginning of deconvolution, the computational cost of many blind deconvolution schemes can be reduced significantly, and their convergence performance will be improved. The proposed techniques are derived from the autoregressive (AR) model of the underlying images. The efficiency and validity of the techniques are also analyzed.

In Chapter 3, a novel blind image deconvolution scheme based on soft integration of parametric blur structures is proposed. We attempt to address blind deconvolution by assessing the relevance of parametric blur information, and incorporating the knowledge into the parametric double regularization (PDR) scheme. The PDR method assumes that the actual blur satisfies up to a certain degree of parametric structure, as there are many well-known

parametric blurs in practical applications. Further, it can be tailored flexibly to include other blur types if some prior parametric knowledge of the blur is available. A manifold soft parametric modeling (MSPM) technique is proposed to generate the blur manifolds and estimate the fuzzy blur structure.

Chapter 4 presents a novel multichannel recursive filtering (MRF) technique to address multichannel blind image deconvolution. The primary motivation for developing the MRF algorithm is due to its fast convergence in joint blur identification and image deconvolution. The estimated image is recursively updated from its previous estimates, while the multichannel blurs are identified iteratively using conjugate gradient optimization (CGO).

Chapter 5 deals with a new and efficient algorithm for image interpolation based on regularization theory. To render a HR image from a LR one, classical interpolation techniques estimate the missing pixels from the surrounding pixels based on a pixel-by-pixel basis. In contrast, we formulate the interpolation problem into optimization of a cost function. The cost function consists of a data fidelity term and a regularization functional. The main contribution is the development of an efficient algorithm to solve the regularized least squares problem, which incorporates Kronecker product and singular value decomposition (SVD) to reduce the computational cost of the algorithm.

In Chapter 6, we propose a robust higher-order statistics method to address subpixel image registration. Conventional spectrum techniques employ second-order statistics to estimate subpixel translations between two images. They are, however, susceptible to noise, thereby leading to significant performance deterioration in low signal-to-noise ratio (SNR) environments or in the presence of cross-correlated channel noise. The new bispectrum-based method utilizes the characteristics of bispectrum to suppress Gaussian noise. Experimental results show that the proposed technique provides performance improvement over

conventional power spectrum-based methods under different noise levels and conditions.

Chapter 7 describes a novel blind SR algorithm to enhance image resolution without the knowledge of the PSFs. The primary motivation for developing the blind algorithm is due to the observation that most existing SR methods assume the blurs are known *a priori*, which may not be true in many real-world applications. In view of this, we formulate the SR problem into a new framework of joint interpolation-deconvolution scheme. The main contribution is the development of multichannel blind deconvolution to estimate the unknown PSFs, and its integration into the SR scheme to render HR images.

1.4 Organization of Thesis

The remainder of this thesis is organized as follows:

In Chapter 2, several discrete spatial techniques are presented for identification of PSF support size with theoretical proof.

In Chapter 3, the formulation of PDR for blind image deconvolution is discussed in detail. The MSPM algorithm is proposed to generate the blur manifolds and estimate the fuzzy blur structure.

In Chapter 4, a novel multichannel recursive filtering (MRF) technique is presented to address multichannel blind image deconvolution.

In Chapter 5, we discuss image interpolation from the perspective of HR reconstruction. An efficient image interpolation technique based on regularization theory is developed and compared with other classical interpolation methods.

In Chapter 6, a robust higher-order statistics method to address subpixel image registration is proposed. Its efficiency is illustrated under different noisy environments.

In Chapter 7, we develop a blind SR algorithm to enhance image resolution without the knowledge of the PSFs. The SR problem is formulated into a new framework of joint interpolation-deconvolution scheme.

In Chapter 8, the primary contributions toward efficient HR image reconstruction are summarized. Several possible avenues of future research are discussed in detail.

Chapter 2

Blur Support Identification for Deconvolution

2.1 Introduction

Image blurring is commonly due to causes such as lens defocusing, atmospheric turbulence, optical system aberration, and relative motion. The linear model for the blurred image is described in (1.3) that the original image is convoluted by point-spread function (PSF), followed by additive noise. PSF is the transfer function that is used to characterize the blurring process. The name of PSF comes from the spread distribution when a point light passes through a lens in optical experiment.

Let PSF be a 2-D low pass filter with support size $S_h : P \times Q$. Some standard 2-D PSFs include the uniform and Gaussian blurs:

$$h(x, y) = \begin{cases} 1/a, & (x, y) \in S_h; \\ 0, & \text{otherwise} \end{cases}; \quad h(x, y) = \begin{cases} a \exp(-(x^2 + y^2)/2\sigma^2), & (x, y) \in S_h \\ 0, & \text{otherwise} \end{cases} \quad (2.1)$$

where σ and a are the standard deviation of the Gaussian blur and normalizing constant, respectively. The uniform blur is the 2-D extension of 1-D motion blur, and is characterized completely by its dimension. The Gaussian blur is widely observed in applications such as X-ray imaging, and is difficult to estimate using traditional blur identification approaches.

Figure 2.1(a) shows the spatial profile of a truncated Gaussian PSF with support size 5×5 and standard variance $\sigma = 2.5$.

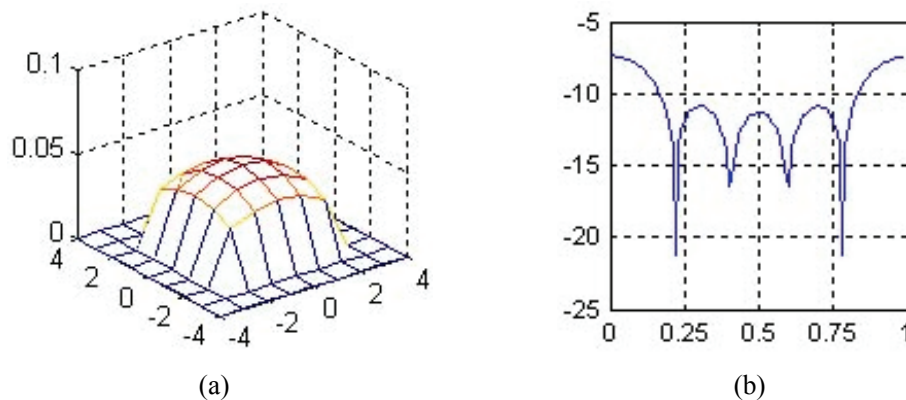


Figure 2.1 Gaussian PSF (support size 5×5 , standard variance $\sigma = 2.5$). (a) Spatial profile, (b) Log-power spectrum.

In most practical settings, the PSF is not known *a priori*, and must be estimated from the degraded image itself. Once the knowledge of the PSF is obtained, one of the existing image restoration techniques such as Wiener filtering and constrained least square (CLS) can then be applied to solve the problem [1]-[4]. Therefore, blur identification is an important issue in blind image deconvolution, involving the identification of the blur support and its coefficients.

Blur support identification is analogous to filter order estimation in signal processing. This chapter will focus on blur support identification because if the blur support can be identified reliably at the beginning of deconvolution, the performance of deconvolution can be improved significantly. The discussion of blur coefficient estimation will be covered in the next chapter.

The rest of this chapter is organized as follows. Section 2.2 reviews the methods for blur support identification. Section 2.3 establishes some notations and concepts to be used in this

chapter. In Section 2.4, the formulations of minimum cyclic-shift correlation (MCSC), maximum average square difference (MASD), and maximum average absolute difference (MAAD) are explained. In Section 2.5, the development of AR estimator is derived and analyzed. Simulation results are presented in Section 2.6. In Section 2.7, conclusions and further remarks are drawn.

2.2 Literature Review

The most straightforward way to identify PSF is by calibrating the camera. This approach is to match with a pre-defined calibration pattern through tuning the physical lens. However, it is complicated and only suitable for particular optics systems, such as astronomical telescope. From this sense, the blur identification using computer software offers an automatic and fast alternative. Most existing software techniques for blur identification do not differentiate between the identification of the blur support S_h and its coefficients $h(x, y)$, because often the first problem implies solving the second, such as maximum likelihood (ML) [6], [7], generalized cross validation (GCV) [8], and residual spectral matching [9]. However, these multivariate estimation approaches require high computational cost and don't guarantee convergence to global minimum. In other cases such as motion blur and out-of-focus blur, knowing the support itself is sufficient for blur identification, because these PSFs have the same coefficient values within the support.

There exist some blind deconvolution approaches that do not need estimation of the blur support explicitly. Nevertheless, these methods avoid this step by either (i) imposing new constraints, or (ii) experiencing inadequate restoration results. For instance, nonnegative and support constraints recursive inverse filtering (NAS-RIF) requires the image object to have a known support and be embedded in a uniform background [25], Greatest common divisor

(GCD) [58] or null-spaced [60] methods require multiple blurred versions of the same scene to be available and the PSFs to be co-prime.

Blur support estimation is analogous to filter order estimation in one-dimensional (1-D) signal processing, albeit the problem is in 2-D spatial domain in this context. In practical settings, if the blur support S_h can be identified reliably at the beginning of deconvolution, the convergence performance of many deconvolution schemes can be improved significantly.

The most popular method to identify the blur support size is the frequency-zero method, which is based on identifying periodic zero-crossings of the blurred image. The discrete Fourier transform (DFT) of (1.3) is

$$\tilde{\mathbf{g}}(\boldsymbol{\omega}) = \tilde{\mathbf{H}}(\boldsymbol{\omega}) \tilde{\mathbf{f}}(\boldsymbol{\omega}) + \tilde{\mathbf{n}}(\boldsymbol{\omega}) \quad (2.2)$$

where superscript “ \sim ” and $\boldsymbol{\omega} = (\omega_x, \omega_y)$ are used to represent the signal in the frequency domain and the frequency pair along the X - and Y -axis, respectively.

Generally speaking, PSF has a smaller support size $S_h : P \times Q$ compared to image size $S_f : M \times N$. Thus, the frequency zeros of PSF are found near the normalized frequency of $\omega_x = (1/P, 2/P, \dots, P-1/P)$ along the X -axis and $\omega_y = (1/Q, 2/Q, \dots, Q-1/Q)$ along the Y -axis. Figure 2.1(b) shows the log-power spectrum $\log(|\tilde{\mathbf{H}}(\boldsymbol{\omega})|^2)$ of the Gaussian PSF in the X -axis direction. It is observed that there are four negative spikes in the Figure 2.1(b), which correspond to the zero-crossings in the frequency domain. Since blurred image is the product of the original image and PSF in frequency domain, the DFT of blurred image is characterized by these periodic zero-crossings, which can be used to identify the blur support. This idea is extended to cepstrum and bispectrum techniques [10], [11]. However, they are sensitive to noise as $\tilde{\mathbf{n}}(\boldsymbol{\omega})$ will obscure the characteristics of zero-crossings. In addition,

these methods are less accurate for the image with rich textures (edges of different intensities and directional textures) because its frequency magnitudes are also rich in terms of zeros or near-zeros.

The spatial-domain methods include Akaike information-theoretic criterion (AIC) [12] and image derivative-based (IDB) method [13]. The AIC identifies the blur support by choosing the optimal solution from a model collection. Therefore, it requires high computational cost. The IDB method is based on autocorrelation of the image derivative. However, the method is restricted to motion blur identification, and the high-pass filter selection does not take underlying image characteristics into consideration. There are other joint blur identification and image deconvolution methods, such as alternating minimization (AM) [14]. AM employs iterative threshold pruning (ITP) to identify the blur support. Starting with an overestimated support, the method proceeds to discard boundary coefficients that have small energy iteratively. Nevertheless, ITP fails to provide robust support identification, as it is sensitive towards the initial support guess and the regularization schemes. In [60], the blind restoration algorithm is based on the assumption that the multichannel PSFs are factor co-prime. Therefore, in the absence of noise, the desired image and PSFs can be transformed into the null-space of a special matrix constructed from the degraded images. The upper bound of the support size can be identified from the rank properties of this null-space matrix. The whole restoration scheme works by first estimating the PSF using a procedure of min-eigenvector, followed by conventional image restoration using the identified PSFs. Nevertheless, the null-spaced method suffers from noise amplification, which often leads to poor solutions in the noisy environments.

In view of this, we develop three discrete spatial techniques, namely minimum cyclic-shift correlation (MCSC), maximum average square difference (MASD), and maximum average

absolute difference (MAAD) estimators to identify the PSF support. The novelty of the proposed methods involves: (i) investigating the practicality of utilizing autoregressive moving-average (ARMA) model in blur support identification, (ii) designing three blur support estimators, which include the development of adaptive filter based on the AR model of the underlying image, (iii) providing analytical studies on the efficiency and validity of the estimators.

Unlike the frequency-domain techniques (cepstrum or bispectrum), the proposed methods do not require the condition that the PSFs must have spectral nulls. On the other hand, when compared to the spatial-domain techniques, the proposed methods are more flexible than the IDB method [13] as the proposed estimators can identify blur support for different blur types other than the motion blur. It is applicable for both single-channel and multi-channel restoration. In short, the main advantages of the proposed methods are their low computational complexity, implementation simplicity, and relative robustness.

2.3 Preliminaries and Notations

2.3.1 ARMA Image Model

Various state-of-the-art image modeling techniques have been studied in different literatures. These include fast unitary transforms (discrete Fourier transform, discrete cosine transform, Walsh-Hadamard transform), Karhunen-Loeve transform, discrete Markov random field, autoregressive and state-space models [15]-[17]. Among them, ARMA model is frequently used in image restoration and blur identification. The practicality and effectiveness of the ARMA in modeling the blurred images in the context of image deconvolution have been demonstrated in many previous works [1]-[4].

The development of a suitable model for images requires a tradeoff between the accuracy of representation and its utility in image identification and restoration. Generally, blurred images exhibit characteristics of low pass smoothing. Therefore, a 2-D moving-average (MA) process is used to represent this low pass filtering effect. On the other hand, the image model uses a 2-D autoregressive (AR) process driven by independent zero-mean white noise (innovation) to model the image formation. Therefore, ARMA modeling of blurred images consists of two parts: AR for image modeling and MA for blur modeling.

The original image is modeled as a 2-D AR process by many researchers in the area of image restoration:

$$f(x, y) = \sum_{(m,n) \in S_a} a(m, n) f(x - m, y - n) + w(m, n) \quad (2.3)$$

where $w(i, j)$ is the additive white Gaussian noise (AWGN) with variance σ_w^2 . $a(x, y)$ and S_a are the AR model coefficients and support, respectively. The AR model in (2.3) can be denoted by a more compact matrix-vector notation as:

$$\mathbf{f} = \mathbf{A}\mathbf{f} + \mathbf{w} \quad (2.4)$$

Let the image be periodic with dimension $M \times N$, \mathbf{f} is a lexicographically ordered column vector of size $MN \times 1$ in (2.4). \mathbf{A} is a block-Toeplitz Toeplitz-block (BTTB) matrix constructed from the AR model. The BTTB matrix is often approximated by the block-circulant circulant-block (BCCB) and given by

$$\mathbf{A} = \begin{bmatrix} \mathbf{A}^{(0)} & \mathbf{A}^{(M-1)} & \cdots & \mathbf{A}^{(1)} \\ \mathbf{A}^{(1)} & \mathbf{A}^{(0)} & \cdots & \mathbf{A}^{(2)} \\ \vdots & \vdots & \ddots & \vdots \\ \mathbf{A}^{(M-1)} & \mathbf{A}^{(M-2)} & \cdots & \mathbf{A}^{(0)} \end{bmatrix}_{MN \times MN}, \quad \mathbf{A}^{(j)} = \begin{bmatrix} a(j, 0) & a(j, N-1) & \cdots & a(j, 1) \\ a(j, 1) & a(j, 0) & \cdots & a(j, 2) \\ \vdots & \vdots & \ddots & \vdots \\ a(j, N-1) & a(j, N-2) & \cdots & a(j, 0) \end{bmatrix}_{N \times N} \quad (2.5)$$

with $\mathbf{A}^{(j)} = \mathbf{A}^{(j-M)}$, $a(j, k) = a(j, k - N)$.

The linear blurring model can be expressed as a 2-D MA process in (1.3), where \mathbf{H} is a BCCB matrix constructed from the PSF with size $MN \times MN$.

$$\mathbf{H} = \begin{bmatrix} \mathbf{H}^{(0)} & \mathbf{H}^{(M-1)} & \cdots & \mathbf{H}^{(1)} \\ \mathbf{H}^{(1)} & \mathbf{H}^{(0)} & \cdots & \mathbf{H}^{(2)} \\ \vdots & \vdots & \ddots & \vdots \\ \mathbf{H}^{(M-1)} & \mathbf{H}^{(M-2)} & \cdots & \mathbf{H}^{(0)} \end{bmatrix}_{MN \times MN}, \mathbf{H}^{(j)} = \begin{bmatrix} h(j,0) & h(j,N-1) & \cdots & h(j,1) \\ h(j,1) & h(j,0) & \cdots & h(j,2) \\ \vdots & \vdots & \ddots & \vdots \\ h(j,N-1) & h(j,N-2) & \cdots & h(j,0) \end{bmatrix}_{N \times N} \quad (2.6)$$

2.3.2 Kronecker Product

Kronecker product between two matrices A and B is an $mp \times nq$ matrix with the block structure [18]:

$$A \otimes B = \begin{bmatrix} a_{11}\mathbf{B} & \cdots & a_{1n}\mathbf{B} \\ \vdots & \ddots & \vdots \\ a_{m1}\mathbf{B} & \cdots & a_{mn}\mathbf{B} \end{bmatrix}_{mp \times nq} \quad (2.7)$$

where $A \in \mathbb{R}^{m \times n}$, $B \in \mathbb{R}^{p \times q}$, and \otimes denotes the Kronecker product.

$$A_{m \times n} = \begin{bmatrix} a_{11} & \cdots & a_{1n} \\ \vdots & \ddots & \vdots \\ a_{m1} & \cdots & a_{mn} \end{bmatrix}_{m \times n}, B_{p \times q} = \begin{bmatrix} b_{11} & \cdots & b_{1q} \\ \vdots & \ddots & \vdots \\ b_{p1} & \cdots & b_{pq} \end{bmatrix}_{p \times q} \quad (2.8)$$

The following properties of Kronecker product will be used throughout the analysis:

$$\begin{aligned} (A \otimes B)^H &= A^H \otimes B^H \\ (A \otimes B)(C \otimes D) &= AC \otimes BD \\ \text{tr}(A \otimes B) &= \text{tr}(A) \cdot \text{tr}(B) \\ (A \otimes B)\mathbf{c} &= \text{vec}(B \text{ ivec}(\mathbf{c}) A^T) \end{aligned} \quad (2.9)$$

where superscript $(\cdot)^H$ denotes Hermitian transposition, and $\text{tr}(\cdot)$ represents the trace of a matrix. $\text{vec}(\cdot)$ denotes concatenating the columns of a matrix into a vector, and $\text{ivec}(\cdot)$ is

the inverse process of rehashing the vector into the matrix.

2.3.3 Characteristics of PSF

We impose the standard unity and non-negativity constraints on the PSF in this work [1]-[4]

$$\sum_{(x,y) \in S_h} h(x,y) = 1; \quad h(x,y) > 0 \quad (2.10)$$

Image blurring is commonly due to causes such as lens defocusing, atmospheric turbulence, and object motion. There are numerous practical settings in which the PSF is separable, i.e.

$$\mathbf{h} = \mathbf{h}_u \mathbf{h}_v^H \quad (2.11)$$

where $\mathbf{h}_u = [u_{-(P-1)/2} \quad \dots \quad u_0 \quad \dots \quad u_{(P-1)/2}]^H$ and $\mathbf{h}_v = [v_{-(Q-1)/2} \quad \dots \quad v_0 \quad \dots \quad v_{(Q-1)/2}]^H$. These include motion blur, uniform blur, sinc-square blur, and Gaussian blur, among others. In the specific event that the PSFs are non-separable, we can employ the technique in [19] to approximate the non-separable PSF using separable PSFs. Under the condition that the PSFs are separable, \mathbf{H} can be decomposed into the Kronecker product of two circulant matrices (\mathbf{H}_u and \mathbf{H}_v) with bandwidth P and Q :

$$\mathbf{H} = \mathbf{H}_u \otimes \mathbf{H}_v = \begin{bmatrix} u_0 & u_{-1} & \cdots & u_1 \\ u_1 & u_0 & \cdots & u_2 \\ \vdots & \vdots & \ddots & \vdots \\ u_{-1} & u_{-2} & \cdots & u_0 \end{bmatrix} \otimes \begin{bmatrix} v_0 & v_{-1} & \cdots & v_1 \\ v_1 & v_0 & \cdots & v_2 \\ \vdots & \vdots & \ddots & \vdots \\ v_{-1} & v_{-2} & \cdots & v_0 \end{bmatrix} \quad (2.12)$$

2.3.4 Cyclically Shifted Image

We establish the following definitions in order to facilitate discussions for the blur support identification.

DEFINITION 1: *Shift-Identity Matrix* is defined as

$$\mathcal{I}_M = \begin{bmatrix} 0 & 1 & \cdots & 0 \\ \vdots & \ddots & \ddots & \vdots \\ \vdots & \ddots & \ddots & 1 \\ 1 & \cdots & \cdots & 0 \end{bmatrix}_{M \times M} \quad (2.13)$$

where $\mathcal{I}_M \in \mathbb{R}^{M \times M}$. If we pre-multiply a column vector by a shift-identity matrix, the entries of the column vector will be shifted up circularly. We further define $\mathcal{I}_M^0 = \mathbf{I}_M$, where $\mathbf{I}_M \in \mathbb{R}^{M \times M}$ is the identity matrix.

DEFINITION 2: *Cyclically Shifted Image* is defined in terms of shift-identity matrix as:

$$\mathbf{f}_{(m,n)} = (\mathcal{I}_M^m \otimes \mathcal{I}_N^n) \mathbf{f} \quad (2.14)$$

where (m,n) is the shiftsize vector in the vertical and horizontal directions, respectively. The cyclically shifted image can be formed simply by circularly shifting the image matrix by shiftsize (m,n) .

2.4 Discrete Spatial Techniques

The degraded image can be modeled by combining the MA model in (1.3) with the AR model in (2.4) to give:

$$\mathbf{g} = \mathbf{H}(\mathbf{I} - \mathbf{A})^{-1} \mathbf{w} + \mathbf{n} \quad (2.15)$$

where \mathbf{n} and \mathbf{w} are assumed as additive white Gaussian noise (AWGN) with variance σ_n^2 and σ_w^2 .

Let \mathbf{r} be the filtered image obtained by convoluting the degraded image \mathbf{g} with a 2-D finite impulse response (FIR) filter \mathbf{I} . Under the condition that the filter \mathbf{I} satisfies $\mathbf{L} = \mathbf{I} - \mathbf{A}$, where \mathbf{L} and \mathbf{A} are the BCCB matrices constructed from the filter \mathbf{I} and AR model \mathbf{a} , the filtered image \mathbf{r} can be written as:

$$\mathbf{r} = \mathbf{L}\mathbf{g} = \mathbf{H}\mathbf{w} + (\mathbf{I} - \mathbf{A})\mathbf{n} \quad (2.16)$$

Equation (2.16) implies that the correlation function of \mathbf{r} is the sum of the correlations of \mathbf{H} and $\mathbf{I} - \mathbf{A}$ weighted by their respective noise variances, since \mathbf{w} and \mathbf{n} are uncorrelated and AWGN. Moreover, if σ_w^2 is much larger than σ_n^2 , the correlation of \mathbf{r} approaches that of \mathbf{H} .

In view of this, we propose the following methods to estimate the PSF support:

(1) Minimum cyclic-shift correlation (MCSC) estimator

$$\begin{aligned} \hat{P}_{MCSC} &= \arg \min_m \{R_{MCSC}(m, 0)\}; \quad \hat{Q}_{MCSC} = \arg \min_n \{R_{MCSC}(0, n)\} \\ \text{where } R_{MCSC}(m, n) &= \frac{1}{MN} \sum_{x=1}^M \sum_{y=1}^N [r(x, y)r(x+m, y+n)] \end{aligned} \quad (2.17)$$

where \hat{P} and \hat{Q} are the estimated blur support in the vertical and horizontal directions.

(2) Maximum average square difference (MASD) estimator:

$$\begin{aligned} \hat{P}_{MASD} &= \arg \max_m \{R_{MASD}(m, 0)\}; \quad \hat{Q}_{MASD} = \arg \max_n \{R_{MASD}(0, n)\} \\ \text{where } R_{MASD}(m, n) &= \frac{1}{MN} \sum_{x=1}^M \sum_{y=1}^N [r(x, y) - r(x+m, y+n)]^2 \end{aligned} \quad (2.18)$$

(3) Maximum average absolute difference (MAAD) estimator:

$$\begin{aligned} \hat{P}_{MAAD} &= \arg \max_m \{R_{MAAD}(m, 0)\}; \quad \hat{Q}_{MAAD} = \arg \max_n \{R_{MAAD}(0, n)\} \\ \text{where } R_{MAAD}(m, n) &= \frac{1}{MN} \sum_{x=1}^M \sum_{y=1}^N |r(x, y) - r(x+m, y+n)| \end{aligned} \quad (2.19)$$

Proof:

Let us first analyze the MCSC estimator in (2.17). The expected value of $R_{MCSC}(m, n)$ is:

$$E[R_{MCSC}(m, n)] = C_{rr}(m, n) = \frac{1}{MN} E[\mathbf{r}^H \mathbf{r}_{(m, n)}] \quad (2.20)$$

where $\mathbf{r}_{(m, n)} = (\mathcal{I}_M^m \otimes \mathcal{I}_N^n) \mathbf{r}$ is the cyclically shifted image as in (2.14), and $C_{rr}(m, n)$ is the autocorrelation of image \mathbf{r} given by:

$$\begin{aligned} C_{rr}(m, n) &= \frac{1}{MN} E[\mathbf{r}^H \mathbf{r}_{(m, n)}] \\ &= \frac{1}{MN} E[(\mathbf{H}\mathbf{w} + (\mathbf{I} - \mathbf{A})\mathbf{n})^H (\mathcal{I}_M^m \otimes \mathcal{I}_N^n) (\mathbf{H}\mathbf{w} + (\mathbf{I} - \mathbf{A})\mathbf{n})] \\ &= \frac{1}{MN} \sigma_w^2 \text{tr}[\mathbf{H}^H \mathbf{H} (\mathcal{I}_M^m \otimes \mathcal{I}_N^n)] + \frac{1}{MN} \sigma_n^2 \text{tr}[(\mathbf{I} - \mathbf{A})^H (\mathbf{I} - \mathbf{A}) (\mathcal{I}_M^m \otimes \mathcal{I}_N^n)] \end{aligned} \quad (2.21)$$

It is noted that (i) the inverse of a BCCB matrix is also a BCCB, and (ii) BCCB matrices are commutative. Previous studies have shown that in many practical applications, the MA noise power σ_n^2 is much smaller than the AR noise power σ_w^2 , implying that the MA /AR noise ratio $\sigma_n^2 / \sigma_w^2 \ll 1$ [3], [4], [6]-[8]. In line with these studies, we have assumed that the MA/AR noise ratio to be $\sigma_n^2 / \sigma_w^2 \ll 1$ in our work. Thus, the second term in (2.21) can be ignored when compared to the first term. We will further simplify (2.21) by substituting (2.12) to obtain:

$$\begin{aligned} C_{rr}(m, n) &= \frac{1}{MN} \sigma_w^2 \text{tr}[(\mathbf{H}_u \otimes \mathbf{H}_v)^H (\mathbf{H}_u \otimes \mathbf{H}_v) (\mathcal{I}_M^m \otimes \mathcal{I}_N^n)] \\ &= \sigma_w^2 MN \cdot C_{uu}(m) \cdot C_{vv}(n) \end{aligned} \quad (2.22)$$

where $C_{uu}(m)$ and $C_{vv}(n)$ are the autocorrelations of \mathbf{h}_u and \mathbf{h}_v , respectively:

$$\begin{aligned}
C_{uu}(m) &= E[u(x)^* u(x+m)] = \frac{1}{M} \mathbf{h}_u^H \mathcal{I}_M^m \mathbf{h}_u \\
C_{vv}(n) &= E[v(y)^* v(y+n)] = \frac{1}{N} \mathbf{h}_v^H \mathcal{I}_N^n \mathbf{h}_v
\end{aligned} \tag{2.23}$$

In the cases where the autocorrelation sequence \mathbf{h}_u is monotonically decreasing, which is applicable in many blurs such as Gaussian and concentric linear blurs, it is clear that the sequence $E[R_{MCSC}(m,0)]$ satisfies the following:

$$E[R_{MCSC}(0,0)] > E[R_{MCSC}(1,0)] > \dots > E[R_{MCSC}(P,0)] = E[R_{MCSC}(P+1,0)] = \dots \tag{2.24}$$

Therefore, we observe that $E[R_{MCSC}(0,0)]$ will reach the minimum value when $m \geq P$, where P is the support of the PSF in the vertical direction. Similar argument can be used to verify \hat{Q}_{MCSC} in (2.17).

As far as the MASD in (2.18) is concerned, the expected value of $R_{MASD}(m,n)$ is:

$$\begin{aligned}
E[R_{MASD}(m,n)] &= \frac{1}{MN} E[(\mathbf{r}^H \mathbf{r} + \mathbf{r}_{(m,n)}^H \mathbf{r}_{(m,n)} - 2\mathbf{r}^H \mathbf{r}_{(m,n)})] \\
&= 2(C_{rr}(0,0) - C_{rr}(m,n))
\end{aligned} \tag{2.25}$$

This suggests that the minimum of $R_{MASD}(m,n)$ can be used to estimate \hat{P}_{MASD} and \hat{Q}_{MASD} .

We can derive the following expression for MAAD by using the invariance theorem [20]:

$$E[R_{MAAD}(m,n)] = 2\sqrt{(C_{rr}(0,0) - C_{rr}(m,n)) / \pi} \tag{2.26}$$

The MAAD estimator has low computational cost as it does not require multiplications. Therefore, it is useful for those applications where low computational complexity is a major consideration. It is worth mentioning that MCSC identifies the blur support by locating the minima, while the MASD and MAAD by using the maxima.

2.5 AR Image Model Estimation

It has been shown that our techniques will achieve its optimal solution when $\mathbf{L} = \mathbf{I} - \mathbf{A}$ in (2.16). The estimation of the AR model will influence the performance of the proposed techniques. Different AR models including causal, semicausal, and noncausal structures have been employed in modeling the images [15]. Various techniques have also been proposed to estimate the half plane causal AR model, such as the recursive method [12] and maximum likelihood method [6]. We will formulate an AR model estimation method that is applicable for noncausal as well as causal and semicausal structures. The AR model in (2.4) can be re-expressed alternatively as:

$$\mathbf{f} = \mathcal{F}\mathbf{a} + \mathbf{w} \quad (2.27)$$

where \mathbf{a} is the column vector formed by concatenating the coefficients of the AR model:

$$\mathbf{a} = \left[a_{(-\alpha, -\beta)} \quad \cdots \quad a_{(-1, 0)} \quad a_{(1, 0)} \quad \cdots \quad a_{(\alpha, \beta)} \right]^T \quad (2.28)$$

with the AR model having a support size of $(2\alpha + 1) \times (2\beta + 1)$ and $a_{(0, 0)} = 0$.

\mathcal{F} is the stacked array of $\mathbf{f}_{(i, j)}$, where $\mathbf{f}_{(i, j)}$ is the cyclically shifted image as in (2.14)

$$\mathcal{F} = \left[\mathbf{f}_{(-\alpha, -\beta)} \quad \cdots \quad \mathbf{f}_{(-1, 0)} \quad \mathbf{f}_{(1, 0)} \quad \cdots \quad \mathbf{f}_{(\alpha, \beta)} \right] \quad (2.29)$$

The minimum variance unbiased (MVU) estimator for the AR model is given by:

$$\hat{\mathbf{a}} = (\mathcal{F}^T \mathcal{F})^{-1} \mathcal{F}^T \mathbf{f} \quad (2.30)$$

It can be shown that this estimator is unbiased, and attains the Cramer-Rao lower bound (CRLB), provided $\mathcal{F}^T \mathcal{F}$ is invertible and \mathbf{w} is AWGN. In ideal condition where the original image \mathbf{f} is available, we can estimate $\hat{\mathbf{a}}$ readily using (2.30). However, only the knowledge of the degraded image \mathbf{g} is available in blind image deconvolution. Therefore, we

need to reformulate the MVU estimator in terms of the degraded image. Rewriting \mathbf{g} in another format, we obtain:

$$\begin{aligned}\mathbf{g} &= \mathbf{H}(\mathbf{A}\mathbf{f} + \mathbf{w}) + \mathbf{n} \\ &= \mathbf{A}\mathbf{g} + \mathbf{H}\mathbf{w} + (\mathbf{I} - \mathbf{A})\mathbf{n} \\ &= \mathcal{G}\mathbf{a} + \mathbf{n}_1\end{aligned}\tag{2.31}$$

where \mathcal{G} has the same structure as \mathcal{F} in (2.30), and $\mathbf{n}_1 = \mathbf{H}\mathbf{w} + (\mathbf{I} - \mathbf{A})\mathbf{n}$, with \mathbf{n}_1 being the colored Gaussian noise with $\mathbf{n}_1 \sim N(\mathbf{0}, \mathbf{\zeta})$, where $\mathbf{\zeta} = \sigma_w^2 \mathbf{H}\mathbf{H}^T + \sigma_n^2 (\mathbf{I} - \mathbf{A})(\mathbf{I} - \mathbf{A})^T$.

From Gauss-Markov Theorem [21], the MVU estimator is given by

$$\hat{\mathbf{a}} = (\mathcal{G}^T \mathbf{\zeta}^{-1} \mathcal{G})^{-1} \mathcal{G}^T \mathbf{\zeta}^{-1} \mathbf{g}\tag{2.32}$$

Since the estimator in (2.32) requires excessive computational cost due to the high dimensionality of $\mathbf{\zeta}$ (namely $MN \times MN$), we simplify the complexity by assuming that the degraded image is noiseless to obtain the following estimator:

$$\hat{\mathbf{a}} = (\mathcal{G}^T \mathcal{G})^{-1} \mathcal{G}^T \mathbf{g}\tag{2.33}$$

The performance evaluation of the estimator in (2.33) is discussed in the Appendix.

An important condition of AR model estimation lies in the relative homogeneity of the whole image. This is, however, restrictive, as some real-life images are non-homogeneous, consisting of numerous smooth and textured image regions. In order to overcome this limitation, we can decompose an image into a number of homogeneous or quasi-homogeneous image blocks by quadtree decomposition. The formation of the image blocks is determined based on standard homogeneity criterion such as local image variance. Hence, the proposed discrete spatial techniques can be implemented independently for each block. This procedure can reduce the constraint of Gaussian stationarity condition.

2.6 Experimental Results

2.6.1 Blur Support Identification of 2-D PSF.

The 256×256 “Flower” image shown in Figure 2.2(a) is degraded by 7×7 Gaussian blur with standard deviation $\sigma = 3.2$ in Figure 2.2(b) to produce Figure 2.2(c). The AR model \mathbf{a} is computed using (2.33), and the filter $\mathbf{L} = \mathbf{I} - \mathbf{A}$ is applied to the degraded image to obtain the filtered image. The MCSC, MASD, and MAAD of the filtered image in the vertical and horizontal directions are given in Figure 2.2(d) and (e). It is noted that the values of MCSC, MASD, and MAAD are normalized in order to accommodate them in a single figure. We observe from Figure 2.2 (d) that all estimators achieve the minima or maxima at $m=7$, which is the actual blur support in the vertical direction. Similarly, the techniques reach the minima or maxima at $n=7$ in the horizontal direction as shown in Figure 2.2(e). Therefore, the methods have correctly identified the support of the PSF as 7×7 .

Moreover, the methods are still effective as the SNR reaches 25dB in this case. It is worth mentioning that when we apply median filter to remove noise in the degraded image, the proposed methods can work even better in low SNR environment. This illustrates that the proposed methods are robust in identifying blur support under different SNR environments.

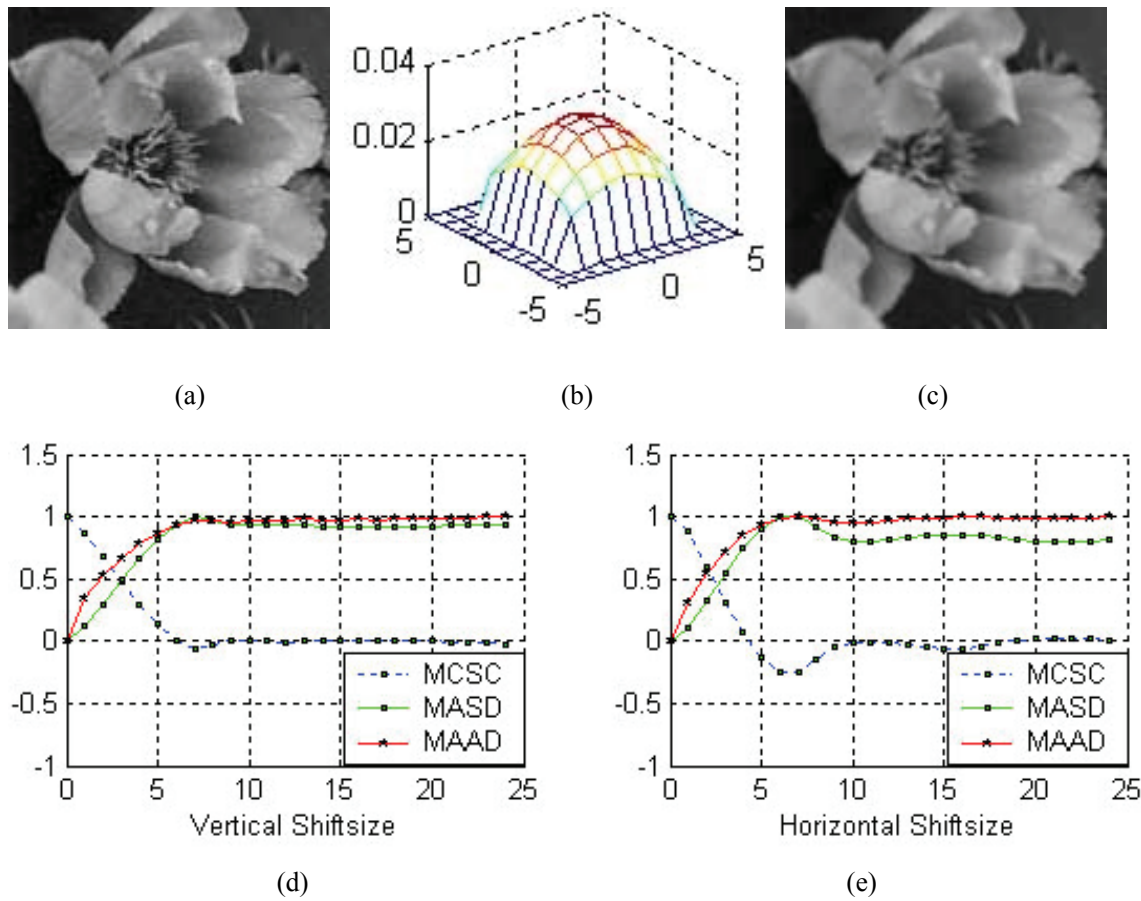


Figure 2.2 Blur support identification of 2-D PSF. (a) Original “Flower” image, (b) 2-D Gaussian PSF (size 7×7 , $\sigma = 3.2$), (c) Image degraded by Gaussian PSF, (d) MCSC, MASD and MAAD profiles in the vertical direction, (e) MCSC, MASD and MAAD profiles in the horizontal direction.

2.6.2 Image Restoration Using Various PSF Support Sizes

Blur identification from noisy blurred image is a challenging problem in blind image deconvolution. We illustrate the capability of the proposed algorithm to handle noisy degraded image. The 512×512 “Lena” image in Figure 2.3(a) is selected as the test image. The image is degraded by 5×7 uniform PSF in Figure 2.3(b), followed by 30dB SNR AWGN. We repeat the procedure as in previous experiments. The results are shown in Figure 2.3(d) and Figure 2.3(e). It is observed that the all methods manage to identify the blur support as 5×7 correctly under 30dB noise. In order to illustrate the significance of blur support identification, we restore the image and identify the PSF under different PSF support sizes. The proposed parametric double regularization (PDR) algorithm in Chapter 4 is run with iteration numbers of alternating minimization (AM) and conjugate gradient optimization (CGO) being set to 10. The comparison of the restored images and identified PSFs with different blur support sizes are tabulated in Table 2.1.

The peak signal-to-noise ratio (PSNR) is employed for evaluation of image quality,

$$PSNR = 10 \log_{10} \left(\frac{255^2 \cdot MN}{\sum_{(x,y)} (f(x,y) - \hat{f}(x,y))^2} \right) \quad (2.34)$$

where $f(x,y)$ and $\hat{f}(x,y)$ are the original and the estimated images.

The sum of square error (SSE) is used for PSF evaluation:

$$SSE = \sum_{(x,y) \in \text{sup}(S_{h_1}, S_{h_2})} (h(x,y) - \hat{h}(x,y))^2 \quad (2.35)$$

where $h(x,y)$ and $\hat{h}(x,y)$ denote the coefficients of the original and the identified PSFs, respectively. As the original and the identified PSFs may have different support size, we pad

the smaller-size PSF with zeros.

From Table 2.1, it is clear that the restored image with good support dimension such as 5×7 outperforms the others as it has the highest PSNR and lowest SSE. The results clearly show good PSF support size can produce superior image quality during blind image restoration.

TABLE 2.1 COMPARISON OF RESTORED IMAGES WITH DIFFERENT SUPPORT SIZES

Blur Support Size	3×3	5×5	5×7	7×7	7×9	9×9	11×11
PSNR of restored images	28.05	29.28	30.88	29.68	29.30	29.04	28.90
SSE of identified PSFs	0.082	0.0114	0.0015	0.0059	0.0082	0.0083	0.0091

2.6.3 Blur Support Identification under Noisy Condition

In some experiments, there may have multiple maximum (or minimum) points that become the candidates for the support size. A 512×512 “Woman” image shown in Figure 2.4(a) is blurred by a 9×9 uniform PSF in Figure 2.4(b) under 40dB noise level. The proposed approaches are applied to the degraded image in Figure 2.4(c). In Figure 2.4(d) and (e), it is observed that multiple maximum values (MAAD and MASD) are achieved when the vertical and horizontal shiftsize are larger than 9. Together with MCSC, we will select the extremum with the smallest vertical or horizontal shiftsize if multiple candidates exist, which is 9×9 in Figure 2.4. In practice, the approach in [22] is recommended which can use the corner of the L-curve to estimate the support size (or lower- and upper-bounds of the support size). In addition, to facilitate the implementation of image restoration where blur support is usually taken as odd number, we will choose the next-best (odd number) blur support estimate. For example, if the estimated blur supports is 4×5 , the restoration scheme will adopt 3×5 or 5×5 as the estimated support.

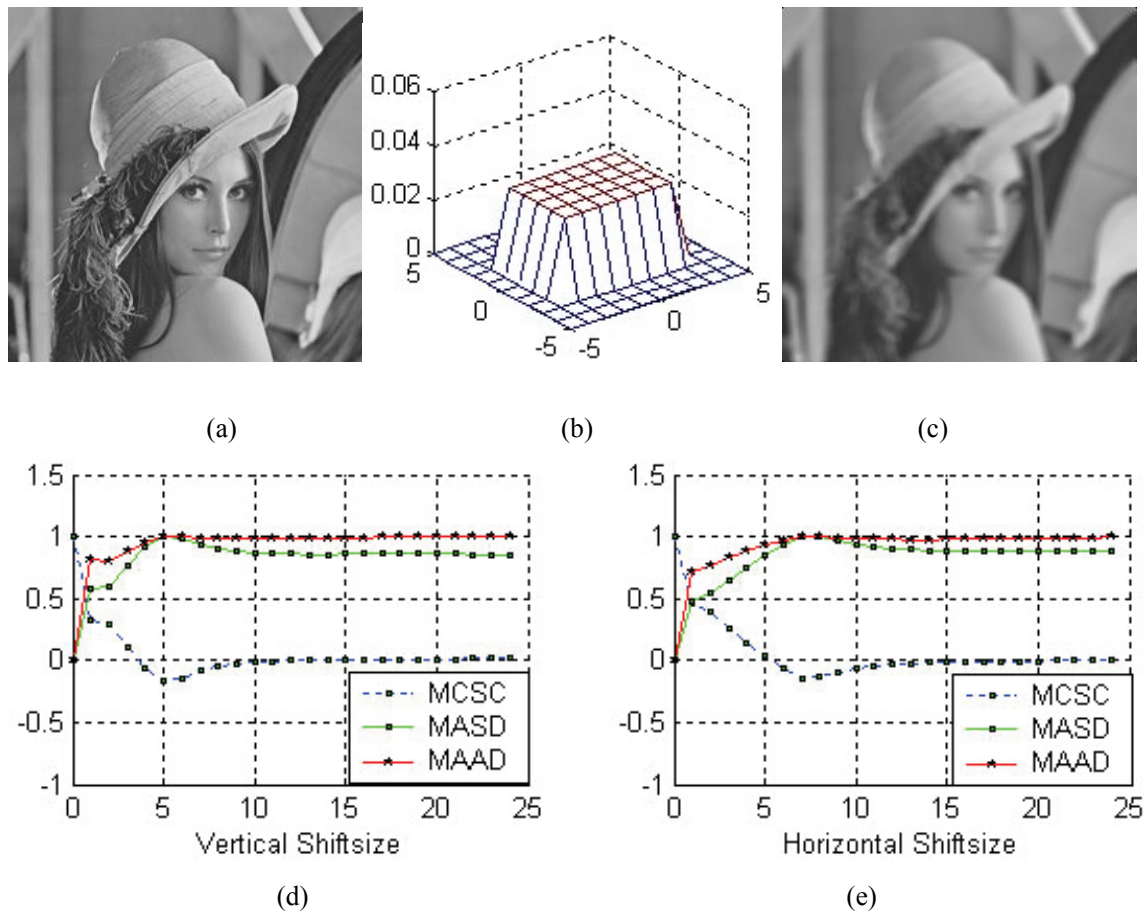


Figure 2.3 Blur support identification under 30dB noise level. (a) Original “Lena” image, (b) 2-D uniform PSF (size 5×7), (c) Image degraded by uniform PSF, (d) MCSC, MASD and MAAD profiles in the vertical direction, (e) MCSC, MASD and MAAD profiles in the horizontal direction.

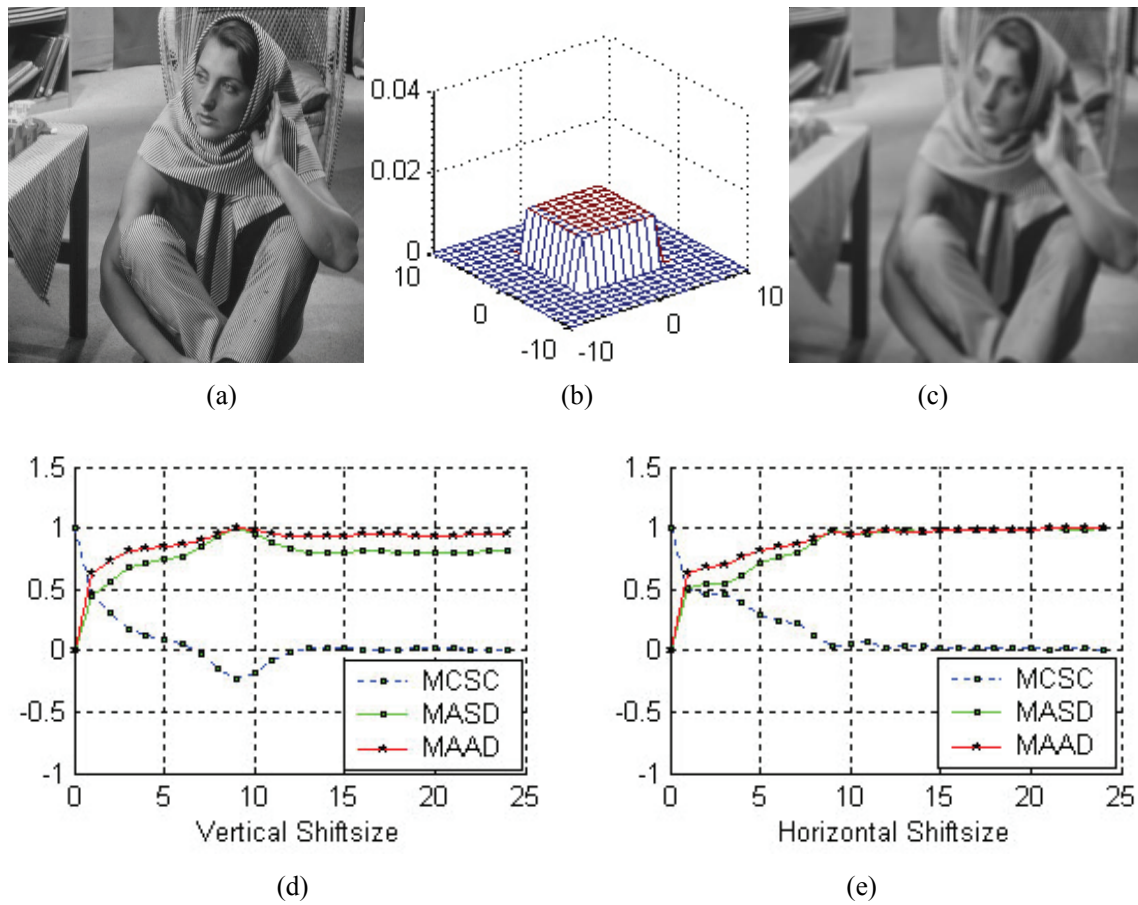


Figure 2.4 Blur support identification of 2-D PSF. (a) Original "Woman" image, (b) 2-D uniform PSF (size 9×9), (c) Image degraded by uniform PSF, (d) MCSC, MASD and MAAD profiles in the vertical direction, (e) MCSC, MASD and MAAD profiles in the horizontal direction.

2.6.4 Comparison with Other Blur Support Identification Methods

The 512×512 “Lena” image in Figure 2.3(a) is blurred by different PSFs in Figure 2.5(a)-(c), and followed by 30dB or 40dB additive noise, respectively. The identified support using the proposed methods are compared with two other well-known methods, namely, cepstrum [3] and ITP [14], and the results are given in Table 2.2. It is clear from Table 2.2 that the proposed methods manage to identify the blur support successfully in all the cases. In contrast, the cepstrum method fails to detect negative cepstral spikes in the vertical direction in some cases, particularly in more noisy environments of 30dB noise. We mark these occasions with “-” in Table 2.2. On the other hand, it can be seen that ITP makes some erroneous identification. This is because ITP is sensitive to various factors such as initial blur estimate, regularization scheme, and pruning threshold selection. The results show that the proposed methods are robust towards different blur types and up to at least 30dB noise levels.

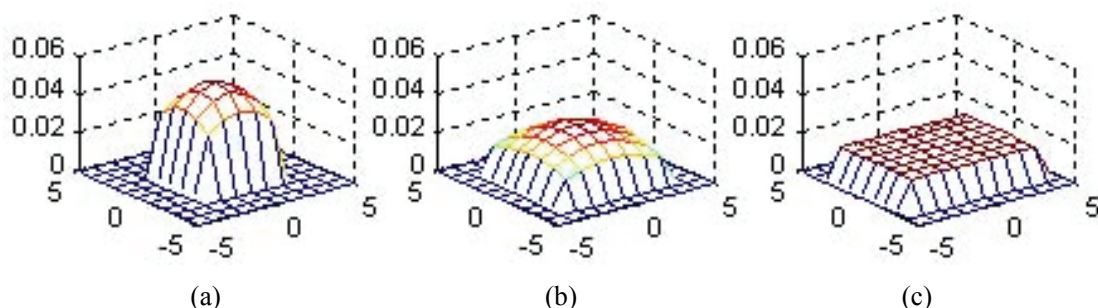


Figure 2.5 Different PSFs. (a) 2-D Gaussian PSF (size 5×5 , $\sigma = 3.0$), (b) 2-D Gaussian PSF (size 7×7 , $\sigma = 3.5$), (c) 2-D uniform PSF (size 7×9).

TABLE 2.2 BLUR SUPPORT IDENTIFICATION BY DIFFERENT METHODS

PSF	Gaussian 5×5, σ=3.0		Gaussian 7×7, σ=3.5		Uniform 7×9	
Noise Level	40dB	30dB	40dB	30dB	40dB	30dB
Cepstrum	5×5	-×5	7×7	-×7	9×9	-×11
ITP	5×5	7×7	9×9	9×9	11×9	11×11
Proposed	5×5	5×5	7×7	7×7	7×9	7×9

2.6.5 Blur Support Identification for Infinite- or Large-Support PSF

In some practical situations, the PSF will have infinite- or large-support size but the energy of the PSF will be concentrated near the center of the PSF. To simulate this scenario, a sample PSF is modeled by the following Gaussian mixture:

$$h(x, y) = h_1(x, y) + h_2(x, y) \quad (2.36)$$

where

$$h_1 = \begin{cases} a_1 \exp(-(x^2 + y^2) / 2\sigma_1^2) & (x, y) \in S_{h_1} \\ 0, & \text{otherwise} \end{cases} \quad (2.37)$$

$$h_2 = \begin{cases} a_2 \exp(-(x^2 + y^2) / 2\sigma_2^2) & (x, y) \in S_{h_2} \\ 0, & \text{otherwise} \end{cases}$$

Here $h(x, y)$ is composed of two different Gaussian blurs with $S_{h_1} < S_{h_2}$ and $\sigma_1 < \sigma_2$. Since $h_1(x, y)$ is narrower and steeper than $h_2(x, y)$, the effective 2-D profile of $h(x, y)$ is bounded by $S_{h_1} \leq S_h \leq S_{h_2}$. Figure 2.6(b) shows an example of such PSF with $S_{h_1} = 5 \times 5$, $\sigma_1 = 2$, $S_{h_2} = 13 \times 13$, $\sigma_2 = 4$. The coefficients of the PSF are given by

$$\begin{bmatrix} 0.0007 & 0.0009 & 0.0012 & 0.0015 & 0.0018 & 0.0019 & 0.0020 & 0.0019 & 0.0018 & 0.0015 & 0.0012 & 0.0009 & 0.0007 \\ 0.0009 & 0.0013 & 0.0017 & 0.0021 & 0.0025 & 0.0027 & 0.0028 & 0.0027 & 0.0025 & 0.0021 & 0.0017 & 0.0013 & 0.0009 \\ 0.0012 & 0.0017 & 0.0023 & 0.0028 & 0.0033 & 0.0036 & 0.0038 & 0.0036 & 0.0033 & 0.0028 & 0.0023 & 0.0017 & 0.0012 \\ 0.0015 & 0.0021 & 0.0028 & 0.0060 & 0.0087 & 0.0112 & 0.0122 & 0.0112 & 0.0087 & 0.0060 & 0.0028 & 0.0021 & 0.0015 \\ 0.0018 & 0.0025 & 0.0033 & 0.0087 & 0.0134 & 0.0178 & 0.0196 & 0.0178 & 0.0134 & 0.0087 & 0.0033 & 0.0025 & 0.0018 \\ 0.0019 & 0.0027 & 0.0036 & 0.0112 & 0.0178 & 0.0240 & 0.0266 & 0.0240 & 0.0178 & 0.0112 & 0.0036 & 0.0027 & 0.0019 \\ 0.0020 & 0.0028 & 0.0038 & 0.0122 & 0.0196 & 0.0266 & 0.0295 & 0.0266 & 0.0196 & 0.0122 & 0.0038 & 0.0028 & 0.0020 \\ 0.0019 & 0.0027 & 0.0036 & 0.0112 & 0.0178 & 0.0240 & 0.0266 & 0.0240 & 0.0178 & 0.0112 & 0.0036 & 0.0027 & 0.0019 \\ 0.0018 & 0.0025 & 0.0033 & 0.0087 & 0.0134 & 0.0178 & 0.0196 & 0.0178 & 0.0134 & 0.0087 & 0.0033 & 0.0025 & 0.0018 \\ 0.0015 & 0.0021 & 0.0028 & 0.0060 & 0.0087 & 0.0112 & 0.0122 & 0.0112 & 0.0087 & 0.0060 & 0.0028 & 0.0021 & 0.0015 \\ 0.0012 & 0.0017 & 0.0023 & 0.0028 & 0.0033 & 0.0036 & 0.0038 & 0.0036 & 0.0033 & 0.0028 & 0.0023 & 0.0017 & 0.0012 \\ 0.0009 & 0.0013 & 0.0017 & 0.0021 & 0.0025 & 0.0027 & 0.0028 & 0.0027 & 0.0025 & 0.0021 & 0.0017 & 0.0013 & 0.0009 \\ 0.0007 & 0.0009 & 0.0012 & 0.0015 & 0.0018 & 0.0019 & 0.0020 & 0.0019 & 0.0018 & 0.0015 & 0.0012 & 0.0009 & 0.0007 \end{bmatrix}$$

It can be observed that the energy of the PSF is centered within the central 7×7 support area, even though the actual blur support is the larger value of 13×13 .

The original 512×512 “Lena” image in Figure 2.6 (a) is degraded by the PSF in Figure 2.6 (b) to produce the degraded image in Figure 2.6 (c). The proposed methods are applied to obtain the estimated blur support size in Figure 2.6 (d) and (e). From the figures, it can be observed that the estimated blur supports is 7×8 . To facilitate the implementation of image restoration where blur support is usually taken as odd number, we will choose the next-best blur support estimate to be 7×7 or 7×9 . The proposed PDR algorithm in Chapter 4 is run with iteration number of alternating minimization (AM) and conjugate gradient optimization (CGO) being 10. The restored images with different blur support size are given in Figure 2.6 (f)-(m) and the corresponding PSNR are tabulated Table 2.3. It is clear that the restored image with good support dimension such as 7×7 in Figure 2.6 (h) outperforms the others as it has the highest PSNR. If the estimated size is smaller than the actual support, insufficient textured or edge details are restored as shown in Figure 2.6 (f). Conversely, if support is larger than the actual support, extreme ringing and noise amplification dominates the scene as in Figure 2.6 (l) and (m). A good compromise of the support size between 7×7 and 11×11 will provide a higher quality in the restored image, as shown in Figure 2.6 (g)-(k).

TABLE 2.3 IMAGE DECONVOLUTION FOR LARGE-SUPPORT PSF

Blur Support Size	5×5	5×7	7×7	7×9	9×9	11×11	13×13	15×15
PSNR(dB)	28.87	29.57	30.33	29.93	29.37	29.24	28.82	19.13

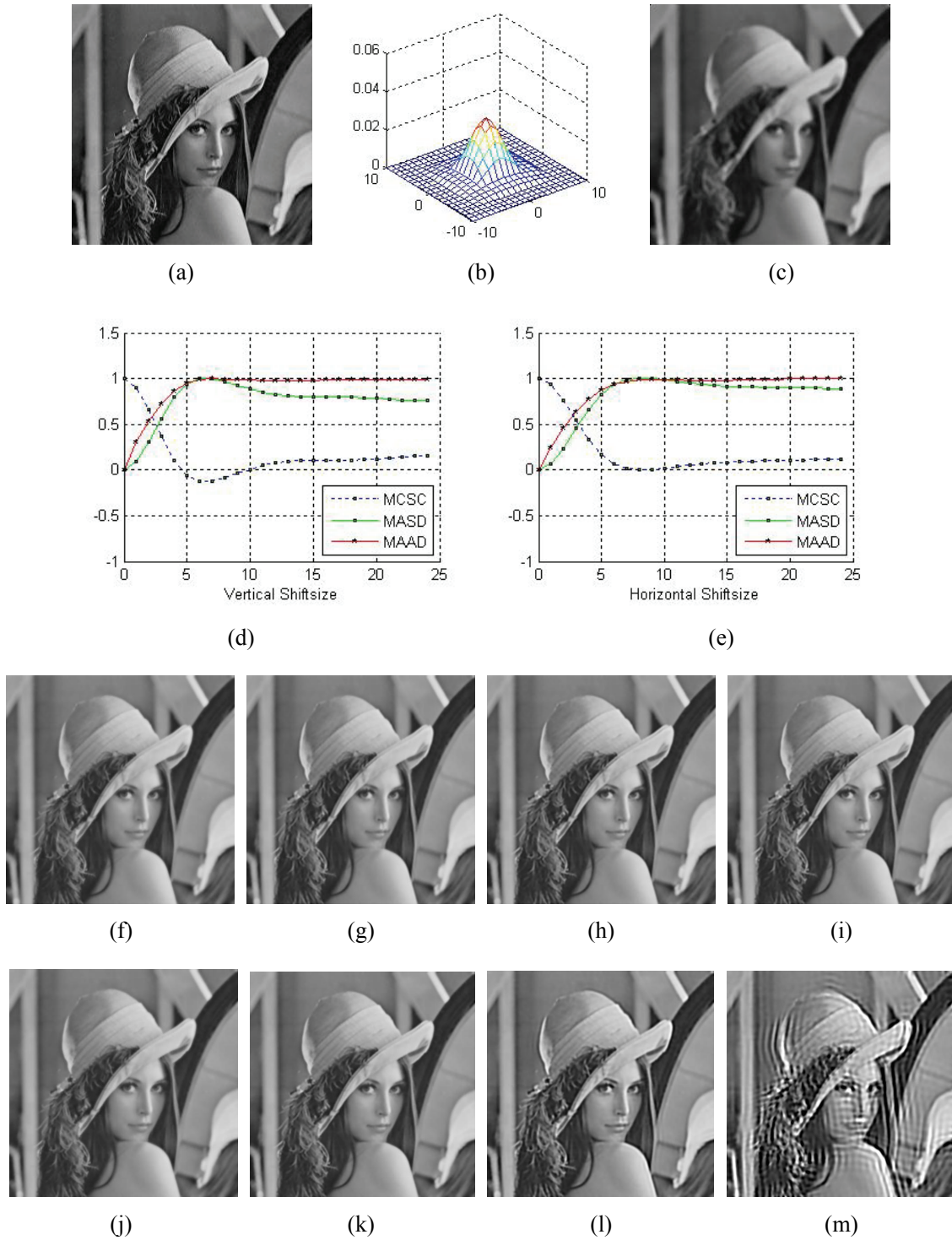


Figure 2.6 Blind deconvolution of image degraded by a PSF with large blur support size. (a) Original “Lena” image, (b) Gaussian mixture PSF, (c) Image degraded by PSF, (d) MCSC, MASD and MAAD profiles in the vertical direction, (e) MCSC, MASD and MAAD profiles in the horizontal direction, (f) 5×5, (g) 5×7, (h) 7×7, (i) 7×9, (j) 9×9, (k) 11×11, (l) 13×13, (m) 15×15.

2.7 Summary

Three efficient discrete spatial techniques, namely MCSC, MASD and MAAD have been developed for blur support identification. The methods can provide robust estimate of the support for 1-D blurs as well as 2-D blurs. The efficiency and validity of the techniques have also been analyzed.

2.8 Appendix

We will analyze the efficiency of the proposed estimator in (2.33). An estimator is efficient if it satisfies two conditions: (i) it is unbiased, and (ii) its variance achieves CRLB. From (2.31), we have:

$$\mathbf{g} = \mathcal{G}\mathbf{a} + \mathbf{n}_1, \mathbf{g} \sim N(\boldsymbol{\mu}(\mathbf{a}), \boldsymbol{\zeta}), \mathbf{n}_1 \sim N(\mathbf{0}, \boldsymbol{\zeta}) \quad (2.38)$$

where $\boldsymbol{\mu}(\mathbf{a}) = \mathcal{G}\mathbf{a}$, $\boldsymbol{\zeta} = \sigma_w^2 \mathbf{H}\mathbf{H}^T + \sigma_n^2 (\mathbf{I} - \mathbf{A})(\mathbf{I} - \mathbf{A})^T$

(1) Expectation of $\hat{\mathbf{a}}$

$$E(\hat{\mathbf{a}}) = E[(\mathcal{G}^T \mathcal{G})^{-1} \mathcal{G}^T (\mathcal{G}\mathbf{a} + \mathbf{n}_1)] = \mathbf{a} + E[(\mathcal{G}^T \mathcal{G})^{-1} \mathcal{G}^T \mathbf{n}_1] = \mathbf{a} \quad (2.39)$$

(2) Variance of $\hat{\mathbf{a}}$

$$\text{var}(\hat{\mathbf{a}}) = E[(\mathcal{G}^T \mathcal{G})^{-1} \mathcal{G}^T (\mathbf{g} - \mathbf{a})][(\mathcal{G}^T \mathcal{G})^{-1} \mathcal{G}^T (\mathbf{g} - \mathbf{a})^T] = (\mathcal{G}^T \mathcal{G})^{-1} \mathcal{G}^T \boldsymbol{\zeta} \mathcal{G} (\mathcal{G}^T \mathcal{G})^{-1} \quad (2.40)$$

The Fisher's information matrix is given by [21]:

$$[\mathbf{J}(\mathbf{a})]_{ij} = \left[\frac{\partial \boldsymbol{\mu}(\mathbf{a})}{\partial \mathbf{a}_i} \right]^T \boldsymbol{\zeta}^{-1} \left[\frac{\partial \boldsymbol{\mu}(\mathbf{a})}{\partial \mathbf{a}_j} \right] + \frac{1}{2} \text{tr} \left[\boldsymbol{\zeta}^{-1} \frac{\partial \boldsymbol{\zeta}}{\partial \mathbf{a}_i} \boldsymbol{\zeta}^{-1} \frac{\partial \boldsymbol{\zeta}}{\partial \mathbf{a}_j} \right] \quad (2.41)$$

Thus the CRLB is the $[i, i]$ elements of the inverse matrix that $\text{var}(\hat{\mathbf{a}}_i) \geq [\mathbf{J}^{-1}(\mathbf{a})]_{ii}$. It is

difficult to compute the CRLB analytically using (2.41) as it involves the inversion of a large covariance matrix \mathbf{C} . To simplify the analysis, we consider the noiseless degraded image, where $\sigma_n^2 = 0$. Thus we obtain:

$$\begin{aligned} \text{var}(\hat{\mathbf{a}}) &= \sigma_w^2 (\mathbf{G}^T \mathbf{G})^{-1} \mathbf{G}^T \mathbf{H} \mathbf{H}^T \mathbf{G} (\mathbf{G}^T \mathbf{G})^{-1} \\ \mathbf{J}(\mathbf{a}) &= \frac{1}{\sigma_w^2} \mathbf{G}^T (\mathbf{H} \mathbf{H}^T)^{-1} \mathbf{G} \end{aligned} \quad (2.42)$$

It can be observed that $\text{var}(\hat{a}_i) \approx [\mathbf{J}^{-1}(\mathbf{a})]_{ii}$ when the blur has a small support.

Chapter 3

Parametric Double Regularization

Approach for Deconvolution

3.1 Introduction

Image deconvolution is an inverse process that attempts to deconvolute the blurred and noisy images to recover the original scene. Figure 3.1 shows the system flowchart of the deconvolution process, where the blurred image is passed through an inverse filter to produce the restored image. Classical image restoration assumes that the PSF is known prior to deconvolution. This is, however, elusive in real-world applications due to various practical constraints that PSF cannot be calibrated in advance. This leads to the study of blind image deconvolution (blind image restoration) where the primary objective is to perform joint blur identification and image restoration given little or no prior knowledge about the blur [3], [4].

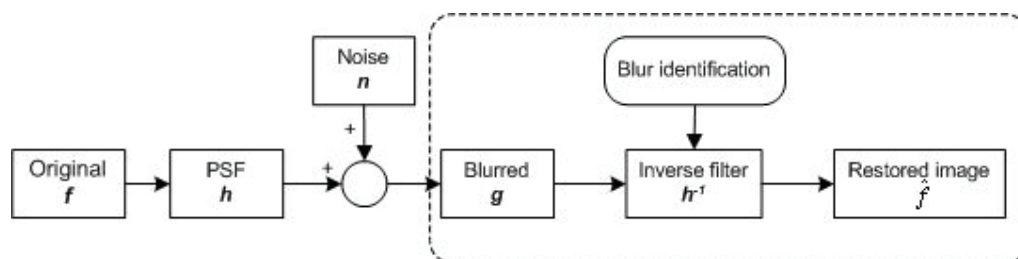


Figure 3.1 Image blurring model and deconvolution process.

Even when the PSF is known prior to deconvolution, it is impossible to deconvolute the blurred image directly to give a close-fidelity of the estimated image by $\tilde{\mathbf{f}}(\omega) = (\tilde{\mathbf{g}}(\omega) - \tilde{\mathbf{n}}(\omega)) / \tilde{\mathbf{H}}(\omega)$. The reason is that the condition number of \mathbf{H} is large. A trivial perturbation in \mathbf{g} can produce non-trivial perturbations in $\hat{\mathbf{f}}$. The restored image will be subjected to noise amplification when there exists noise in \mathbf{g} . In the worst scenario, the smallest eigenvalue of \mathbf{H} will equal or approximate zero. The solution $\hat{\mathbf{f}}$ may not exist as $\tilde{\mathbf{H}}(\omega)^{-1} \rightarrow \infty$. To reduce the condition number of \mathbf{H} , the common approach is using regularization to impose constraint on the image. This leads to the conventional Wiener filter and constraint least squares. Moreover, since PSF is unknown in blind deconvolution, more than one solution may exist when $\hat{\mathbf{H}}_{(1)}\hat{\mathbf{f}}_{(1)} = \hat{\mathbf{H}}_{(2)}\hat{\mathbf{f}}_{(2)}$, where $\hat{\mathbf{H}}_{(1)}, \hat{\mathbf{H}}_{(2)}, \hat{\mathbf{f}}_{(1)}, \hat{\mathbf{f}}_{(2)}$ are the estimated blurs and images. Therefore, blind image deconvolution is a difficult ill-posed inverse problem as the uniqueness and stability of the solutions is not guaranteed.

The rest of this chapter is organized as follows. Section 3.2 reviews the methods for blind image deconvolution. Section 3.3 provides a discussion on cost function formulation. In Section 3.4, the development of parametric modeling is explained. In Section 3.5, the derivation of optimization procedure is discussed. In Section 3.6, experimental results using the proposed method are discussed and compared with other techniques. In Section 3.7, conclusions and further remarks are given.

3.2 Literature Review

Various techniques have been proposed to address blind image deconvolution over the last two decades. A popular parametric approach in representing linear image degradation processes is centered on autoregressive moving-average (ARMA) model. The AR and MA

processes are used to model the original image and PSF, respectively. Under this framework, the objective of blind deconvolution is to estimate these parameters using statistical methods such as maximum likelihood (ML) [6], expectation maximization (EM) [7], [23] and generalized cross-validation (GCV) [8]. EM is used in conjunction with the ML method to maximize the log-likelihood function of the ARMA parameter set in the solution space. In contrast, GCV determines the parameters by minimizing a weighted sum of predictive errors. The shortcomings of ARMA modeling include its sensitivity towards high-dimensional parametric vector, leading to poor local convergence.

The development of filtering theory with constraints has been extended to address blind image deconvolution by some researchers. Iterative blind deconvolution (IBD) adopts Wiener-based filter to restore the image and identify the blur alternately [24]. The major drawback of IBD lies in its sensitivity towards initial image estimate and noise, thus leading to algorithmic instability. Another class of iterative methods include NAS-RIF [25], together with its extensions such as enhanced NAS-RIF [26], and regularized RIF [27]. NAS-RIF methods involve recursive filtering of the blurred image to minimize a predictive cost function, which is based on the difference between the estimated true image and the projected image. They require the image object to have a known support and be located in a uniform background. This is inflexible as the assumption conflicts with many real-life images.

Another research direction involves extending the regularization theory to address image deconvolution. The regularized adaptive iterative algorithms for image deconvolution have been proposed in [28], [29]. Projection-based approaches with conjugate-gradient minimization have also been developed in [30], [31]. Symmetric double regularization (SDR) combines the advantages of the above two methodologies, i.e. formulates the blind problem as the minimization of an adaptive double *Tikhonov* regularization cost function, decomposes it

into two symmetric processes of blur identification and image deconvolution, where each process is minimized by conjugate gradient optimization (CGO) [14]. Anisotropic regularization attempts to mitigate the lack of information by exploiting the piecewise smoothness of the images and blur [32]. One of the successful regularization approaches is the total variation (TV) regularization method [33], [34]. TV regularization has also been incorporated into SDR to achieve edge preservation and noise suppression [35].

Motivated by parallel computational power and intelligence of the neural networks (NN), a number of researchers have attempted to achieve good restoration results via the dense interconnection of neurons. The NN model is employed to represent the possibly nonstationary image [36]. The restoration procedure consists of two stages: estimation of the parameters of the NN model and reconstruction of images. During the first stage, the parameters are estimated by comparing the energy function of the network to a constrained error function. The nonlinear restoration method is then carried out iteratively in the second stage by using a dynamic algorithm to minimize the energy function of the network. Further, the modified Hopfield NN is proposed for regularized image restoration [37]. A hierarchical cluster model (HCM) is developed that consists of parallel, distributed subnetworks [38], [39]. HCM models the organization of the neo-cortex in human brain where functional groups of neurons organize themselves dynamically into multidimensional subnetworks. This idea is extended to formulate a recursive blind deconvolution scheme based on soft blur identification and hierarchical network model [40], [41].

It is well known that most PSFs satisfy up to a certain degree of parametric structure [1]-[4]. Conventional blind methods require a hard-decision on the structure of PSF to be made prior to deconvolution. This either restricts the flexibility of the algorithms, as exemplified by *a priori* blur identification, or results in underutilization of the information available, as

illustrated in SDR and NAS-RIF approaches. In view of this, this chapter proposes a parametric double regularization (PDR) approach for adaptive blind image deconvolution. A novel manifold soft parametric modeling (MSPM) algorithm is developed to evaluate the relevance of multiple parametric blur structures, and integrate the useful information into the scheme. An optimization procedure called alternating minimization (AM) is then employed to minimize the image- and blur-domain cost functions iteratively.

3.3 Development of Cost Function

The main issues involved in the design of blind image deconvolution comprise: (i) proposal of meaningful cost function, (ii) integration of useful *a priori* information, and (iii) development of effective optimization procedure. We will examine the development of the meaningful cost function in this section.

Blind image deconvolution is an ill-posed problem, as the stability of the solution is not guaranteed. The regularization approach is effective in offering numerically stable and visually pleasing solution. SDR adopts two regularization functionals to impose the constraints on the estimated original image and PSF, respectively. The regularization functional can be either TV to minimize the energy of first-order derivative or *Tikhonov* for second-order derivative. To perform effective joint blur identification and image deconvolution, we extend DR by proposing the following cost function:

$$J(\mathbf{f}, \mathbf{h}) = \|\mathbf{g} - \mathbf{H}\mathbf{f}\|^2 + R(\mathbf{f}) + R(\mathbf{h}) + S(\mathbf{h}) \quad (3.1)$$

where $\|\cdot\|$ represents the L_2 -norm. For ease of notation, we omit cap “ \wedge ” that represents the estimated results for blur and image.

The first term in (3.1) represents the least-square data fidelity of the estimated \mathbf{f} and \mathbf{h} with

respect to the degrade image \mathbf{g} . $R(\mathbf{f})$ and $R(\mathbf{h})$ are the *Tikhonov* regularization functionals that introduce stability into the solution by imposing smoothness constraints on the image and PSF, respectively. We formulate a spatially adaptive regularization scheme by introducing the functional below:

$$\begin{aligned} R(\mathbf{f}) &= \sum_{(x,y) \in S_f} \alpha(x,y) [c(x,y) * f(x,y)]^2 = \|\mathbf{A}\mathbf{C}\mathbf{f}\|^2; \\ R(\mathbf{h}) &= \sum_{(x,y) \in S_h} \beta(x,y) [e(x,y) * h(x,y)]^2 = \|\mathbf{\Psi}\mathbf{E}\mathbf{h}\|^2 \end{aligned} \quad (3.2)$$

where $c(x,y)$ and $e(x,y)$ are the regularization filters to ensure smoothness of the solution, which can take the form of high-pass or impulse function. \mathbf{C} and \mathbf{E} are the BCCB matrices constructed from $c(x,y)$ and $e(x,y)$, respectively. α_i and β_i assign regularization parameters to the i th element in the image- and blur-domain, respectively. They serves two purposes: (i) assign spatially varying regularization parameters to different image areas to encourage detail preservation at the textured regions, and suppress noise in the smooth background, (ii) provide a compromise between data fidelity and regularization functionals. Let $diag(\cdot)$ denotes the diagonal matrix, \mathbf{A} and $\mathbf{\Psi}$ are diagonal matrices given as

$$\mathbf{A} = diag(\sqrt{\alpha_1}, \dots, \sqrt{\alpha_i}, \dots, \sqrt{\alpha_{MN}}); \quad \mathbf{\Psi} = diag(\sqrt{\beta_1}, \dots, \sqrt{\beta_i}, \dots, \sqrt{\beta_{PQ}}) \quad (3.3)$$

The last term $S(\mathbf{h})$ in (3.1) represents the soft parametric modeling term for the blur. It serves as a reinforcement learning term to integrate the potentially useful parametric structure of the blur. It is well-known that most blurs satisfy up to a certain degree of parametric structure. In view of this, we introduce the following soft modeling term for $S(\mathbf{h})$:

$$S(\mathbf{h}) = \sum_{(x,y) \in S_h} \gamma(x,y) [h(x,y) - h_p(x,y)]^2 = \|\mathbf{\Gamma}(\mathbf{h} - \mathbf{h}_p)\|^2 \quad (3.4)$$

where $\mathbf{\Gamma} = \text{diag}(\sqrt{\gamma_1}, \dots, \sqrt{\gamma_i}, \dots, \sqrt{\gamma_{PQ}})$. The weight parameters γ_i assign different emphases based on the relative difference between \mathbf{h} and \mathbf{h}_p . \mathbf{h}_p is the parametric estimate constructed from soft parametric models, which will be introduced in Section 3.4.

The main objective of this arrangement is to assess the relevance of current blur estimate \mathbf{h} with respect to parametric models, and integrate this knowledge progressively into the scheme if necessary. If the current blur \mathbf{h} resembles the parametric estimate \mathbf{h}_p closely, suggesting a strong likelihood that \mathbf{h} indeed belongs to a parametric structure, then the soft modeling term $S(\mathbf{h})$ will induce learning towards \mathbf{h}_p . In contrast, if \mathbf{h} differs from \mathbf{h}_p significantly, suggesting that \mathbf{h} may not belong to any predefined parametric blur types, then $S(\mathbf{h})$ will be small, and there will be little learning towards \mathbf{h}_p . This mechanism represents a flexible reinforcement learning paradigm where the parametric blur information is integrated only if it is relevant.

3.4 Manifold Soft Parametric Modeling

Blind image deconvolution algorithms can be classified broadly into two categories: parametric and nonparametric techniques. Parametric modeling techniques such as *a priori* blur identification assume that the PSF satisfies a known parametric structure. The scheme is developed specifically for the targeted blur structure, hence restricting its overall flexibility. In contrast, nonparametric methods do not utilize well-known blur knowledge, resulting in underutilization of the information available. Both classes of methods above adopt crisp logics implicitly, namely the parametric blur information is either incorporated fully or discarded totally. In view of this, we propose a novel manifold soft parametric modeling (MSPM) algorithm to resolve such dilemma.

The MSPM algorithm assesses the relevance of current blur \mathbf{h} with respect to parametric models, and integrates this knowledge progressively into the scheme. The block diagram of the MSPM scheme is given in Figure 3.2. It consists of three functional layers. The first layer is the neighbor generation layer where K nearest neighbors or manifolds $\{\mathbf{h}_1, \dots, \mathbf{h}_K\}$ are constructed from \mathbf{h} . The second layer is fuzzy membership estimation layer, which aims at evaluating the relevance of the parametric models $\{T_1, \dots, T_C\}$ with respect to $\{\mathbf{h}_1, \dots, \mathbf{h}_K\}$. The final layer performs weighted mean filtering to obtain the final parametric blur estimate \mathbf{h}_p based on their relative degree of relevance.

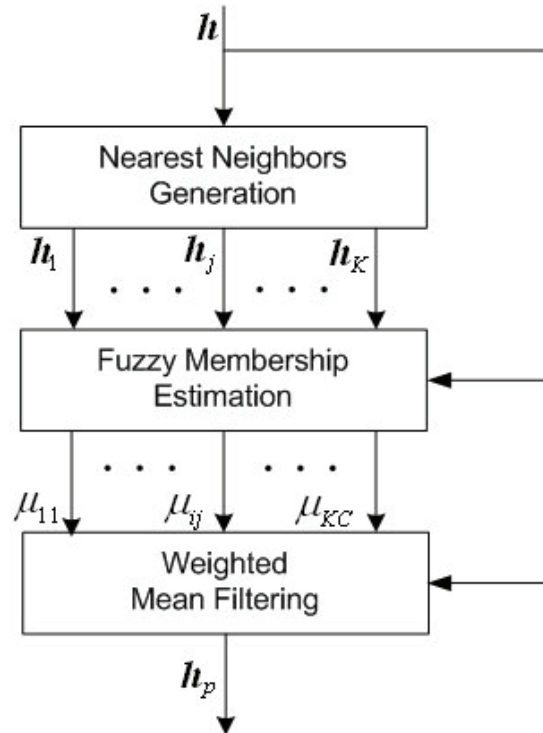


Figure 3.2 Manifold soft parametric modeling blur estimator.

3.4.1 Nearest Neighbors Generation

The K -nearest-neighbor (K -NN) rule is one of the most widely used classifying principles in

pattern recognition. K -NN rule implies that the input sample is classified according to its K nearest neighbors [42]-[44]. Throughout deconvolution, the coefficients of \mathbf{h} are susceptible to error due to uncertainty in joint estimation of blur and image. The only reliable information lies in the overall structure, or in other words, the low-frequency contents of \mathbf{h} . Therefore, the neighbor generation is based on its low-frequency information.

First, the 2-D DFT of \mathbf{h} is computed to produce $\tilde{\mathbf{H}}$.

Next, $\tilde{\mathbf{H}}$ is passed through different low-pass raised cosine filters $\mathbf{W}_j \{j=1, \dots, K\}$ [45]:

$$W_j(x, y) = \begin{cases} \frac{1}{2} \left\{ 1 + \cos \left[\frac{\pi}{\zeta_j} \left(\sqrt{\frac{x^2}{P^2} + \frac{y^2}{Q^2}} - \frac{1 - \zeta_j}{2} \right) \right] \right\}; & \sqrt{\frac{x^2}{P^2} + \frac{y^2}{Q^2}} \geq \frac{1 - \zeta_j}{2} \\ 1; & \text{otherwise} \end{cases} \quad (3.5)$$

where ζ_j is the roll-off factor. The raised cosine filters consist of unity gain at low frequencies, a raised cosine function in the middle, and total attenuation at high frequencies. The purpose of the roll-off factor ζ_j is to generate a 2-D weighting matrix to assign emphases to different frequency component. In other words, each nearest neighbor is generated by a weighting matrix, where this weighting matrix is produced by a specific ζ_j . Since the weighting matrices are desired to have different frequency emphasis, the sequence of ζ_j is ideally randomly distributed in the range of [0 1]. In the experiments, we use $\zeta_j = j/K$ in (3.5), where $j=1, \dots, K$ and K is the number of neighbors. For example, $\zeta_j = \{0.2, 0.4, 0.6, 0.8, 1.0\}$ when there are 5 nearest neighbors. Experimental results show that the algorithm is relatively insensitive to this roll-off factor.

Finally, 2-D inverse discrete Fourier transform (IDFT) is performed to generate the K -NN $\mathbf{h}_j \{j=1, \dots, K\}$. We will adopt $K = \sqrt{PQ}$ in our experiment.

3.4.2 Fuzzy Membership Estimation

We define a soft set Ω , consisting of parametric models as

$$\Omega = \{T_i(\theta)\}; \quad i = 1, \dots, C \quad (3.6)$$

where $T_i(\theta)$ represents the i th parametric model of the PSF with its defining parameters θ , and C is the number of blur models. We will focus our attention on some practical blur models in this work, namely Gaussian, uniform, and linear blurs:

$$\begin{aligned} T_g(\theta) &: \{T_g(x, y) = a \exp(-(x^2 + y^2)/(2\sigma^2))\} \\ T_u(\theta) &: \{T_u(x, y) = 1/a\} \\ T_l(\theta) &: \{T_l(x, y) = b - a\sqrt{x^2 + y^2}\} \end{aligned} \quad (3.7)$$

where a, b, σ are the model parameters of the PSF. The linear blur is implemented as a first-order approximation to the generic blur. We can extend the model set Ω to include other parametric models if desired.

We define μ_{ij} as the fuzzy membership or likelihood of the neighbor \mathbf{h}_j in resembling the i th parametric model $T_i(\theta)$. The first subscript i denotes the index of blur model, while the second subscript j represents the index of the nearest neighbor. It is assumed that $\chi = T_i(\theta) - \mathbf{h}_j$ is identically and independently distributed (iid) Gaussian noise with covariance matrix $\Sigma = \sigma_\chi^2 \mathbf{I}$. A maximum *a posteriori* (MAP) estimator is then employed to determine the best-fit model $T_{ij}(\theta^*)$ for \mathbf{h}_j :

$$\begin{aligned}
\mathbf{T}_{ij}(\boldsymbol{\theta}^*) &= \arg \max_{\boldsymbol{\theta}} P(\mathbf{T}_i(\boldsymbol{\theta}) | \mathbf{h}_j) \\
&= \arg \max_{\boldsymbol{\theta}} \log \left\{ \sqrt{\frac{1}{2\pi^{PQ} \det |\Sigma|}} \exp \left[-\frac{1}{2} (\mathbf{T}_i(\boldsymbol{\theta}) - \mathbf{h}_j)^T \Sigma^{-1} (\mathbf{T}_i(\boldsymbol{\theta}) - \mathbf{h}_j) \right] \right\} \\
&= \arg \max_{\boldsymbol{\theta}} \left\{ -\frac{1}{2} PQ \log(2\pi) - \frac{1}{2} PQ \log(\sigma_{\chi}^2) - \frac{1}{2\sigma_{\chi}^2} (\mathbf{T}_i(\boldsymbol{\theta}) - \mathbf{h}_j)^T (\mathbf{T}_i(\boldsymbol{\theta}) - \mathbf{h}_j) \right\}
\end{aligned} \tag{3.8}$$

where σ_{χ}^2 is the modeling noise. Next, the fuzzy membership of μ_{ij} is computed based on the Euclidean distance between \mathbf{h}_j and the corresponding MAP model $\mathbf{T}_{ij}(\boldsymbol{\theta}^*)$:

$$\mu_{ij} = \exp\left(-\frac{\|\mathbf{h}_j - \mathbf{T}_{ij}(\boldsymbol{\theta}^*)\|^2}{2\text{tr}(\boldsymbol{\Sigma}_{ee})}\right) \tag{3.9}$$

3.4.3 Weighted Mean Filtering

We will introduce a membership function $\mu_i(\mathbf{h})$ to determine the membership of \mathbf{h} belonging to the i th parametric blur model. The membership function is:

$$\mu_i(\mathbf{h}) = \frac{\sum_{j=1}^K \mu_{ij} (1 / \|\mathbf{h} - \mathbf{h}_j\|^2)}{\sum_{j=1}^K (1 / \|\mathbf{h} - \mathbf{h}_j\|^2)}; \quad i = 1, \dots, C \tag{3.10}$$

The likelihood function $\mu_i(\mathbf{h})$ depends on two factors: (i) membership value of the blur manifold μ_{ij} , and (ii) the distance between \mathbf{h} and its neighbor \mathbf{h}_j . It is based on the notion that those neighbors that are closer to \mathbf{h} should be assigned greater weight in the computation of $\mu_i(\mathbf{h})$.

The final output parametric blur \mathbf{h}_p is obtained from the parametric blur models using:

$$\mathbf{h}_p = \frac{\mu_0(\mathbf{h})\mathbf{h} + \sum_{i=1}^C \mu_i(\mathbf{h})\mathbf{T}_i(\boldsymbol{\theta}^*)}{\sum_{i=0}^C \mu_i(\mathbf{h})} \quad (3.11)$$

where $\mu_0(\mathbf{h}) = 1 - \max_{i=1, \dots, C} (\mu_i(\mathbf{h}))$, and $\mathbf{T}_i(\boldsymbol{\theta}^*)$ is the optimal parametric model which is computed based on \mathbf{h} using (3.8)

$$\mathbf{T}_i(\boldsymbol{\theta}^*) = \arg \max_{\boldsymbol{\theta}} P(\mathbf{T}_i(\boldsymbol{\theta}) | \mathbf{h}); \quad i = 1, \dots, C \quad (3.12)$$

The proposed MSPM algorithm employs a fuzzy K -NN notion in estimating the final blur estimate. As opposed to finding a single best-fit structure, the MSPM algorithm generates multiple parametric models to the current blur based on K -NN rule. This approach is consistent with the notion that the current blur can only be described in terms of likelihood, rather than absolute certainty, in assuming any parametric structure. In addition, the new scheme will allow the construction of a representative solution space where more blur structures can be incorporated.

3.5 Optimization Procedure

The cost function in (3.1) consists of image- and blur-domain terms. As it is computationally intensive to perform joint optimization, the optimization procedure called alternating minimization (AM) is then extended to minimize them iteratively [14], [31]. We project the overall cost function $J(\mathbf{f}, \mathbf{h})$ into the image-domain cost function $J(\mathbf{f} | \mathbf{h})$, and the blur-domain cost function $J(\mathbf{h} | \mathbf{f})$. The optimization procedure can be summarized as:

- (i) Initialize $\mathbf{h}^{(0)}$, $\mathbf{f}^{(0)}$
- (ii) Minimize the i th iterative cost functions:

$$J_i(\mathbf{f} | \mathbf{h}) = \|\mathbf{g} - \mathbf{H}\mathbf{f}\|^2 + \|\mathbf{A}\mathbf{C}\mathbf{f}\|^2 \quad (3.13)$$

$$J_i(\mathbf{h} | \mathbf{f}) = \|\mathbf{g} - \mathbf{H}\mathbf{f}\|^2 + \|\mathbf{\Psi}\mathbf{E}\mathbf{h}\|^2 + \|\mathbf{\Gamma}(\mathbf{h} - \mathbf{h}_p)\|^2 \quad (3.14)$$

(iii) Stop when termination condition is satisfied.

The cost functions $J(\mathbf{f} | \mathbf{h})$ and $J(\mathbf{h} | \mathbf{f})$ can be shown to be quadratic with positive semi-definite Hessian matrices. It follows that $J(\mathbf{f} | \mathbf{h})$ and $J(\mathbf{h} | \mathbf{f})$ are convex functions, which ensure convergence in their respective domains. A more thorough treatment of convergence analysis on general AM is given in [46].

The overview of the proposed PDR algorithm is given in Figure 3.3. Two relevant issues in PDR deconvolution scheme include: (i) blur support size estimation, and (ii) generation of the MSPM blur estimate. We have already developed MCSC, MASD, and MAAD to address the first issue in Chapter 2. A MSPM algorithm is developed to solve the second issue in previous section. The AM procedure is then employed in conjunction with conjugate gradient optimization (CGO) to perform blur identification and image restoration iteratively. Therefore, The iterative minimization scheme of PDR consists of outer loop of AM, where each AM iteration contains two inner loops of image- and blur-domain CGO.

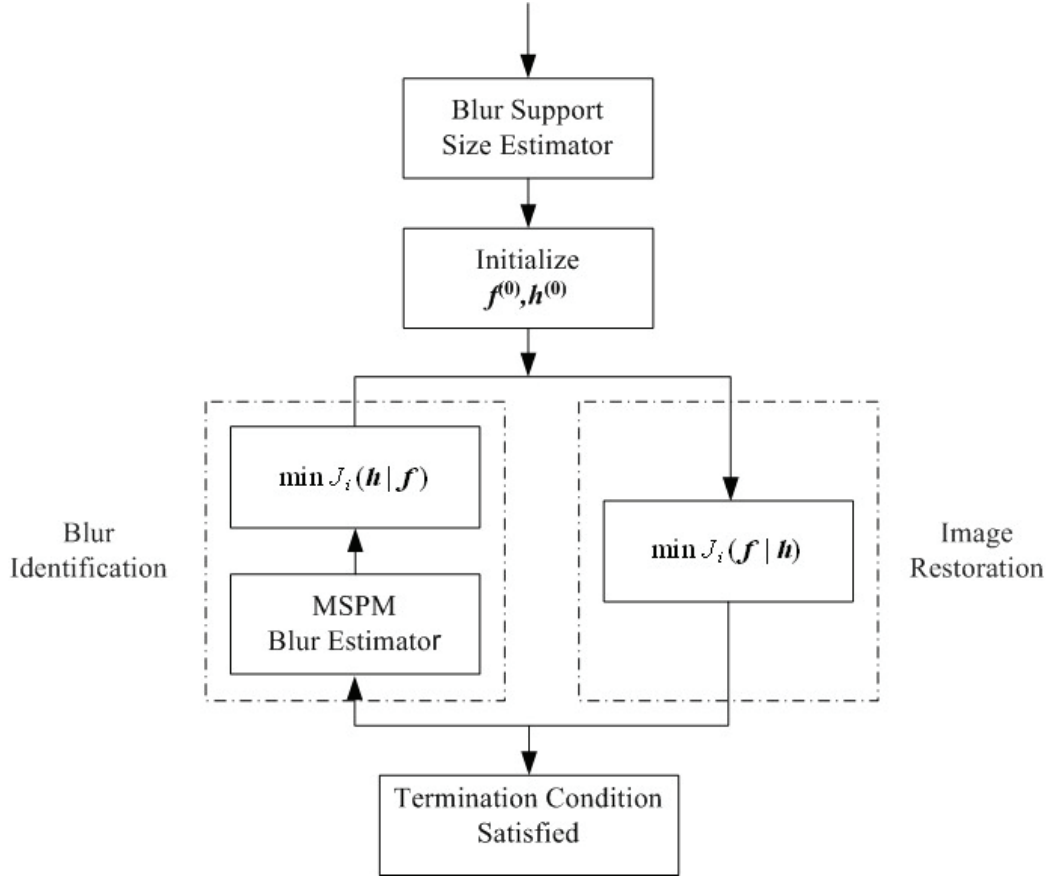


Figure 3.3 Overview of parametric double regularization scheme.

The proposed PDR algorithm is different from the SDR method in several aspects. Firstly, the SDR method decomposes blind image deconvolution into two symmetric processes of image deconvolution and blur identification. It does not consider the unique characteristics of blur domain. This is inconsistent with practical applications as many real-world PSFs satisfy up to a certain degree of parametric structure. Secondly, most PSFs exist in the form of low-pass filters. Thirdly, the SDR method employs a heuristic ITP to estimate the blur support, which is sensitive to pruning threshold and regularization schemes. The proposed PDR algorithm attempts to address these asymmetries by integrating parametric blur information into the scheme. Moreover, the blur support is identified prior to the deconvolution process. These observations above highlight the importance of performing image deconvolution and blur

identification according to their characteristics.

3.5.1 Minimization of Blur-Domain Cost Function

CGO is used in conjunction with AM to optimize the image- and blur-domain cost functions. The steepest descent method uses local gradient and tends to search in the same directions repeatedly, leading to very slow convergence. CGO utilizes conjugate direction at each step to search for the minima and can achieve faster convergence when compared with steepest descent method. Furthermore, the resulting conjugate search directions implicitly accumulate information about the Hessian matrix as iterations proceed. Compared to Newton's method, CGO does not require explicit second partial derivatives in Hessian matrix. It requires less storage requirement and computational complexity when compared with Newton's method [48]. Therefore, CGO is ideal in this large-scale optimization application, leading to fast convergence in a small number of iterations.

The formulation involved in the optimization of $J(\mathbf{h}|\mathbf{f})$ is derived in this subsection. The gradient of $J(\mathbf{h}|\mathbf{f})$ in (3.14) with respect to \mathbf{h} is given by:

$$\nabla_{\mathbf{h}} J = \frac{J(\mathbf{h}|\mathbf{f})}{\partial \mathbf{h}} = 2\mathcal{F}^H(\mathcal{F}\mathbf{h} - \mathbf{g}) + 2\mathbf{E}^H\mathbf{\Psi}^2\mathbf{E}\mathbf{h} + 2\mathbf{\Gamma}^2(\mathbf{h} - \mathbf{h}_p) \quad (3.15)$$

where \mathcal{F} is the stacked matrix formed by the estimated image \mathbf{f} as in (2.29).

The mathematical formulations of blur identification based on CGO are developed as follows:

(i) Initialize the conjugate vector \mathbf{q} :

$$\mathbf{q}^{(0)} = -\nabla_{\mathbf{h}} J^{(0)} \quad (3.16)$$

(ii) Update the $(k+1)$ th iteration blur estimate:

$$\mathbf{h}^{(k+1)} = \mathbf{h}^{(k)} + \eta^{(k)} \mathbf{q}^{(k)}, \quad \text{where} \quad \eta^{(k)} = \frac{\|\nabla_{\mathbf{h}} J^{(k)}\|^2}{\|\mathcal{F}^{(k)} \mathbf{q}^{(k)}\|^2 + \|\Psi \mathbf{E} \mathbf{q}^{(k)}\|^2 + \|\Gamma \mathbf{q}^{(k)}\|^2} \quad (3.17)$$

(iii) Update the $(k+1)$ th iteration conjugate vector:

$$\mathbf{q}^{(k+1)} = -\nabla_{\mathbf{h}} J^{(k)} + \rho^{(k)} \mathbf{q}^{(k)}, \quad \text{where} \quad \rho^{(k)} = \frac{\|\nabla_{\mathbf{h}} J^{(k+1)}\|^2}{\|\nabla_{\mathbf{h}} J^{(k)}\|^2} \quad (3.18)$$

(iv) Impose the blur constraints:

$$\sum_{(x,y) \in S_h} h(x,y) = 1; \quad h(x,y) > 0 \quad (3.19)$$

(v) Repeat steps (ii) to (iv) until convergence or a maximum number of iterations is reached.

3.5.2 Minimization of Image-Domain Cost Function

The gradient of $J(\mathbf{f} | \mathbf{h})$ with respect to \mathbf{f} is given by:

$$\nabla_{\mathbf{f}} J = \frac{\partial J(\mathbf{f} | \mathbf{h})}{\partial \mathbf{f}} = 2\mathbf{H}^H (\mathbf{H}\mathbf{f} - \mathbf{g}) + 2\mathbf{C}^H \mathbf{A}^2 \mathbf{C} \mathbf{f} \quad (3.20)$$

The mathematical formulations of image deconvolution based on CGO are developed as follows:

(i) Initialize the conjugate vector \mathbf{q} :

$$\mathbf{q}^{(0)} = -\nabla_{\mathbf{f}} J^{(0)} \quad (3.21)$$

(ii) Update the $(k+1)$ th iteration image estimate:

$$\mathbf{f}^{(k+1)} = \mathbf{f}^{(k)} + \eta^{(k)} \mathbf{q}^{(k)}, \quad \text{where} \quad \eta^{(k)} = \frac{\|\nabla_{\mathbf{f}} J^{(k)}\|^2}{\|\mathbf{H} \mathbf{q}^{(k)}\|^2 + \|\mathbf{A} \mathbf{C} \mathbf{q}^{(k)}\|^2} \quad (3.22)$$

(iii) Update the $(k+1)$ th iteration conjugate vector:

$$\mathbf{q}^{(k+1)} = -\nabla_f J^{(k)} + \rho^{(k)} \mathbf{q}^{(k)}, \quad \text{where} \quad \rho^{(k)} = \frac{\|\nabla_f J^{(k+1)}\|^2}{\|\nabla_f J^{(k)}\|^2} \quad (3.23)$$

(iv) Impose the image constraint

$$0 \leq f(x, y) \leq 255; \quad (x, y) \in S_f \quad (3.24)$$

(v) Repeat steps (ii) to (iv) until convergence or a maximum number of iterations is reached.

3.6 Experimental Results

The effectiveness of the PDR algorithm is illustrated through deconvolution of several degraded images under various conditions. The blur support is identified prior to the deconvolution process using the proposed techniques in Chapter 2. For MSPM, we select three practical blur models, namely Gaussian, uniform, and linear blurs in (3.7). After generating the K -NN of the current estimated blur, the parametric blur estimate \mathbf{h}_p is produced by (3.11). The weight assignment for the regularization term has been studied extensively in previous literatures [14], [40], [41]. The regularization parameters and soft error term are given as: $\alpha_i = 0.5 / (1 + 10^3 \text{var}_f(i))$, $\beta_i = 10^6 / (1 + 10^3 \text{var}_h(i))$, and $\gamma_i = 10^6 / (1 + 10^3 \text{var}_{h-h_p}(i))$, where $\text{var}_f(i)$, $\text{var}_h(i)$, $\text{var}_{h-h_p}(i)$ denote the normalized local variance of \mathbf{f} , \mathbf{h} , $\mathbf{h} - \mathbf{h}_p$. We have also tried different weight assignments to determine the suitable weighting scheme for the soft MSPM error term. We observe empirically that as long as the contribution between the regularization term and the soft MSPM terms are within the same order of magnitude, the deconvolution results will remain satisfactory. In view of this, we suggest a similar weight assignment scheme for β_i and γ_i due to its simplicity.

The number of iteration for AM and CGO are set to 5 and 10, and the procedure consisting of

blur identification with MSPM and image deconvolution is run. To evaluate the efficiency of the PDR algorithm, a performance measure called peak signal-to-noise ratio (PSNR) is employed. We further evaluate the efficiency of PDR by comparing it with the SDR method [14]. Both methods are run with the same initial conditions and regularization schemes.

3.6.1 Blind Deconvolution of Image Degraded by a Uniform PSF

The 256×256 “Cameraman” image shown in Figure 3.4(a) is degraded by 7×7 uniform blur to produce Figure 3.4(b). The MCSC, MAAD, and MASD sequences of the filtered image in the vertical and horizontal directions are given in Figure 3.4(e) and (f). We observe from Figure 3.4(e) that the criterion achieves the minima or maxima at $m=7$, which is the actual blur support in the vertical direction. Similarly, the criterion reaches the minima or maxima at $n=7$ in the horizontal direction as shown in Figure 3.4(f). Therefore, the MCSC, MAAD, and MASD have correctly identified the support of the PSF as 7×7 . After that, we initialize the PSF with impulse function based on the estimated support size. We apply MSPM in conjunction with AM to perform joint blur identification and image deconvolution. The final restored image is given in Figure 3.4(c). It can be observed that the overall sharpness of the image has been recovered. Significant amount of details has also been restored in the textured and edge regions.

Next, we compare our result with that obtained using the SDR method. The initial blur size for SDR is set to 11×11 , and the ITP is employed to estimate the blur support. The restored image by SDR is shown in Figure 3.4(d). Comparison reveals that our approach is superior in preserving details in the textured regions, while suppressing ringing in the smooth background. This is supported by objective performance measure as our method offers a PSNR of 30.15 dB, compared to 28.28 dB obtained by using the SDR method. The good

performance is due to the effectiveness of the MCSC method in estimating the PSF support, and the MSPM algorithm in integrating the soft parametric blur information. Both these factors result in satisfactory restored image quality.

3.6.2 Blind Deconvolution of Image Degraded under Noisy Conditions

Blind deconvolution of noisy degraded image is a challenging problem. The “Lena” image shown in Figure 3.5(a) is degraded by 5×5 Gaussian blur (standard deviation, $\sigma = 2.5$), followed by 30 dB noise to produce Figure 3.5(b). The PDR algorithm is employed as previously to identify the blur and restore the image. The PDR restored result is given in Figure 3.5(c). It is observed that most visual clarity has been recovered, especially near the feather and hat regions. Next, we compare our result with that obtained using the SDR method. The restored image by SDR is shown in Figure 3.5(d). Comparison reveals that our approach is better as our method offers a PSNR of 31.68 dB, compared to 29.26 dB obtained by using the SDR method.



(a)



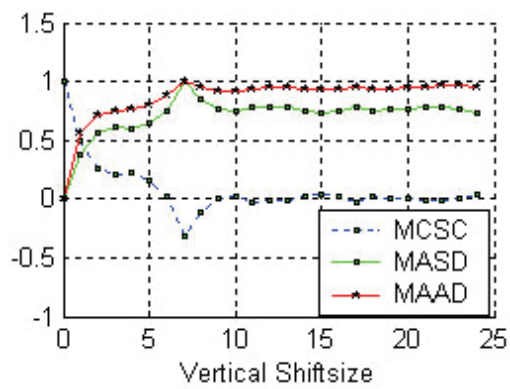
(b)



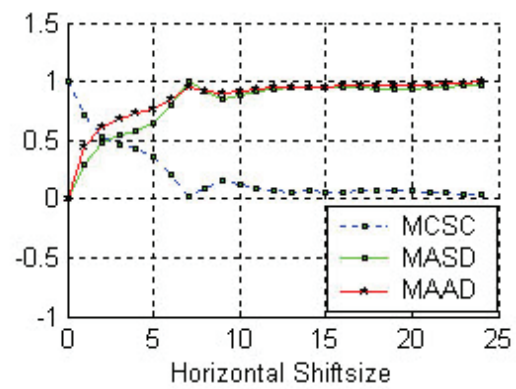
(c)



(d)



(e)



(f)

Figure 3.4 Blind deconvolution of image degraded by a uniform PSF. (a) Original image, (b) Degraded Image, (c) PDR restored image, (d) SDR restored image, (e) MCSC, MASD and MAAD profiles in the vertical direction, (f) MCSC, MASD and MAAD profiles in the horizontal direction.



Figure 3.5 Blind deconvolution of image degraded by a Gaussian PSF with additive noise. (a) Original image, (b) Degraded Image, (c) PDR restored image, (d) SDR restored image.

3.6.3 Blind Deconvolution of Image Degraded by Different PSFs

We illustrate the robustness of the proposed PDR method under different conditions: blur sizes, noise levels, and blur types in this subsection. The “Lena” image is selected as the test image again. The final results are tabulated in Table 3.1. The PDR scheme has achieved satisfactory image deconvolution, as reflected by good PSNR values. It is effective in restoring images under different blur sizes (5×5 , 7×7), different blur types (Gaussian, uniform, linear) in (3.7), and different noise levels (noiseless, 30dB). Further, it is observed that PDR consistently outperforms the SDR method. This demonstrates the robustness of our method in performing blind deconvolution under various conditions and constraints.

TABLE 3.1 BLIND IMAGE DECONVOLUTION RESULTS

Original PSF			PSNR (noiseless)		PSNR (noise at 30 dB)	
Size	Type	Parameter	PDR	SDR	PDR	SDR
5×5	Gaussian	$\sigma = 2.0$	31.69	29.63	31.06	29.24
	Uniform	NA	31.89	30.02	30.44	28.57
	Linear	$a = 0.004$	31.46	29.93	30.15	29.34
7×7	Gaussian	$\sigma = 3.0$	30.42	29.28	29.22	28.45
	Uniform	NA	31.65	29.55	30.30	29.04
	Linear	$a = 0.005$	31.21	30.50	30.62	28.57

Next, we give a set of images degraded by Gaussian PSF (5×5 , standard deviation, $\sigma = 2.5$), followed by 40dB noise. The proposed PDR approach is applied to restore the image and the result is shown in Figure 3.6. It is observed that significant amount of details has been recovered in the restored images.

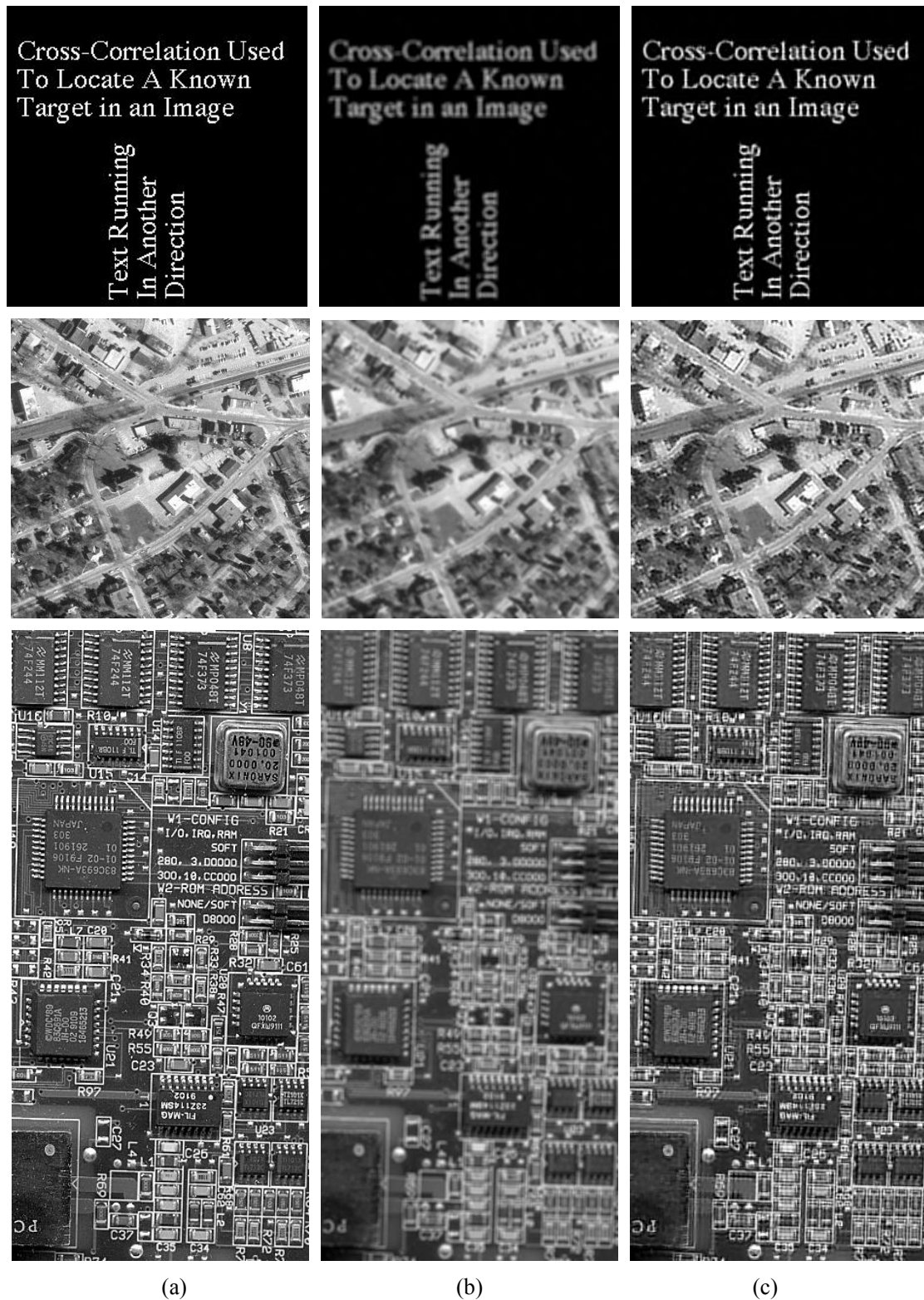


Figure 3.6 Examples of blind image deconvolution results. (a) Original image, (b) Degraded image, (c) Restored image.



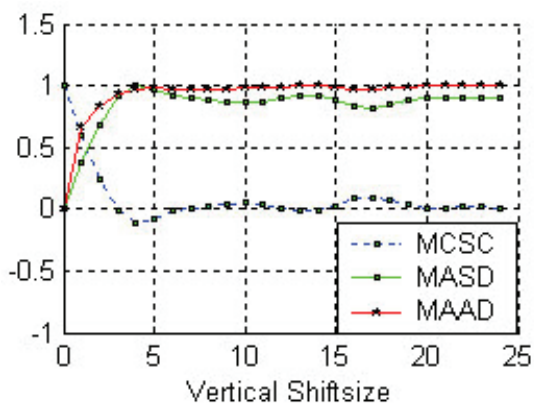
(a)



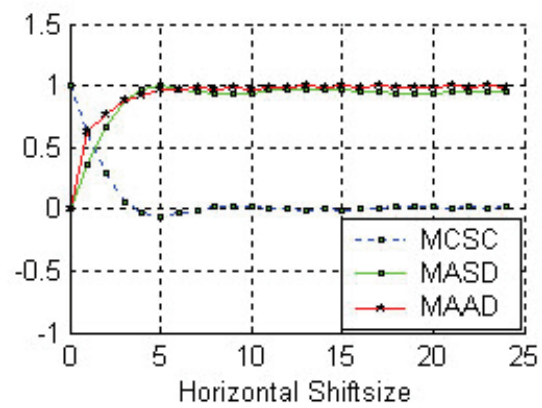
(b)



(c)



(d)



(e)

Figure 3.7 Blind deconvolution of real-life image. (a) Naturally blurred Image, (b) PDR restored image, (c) SDR restored image, (d) MCSC, MASD and MAAD profiles in the vertical direction, (e) MCSC, MASD and MAAD profiles in the horizontal direction.

3.6.4 Blind Deconvolution of Real-Life Blurred Image

A real-life blurred color image of sized 640×480 pixels is captured using a digital camera (Cannon IXUS v3). The image is a shell lying on a piece of paper with some texts, as shown in Figure 3.7(a). We use MCSC, MASD, and MAAD to identify the blur support in this experiment. From the figures, it can be observed that the estimated blur supports is 4×5 . To facilitate the implementation of image restoration where blur support is usually taken as odd number, we have determined the next-best blur support estimate to be 5×5 . The restored image by the PDR algorithm is given in Figure 3.7(b). It can be observed that the overall quality of the image has been improved. In contrast, the SDR restored image is shown in Figure 3.7(c). By comparing the restored images shown in Figure 3.7 (b) and (c), it is obvious that the PDR algorithm is better than SDR as there is little ringing or amplification of noise in the smooth backgrounds. This illustrates that the PDR method is instrumental in handling real-life image deconvolution.

3.7 Summary

We have proposed a PDR approach for blind image deconvolution based on soft integration of manifold blur parametric modeling. The new scheme integrates the parametric information of the blur structures progressively throughout deconvolution. The blind deconvolution problem is formulated into an AM procedure of blur identification and image deconvolution. This improves the convergence rate greatly, leading to significant reduction in computational cost. As opposed to other blind algorithms, the proposed technique is flexible as it has the following characteristics: (i) it can identify the blur support, (ii) it can incorporate readily many well known parametric PSFs such as motion, uniform, and Gaussian blurs into the

scheme, (iii) it can be tailored flexibly to include other blur types if some prior parametric knowledge of the blur is available, (iv) in the event that the actual blur does not satisfy any parametric models, the method has the flexibility to ignore the soft MSPM learning term, and determine the blur based on the combination of least-square data fidelity and regularization term.

Chapter 4

Multichannel Recursive Filtering for Deconvolution

4.1 Introduction

In many applications such as remote sensing and microscopy imaging, multiple degraded images of a single scene become available while the PSF of each channel remains unknown.

The single-input multiple-output (SIMO) model for multichannel degradation is shown in

Figure 4.1. Therefore, the recovery of the original scene from its multiple observations is required and this problem is, commonly, referred to as multichannel blind image deconvolution.

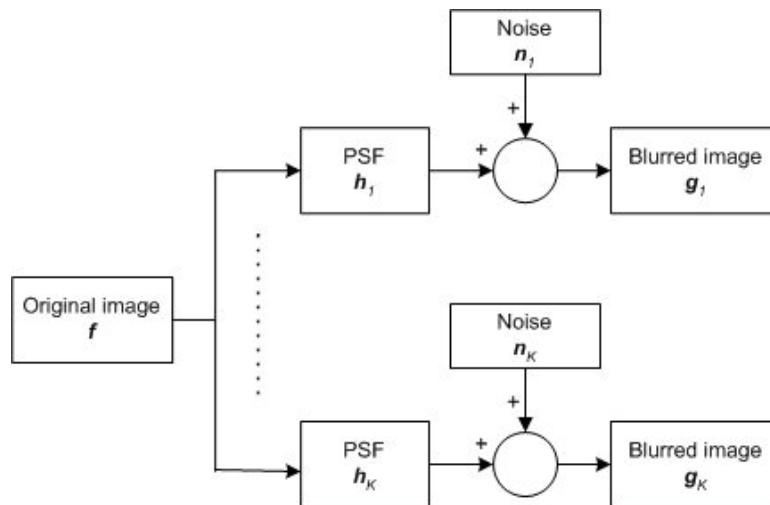


Figure 4.1 Multichannel blurring model.

Processing multichannel images is more complicated than processing single channel image due to the higher dimensionality of the problem. Similar to single-input single-output (SISO) deconvolution in Chapter 2, the key feature in multichannel deconvolution is that PSFs are unknown *a priori*. It is worth mentioning that the ill-posed nature of deconvolution is improved due to that the information lost in one channel may be compensated from the other channel. In other words, the quality of the restored image through SIMO model is normally better than that of SISO model. The more channels we have, the better the deconvolution result is.

The organization for the rest of this chapter is outlined as follows. Section 4.2 reviews the methods for multichannel blind image deconvolution. Section 4.3 provides a brief discussion on the cost function formulation. In Section 4.4, the development of recursive image deconvolution algorithm is presented. In Section 4.5, issues related to the selection of regularization parameters and forgetting factor are discussed. Simulation results are given in Section 4.6. In Section 4.7, conclusions and further remarks are drawn.

4.2 Literature Review

Early efforts for multichannel deconvolution are centered on non-blind restoration of noisy blurred images by using Wiener filtering [49]-[51], constrained least squares [52]-[55], and Bayesian methods [56], [57].

With the assumption that the multichannel PSFs are weakly co-prime, and in the absence of noise, the desired image and PSFs can be transformed into the null-space of a special matrix constructed from the degraded images [58]-[61]. Centered on this idea, several techniques have been proposed which include greatest common divisor (GCD) [58], subspace-based

[59], [60], and eigenstructure-based approaches [61]. The GCD method is based on the notion that the desired image can be regarded as the polynomial GCD among the degraded images in the z -domain. Subspace-based methods work by first estimating the PSF using a procedure of min-eigenvector, followed by conventional image restoration using the identified PSFs. In similar concept, eigenstructure-based algorithm transforms the nullspace problem into a constrained optimization framework and performs direct *deconvolver* estimation. The aforementioned nullspace-based methods, however, suffer from noise amplification, which often lead to poor solutions in the noisy environments.

There are some successful works on the development of multichannel deconvolution, which exploit the features of SISO deconvolution algorithms. These techniques develop a cost function within the framework of constrained least squares minimization. The iterative alternating minimization (AM) strategy is used to minimize the cost function. The minimization step involves two processes of blur identification and image restoration centered on the principle of projection-onto-convex-sets (POCS). The AM strategy is first proposed in [31] along with POCS and extended to double *Tikhonov* regularization for SISO deconvolution in [14]. SDR [62] and Gauss-Markov random fields [63] have also been applied in multichannel blind image deconvolution. A promising attempt has been made by utilizing the blur null-space as the regularization term in the framework of total variation (TV) [64]. Recently, the extension of the Bussgang blind equalization algorithm to iterative multichannel deconvolution has been proposed in [65]. The basic idea is focused on Wiener filtering of the observed degraded images, and updating the filters using a nonlinear Bayesian estimation of the estimated image. Generally speaking, these iterative methods are the extensions of SISO blind image deconvolution approaches. Therefore, if a new degraded image becomes available at a later stage, the iterative schemes will require a complete re-run, rather than a recursive process to update the estimate. This is, clearly, inflexible and

computationally inefficient.

In view of this, we develop a new and efficient algorithm called multichannel recursive filtering (MRF) to address blind multichannel image deconvolution. The estimated image is recursively updated from the previous estimate using a regularization framework. All the operations of MRF are performed in DFT domain, giving rise to fast and simple implementation. The multichannel PSFs are identified iteratively using conjugate gradient optimization (CGO). The proposed algorithm introduces a forgetting factor to discard the old unreliable estimates, hence achieving better convergence performance. A key feature of the method is its computational simplicity and efficiency. This allows the new method to be adopted readily in real-life applications.

4.3 Development of Cost Function

In this work, we are interested in the SIMO multichannel blind image deconvolution problem. Considering the SIMO linear degradation system that consists of K measurements of the original image \mathbf{f} , the observed degraded image of the i th-channel can be modeled as:

$$\mathbf{g}_i = \mathbf{h}_i * \mathbf{f} + \mathbf{n}_i, \quad i = 1, 2, \dots, K \quad (4.1)$$

where \mathbf{g}_i , \mathbf{h}_i , and \mathbf{n}_i represent the degraded image, PSF, and noise of the i th-channel, respectively. To tackle the ill-posed nature of image deconvolution, *Tikhonov* regularization theory has been employed in the deconvolution scheme, as it is effective in detail preservation and noise suppression. The regularization principle has been extended to a SDR framework that imposes smoothness constraint in both the image- and blur domains. In terms of the i th-channel, it can be described by [52], [53]:

$$\|\mathbf{g}_i - \mathbf{h}_i * \mathbf{f}\|^2 = \|\mathbf{n}_i\|^2 \leq \varepsilon_i^2; \quad \|\mathbf{c} * \mathbf{f}\|^2 \leq \kappa^2; \quad \|\mathbf{e}_i * \mathbf{h}_i\|^2 \leq \delta_i^2 \quad (4.2)$$

where ε_i , κ , δ_i are the upper bounds related to the noise, image and PSF terms, respectively. \mathbf{c} and \mathbf{e}_i are the regularization operators and usually take the form of a high-pass filter. The first term in (4.2) is the data-fidelity term, while the second and third terms are the regularization functionals that impose smoothness constraints on the image- and blur-domains respectively. In order to perform joint blur identification and image deconvolution for multichannel problem, the following cost function, in similar fashion to (3.1), is formulated over K channels:

$$J(\mathbf{f}, \mathbf{h}) = \sum_{i=1}^K \left(\|\mathbf{g}_i - \mathbf{h}_i * \mathbf{f}\|^2 + \alpha_i \|\mathbf{c} * \mathbf{f}\|^2 + \beta_i \|\mathbf{e}_i * \mathbf{h}_i\|^2 \right) \quad (4.3)$$

where $\mathbf{h} = \{\mathbf{h}_1, \dots, \mathbf{h}_K\}$ is the multichannel blur. The cost function in (4.3) consists of the data fidelity term, and the image- and blur-domain regularization terms. α_i and β_i are the regularization parameters that offer a compromise between least-square fidelity error and the regularity of the solutions \mathbf{f} and \mathbf{h}_i . As it is computationally intensive to perform joint optimization to estimate image and blur simultaneously, an iterative strategy based on AM is adopted to project the overall cost function $J(\mathbf{f}, \mathbf{h})$ into the image-domain cost function $J(\mathbf{f} | \mathbf{h})$ and the blur-domain cost function $J(\mathbf{h} | \mathbf{f})$. The technique, however, suffers from potential poor local convergence, leading to ringing artifacts in the restored image. Further, if an extra degraded image (i.e. $(K+1)$ th measurement \mathbf{g}_{K+1}) becomes available at a later stage, the iterative schemes will require a complete re-run, rather than a recursive process to update the estimate.

4.4 Recursive Filtering for Multichannel Blind Deconvolution

4.4.1 Multichannel Recursive Filtering

The overall cost function in (4.3) consists of two sets of unknown variables: image and blur. As explained earlier, we project $J(\mathbf{f}, \mathbf{h})$ into the image-domain cost function $J(\mathbf{f} | \mathbf{h})$ by fixing the blurring filters \mathbf{h} to give:

$$J(\mathbf{f} | \mathbf{h}) = \sum_{i=1}^K \left(\|\mathbf{g}_i - \mathbf{h}_i * \mathbf{f}\|^2 + \alpha_i \|\mathbf{c} * \mathbf{f}\|^2 \right) \quad (4.4)$$

It is observed that (4.4) is a convex function with respect to \mathbf{f} .

Recursive filtering is widely used in 1-D signal processing due to its fast convergence rate, as compared with least mean squares (LMS) filtering [66]. Motivated by this consideration, we develop a new multichannel recursive filtering scheme to address the 2-D problem in this work. It is worth noting that, unlike the 1-D cases where *matrix inversion lemma* is used in the development of recursive least square filtering, the same approach cannot be applied in 2-D images due to significantly enhanced complexity. In view of this, we propose a MRF scheme that utilizes DFT to update the image estimate.

This formulation of the proposed MRF is outlined as follows.

Let $\mathbf{f}^{(n)} \{n=1, 2, \dots, K\}$ be the estimated image from the observed data $\{\mathbf{g}_1, \dots, \mathbf{g}_n\}$ at the n th recursive step. The estimated $\mathbf{f}^{(n+1)}$ can be updated by using the information contained in the newly received observation \mathbf{g}_{n+1} through:

$$\mathbf{f}^{(n+1)} = \mathbf{f}^{(n)} + \mathbf{u}^{(n+1)} \quad (4.5)$$

where $\mathbf{u}^{(n+1)}$ is the update term, to be derived in the later part of this subsection.

In the development of MRF, we introduce a *forgetting factor* λ into the cost function of

(4.4) to ensure that the data in the distant past are assigned less emphasis [66]. Thus, we can re-express (4.4) in the matrix-vector notation with the forgetting factor λ as:

$$\mathbf{f}^{(n)} = \min_{\mathbf{f}} \sum_{i=1}^n \lambda^{n-i} \left(\|\mathbf{g}_i - \mathbf{H}_i \mathbf{f}\|^2 + \alpha_i \|\mathbf{C} \mathbf{f}\|^2 \right) \quad (4.6)$$

where \mathbf{H}_i and \mathbf{C} are the block-circulant matrices that are constructed from \mathbf{h}_i and \mathbf{c} , respectively. It is worth mentioning that the special case of $\lambda = 1$ means *infinite memory* as the effect of past data is not attenuated. In contrast, the exponentially decaying memory channel ($\lambda < 1$) is used in time-varying environment.

The closed-form solution to the least squares problem in (4.6) using the pseudoinverse is given by:

$$\mathbf{f}^{(n)} = (\mathbf{R}^{(n)})^{-1} \mathbf{r}^{(n)} \quad (4.7)$$

where $\mathbf{R}^{(n)} = \sum_{i=1}^n \lambda^{n-i} (\mathbf{H}_i^H \mathbf{H}_i + \alpha_i \mathbf{C}_i^H \mathbf{C}_i)$ and $\mathbf{r}^{(n)} = \sum_{i=1}^n \lambda^{n-i} \mathbf{H}_i^H \mathbf{g}_i$.

When the cost function of (4.6) incorporates the available $(n+1)$ th channel, the estimate $\mathbf{f}^{(n+1)}$ is given as

$$\mathbf{f}^{(n+1)} = (\mathbf{R}^{(n+1)})^{-1} \mathbf{r}^{(n+1)} \quad (4.8)$$

where $\mathbf{R}^{(n+1)} = \lambda \mathbf{R}^{(n)} + \mathbf{H}_{n+1}^H \mathbf{H}_{n+1} + \alpha_{n+1} \mathbf{C}_{n+1}^H \mathbf{C}_{n+1}$ and $\mathbf{r}^{(n+1)} = \lambda \mathbf{r}^{(n)} + \mathbf{H}_{n+1}^H \mathbf{g}_{n+1}$. The $(n+1)$ th $\mathbf{f}^{(n+1)}$ depends on the $(n+1)$ th channel \mathbf{h}_{n+1} which is estimated from the blur identification step detailed in next subsection.

Substituting (4.5) and (4.7) into (4.8), it yields the update term $\mathbf{u}^{(n+1)}$ as

$$\mathbf{u}^{(n+1)} = (\mathbf{R}^{(n+1)})^{-1} (\mathbf{H}_{n+1}^H \mathbf{g}_{n+1} - (\mathbf{H}_{n+1}^H \mathbf{H}_{n+1} + \alpha_{n+1} \mathbf{C}_{n+1}^H \mathbf{C}_{n+1}) \mathbf{f}^{(n)}) \quad (4.9)$$

Hence, the $(n+1)$ th least squares estimate $\mathbf{f}^{(n+1)}$ can be computed recursively from its

previous estimate $\mathbf{f}^{(n)}$ using (4.5) and (4.9). However, the matrix $(\mathbf{R}^{(n+1)})^{-1}$ cannot be computed readily from $(\mathbf{R}^{(n)})^{-1}$ due to the huge computation cost associated with the inversion of the matrix $(\lambda \mathbf{R}^{(n)} + \mathbf{H}_{n+1}^H \mathbf{H}_{n+1} + \alpha_{n+1} \mathbf{C}_{n+1}^H \mathbf{C}_{n+1})^{-1}$ (dimension of $MN \times MN$, where $M \times N$ is the size of the image). To address this issue, we exploit the diagonalization properties of the 2-D DFT for BCCB matrix. The recursive filtering in spatial domain is transformed into the DFT domain. Let $\mathcal{F}[\cdot]$ denote the DFT operation, the cap “ \sim ” and $\omega = (\omega_x, \omega_y)$ are used to represent the signal in the frequency domain and the frequency pair along the X - and Y -axis, respectively. The proposed recursive multichannel deconvolution can be summarized as follows:

(i) Initialize the algorithm

$$\mathbf{f}^{(0)} = \mathbf{0}, \tilde{\mathbf{R}}^{(0)} = \mathbf{0}, \lambda \leq 1 \quad (4.10)$$

(ii) For the $(n+1)$ th channel, $n = 0, 1, \dots, K-1$,

Set α_{n+1} , \mathbf{c}_{n+1} , and calculate the DFT¹:

$$\tilde{\mathbf{f}}^{(n)} = \mathcal{F}[\mathbf{f}^{(n)}], \tilde{\mathbf{g}}_{n+1} = \mathcal{F}[\mathbf{g}_{n+1}], \tilde{\mathcal{H}}_{n+1} = \mathcal{F}[\mathbf{h}_{n+1}], \tilde{\mathbf{C}}_{n+1} = \mathcal{F}[\mathbf{c}_{n+1}] \quad (4.11)$$

(a) Update the old estimate recursively:

$$\tilde{\mathbf{f}}^{(n+1)}(\omega) = \tilde{\mathbf{f}}^{(n)}(\omega) + \frac{\tilde{\mathcal{H}}_{n+1}^H(\omega) \tilde{\mathbf{g}}_{n+1}(\omega) - (|\tilde{\mathcal{H}}_{n+1}(\omega)|^2 + \alpha_{n+1} |\tilde{\mathbf{C}}_{n+1}(\omega)|^2) \tilde{\mathbf{f}}^{(n)}(\omega)}{\tilde{\mathbf{R}}^{(n+1)}(\omega)} \quad (4.12)$$

where $\tilde{\mathbf{R}}^{(n+1)}(\omega) = \lambda \tilde{\mathbf{R}}^{(n)}(\omega) + |\tilde{\mathcal{H}}_{n+1}(\omega)|^2 + \alpha_{n+1} |\tilde{\mathbf{C}}_{n+1}(\omega)|^2$

(b) Calculate the IDFT and impose image constraint to obtain the estimated image:

¹ In Matlab, the 2-D DFT of the PSF and regularization operator is implemented using *psf2otf*, while for image, it is implemented using *fft2* function.

$$0 \leq \mathbf{f}^{(n+1)} = \mathcal{F}^{-1}[\tilde{\mathbf{f}}^{(n+1)}] \leq 255 \quad (4.13)$$

4.4.2 Blur Identification

Blur identification is a challenging problem in blind image deconvolution, involving the estimation of its support size and coefficients. The cost function involved in the blur coefficients estimation is given by:

$$\begin{aligned} J(\mathbf{h}_1, \dots, \mathbf{h}_K | \mathbf{f}) &= \sum_{i=1}^K \left(\|\mathbf{g}_i - \mathbf{h}_i * \mathbf{f}\|^2 + \beta_i \|\mathbf{e}_i * \mathbf{h}_i\|^2 \right) \\ &= \sum_{i=1}^K \left(\|\mathbf{g}_i - \mathbf{H}_i \mathbf{f}\|^2 + \beta_i \|\mathbf{E}_i \mathbf{h}_i\|^2 \right) \end{aligned} \quad (4.14)$$

The gradient of $J(\mathbf{h} | \mathbf{f})$ with respect to $\mathbf{h}_i \{i = 1, 2, \dots, K\}$ is given by:

$$\nabla_{\mathbf{h}_i} J^{(n)}(\mathbf{h}_1, \dots, \mathbf{h}_K | \mathbf{f}) = 2\mathcal{F}^H(\mathcal{F}\mathbf{h}_i - \mathbf{g}) + 2\beta_i \mathbf{E}_i^H \mathbf{E}_i \mathbf{h}_i \quad (4.15)$$

The mathematical formulations of blur identification have already been illustrated in Subsection 3.5.1 and summarized in Table 4.1.

TABLE 4.1 SUMMARY OF CONJUGATE GRADIENT OPTIMIZATION FOR BLUR IDENTIFICATION

(i) For the i th channel ($i = 1, 2, \dots, K$), initialize the conjugate vector by setting:

$$\mathbf{q}^{(0)} = -\nabla_{\mathbf{h}_i} J^{(n)}(\mathbf{h}_1, \dots, \mathbf{h}_K | \mathbf{f})$$

(ii) At the $(n+1)$ th CGO iteration, $n = 0, 1, \dots$

(a) Update the n th iteration blur estimate:

$$\mathbf{h}_i^{(n+1)} = \mathbf{h}_i^{(n)} + \eta^{(n)} \mathbf{q}^{(n)}, \text{ where } \eta^{(n)} = \frac{\|\nabla_{\mathbf{h}_i} J^{(n)}\|^2}{\|\mathcal{F}^{(n)} \mathbf{q}^{(n)}\|^2 + \beta_i \|\mathbf{E}_i \mathbf{q}^{(n)}\|^2}$$

(b) Update the n th conjugate vector:

$$\mathbf{q}^{(n+1)} = -\nabla_{\mathbf{h}_i} J^{(n)} + \rho^{(n)} \mathbf{q}^{(n)}, \text{ where } \rho^{(n)} = \frac{\|\nabla_{\mathbf{h}_i} J^{(n+1)}\|^2}{\|\nabla_{\mathbf{h}_i} J^{(n)}\|^2}$$

(iii) Repeat (ii) until convergence or a maximum number of iterations is reached.

4.4.3 Schematic Overview

The schematic overview of the proposed algorithm is given in Figure 4.2. This approach is to alternately minimize the cost function with respect to the common \mathbf{f} and the PSFs \mathbf{h}_i in each channel, respectively. The flowchart consists of two key steps. The first step performs recursive image restoration to yield $\mathbf{f}^{(i)}$ using $\mathbf{f}^{(i-1)}$, $\mathbf{R}^{(i-1)}$ and the new data of the i th-channel. The second step performs blur identification using the conjugate gradient minimization to reach the optimal solution \mathbf{h}_i .

Let K be the total number of channels, the inner loop of the procedure will run through the two steps alternately until data from all K channels have been computed. Unlike recursive filtering in 1-D adaptive filter design, multichannel image deconvolution does not have hundreds of measurements. Therefore, we propose to reuse the estimates $\mathbf{f}^{(0)} = \mathbf{f}^{(K)}$, $\mathbf{R}^{(0)} = \mathbf{R}^{(K)}$ from previous iteration in the outer loop to reiterate the inner loop till the

convergence is reached.

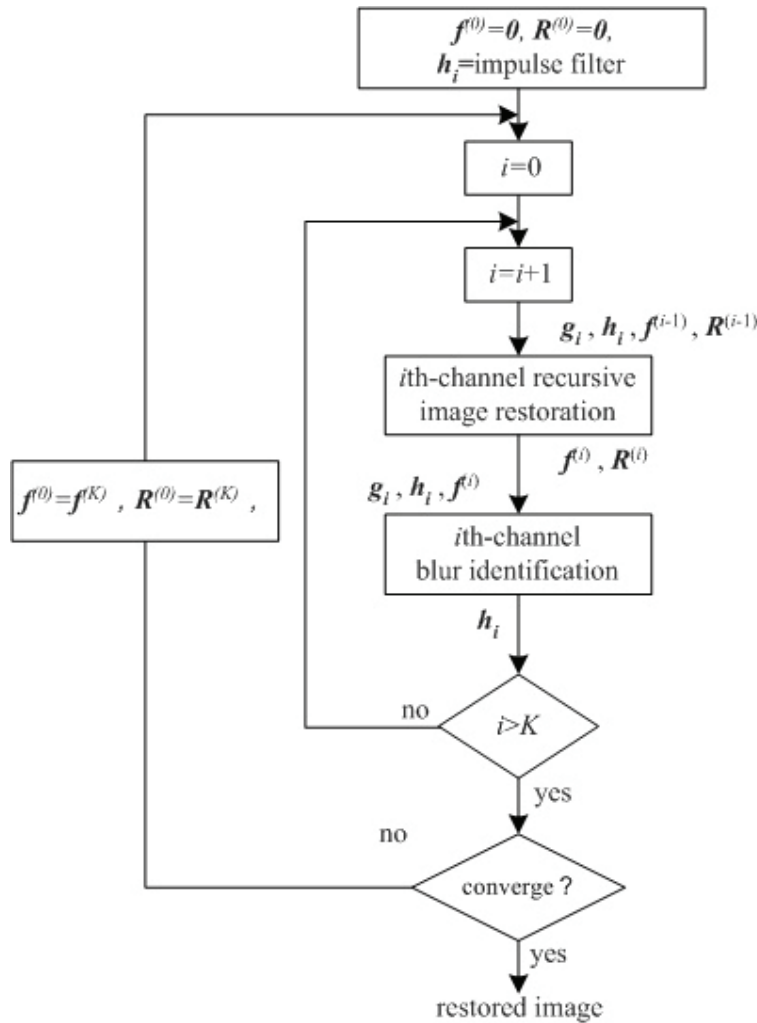


Figure 4.2 Schematic diagram of the proposed algorithm.

The novelty of this work is the recursive scheme in which the channel index is treated as a time index. It is worth mentioning that the proposed MRF for image restoration is performed in a fashion similar to Wiener filtering. It is, however, different from previous iterative schemes, which employ SDR-AM [62] or TV-AM [64] for the minimization of image-domain cost function. One advantage of the proposed algorithm is that it is flexible enough to update the old estimate when the new measurement becomes available later, i.e. the $K+1$ channel

becomes available after computation has been completed based on earlier K channels. Hence, the computational cost is greatly reduced due to two reasons: (i) recursive filtering updates the estimate based on first-come-first-serve basis, hence it does not require all the data to be available at once, and (ii) all the operations of MRF for image-domain minimization are conducted in the DFT domain.

4.5 Issues on MRF Parameters

4.5.1 Regularization Parameters and Operators

The regularization framework is instrumental in providing satisfactory results in image restoration. Let $\chi^{(n)}$ denote the residual error between $\tilde{f}^{(n)}$ in (4.7) and the original image f in (4.1). In the 2-D DFT domain, $\chi^{(n)}$ is given by:

$$\begin{aligned}\tilde{\chi}^{(n)}(\omega) &= \tilde{f}^{(n)}(\omega) - \tilde{f}(\omega) \\ &= \frac{\sum_{i=1}^n \lambda^{n-i} \tilde{\mathcal{H}}_i^H(\omega) \tilde{n}_i(\omega)}{\sum_{i=1}^n \lambda^{n-i} (|\tilde{\mathcal{H}}_i(\omega)|^2 + \alpha_i |\tilde{\mathcal{C}}(\omega)|^2)} - \frac{f(\omega) \sum_{i=1}^n \lambda^{n-i} \alpha_i |\tilde{\mathcal{C}}(\omega)|^2}{\sum_{i=1}^n \lambda^{n-i} (|\tilde{\mathcal{H}}_i(\omega)|^2 + \alpha_i |\tilde{\mathcal{C}}(\omega)|^2)}\end{aligned}\quad (4.16)$$

It can be observed that the error consists of two parts: the noise and the image terms. The first part is the noise term, which will be large for small $\tilde{\mathcal{H}}_i(\omega)$ if there is no regularization term $\alpha_i |\tilde{\mathcal{C}}(\omega)|^2$. Thus, $\alpha_i |\tilde{\mathcal{C}}(\omega)|^2$ will reduce the impact of noise term. However, this is at the cost of producing a small bias to the actual image. In order to make $\chi^{(n)}$ as small as possible, a reasonable compromise needs to be reached between these two terms through careful determination of regularization parameter and operator. Previous work on the selection of the regularization parameter includes *set theoretic* approach and generalized cross-validation [67]. We follow the idea of *set theoretic* [52], [53] to estimate the

regularization parameters α_i and β_i :

$$\alpha_i = \frac{\varepsilon_i^2}{\kappa^2} \approx \frac{MN\sigma_i^2}{\|\mathbf{c} * \mathbf{f}^{(0)}\|^2}; \quad \beta_i = \frac{\varepsilon_i^2}{\delta_i^2} \approx \frac{MN\sigma_i^2}{\|\mathbf{e}_i * \mathbf{h}_i^{(0)}\|^2} \quad (4.17)$$

where ε_i , κ , δ_i are the upper bounds related to the noise, image and PSF terms in (4.2).

σ_i^2 is the noise variance in the i th-channel, which can be estimated from the smooth regions of the image. The purpose of (4.17) is to explore the relationship between noise, image and PSF to choose the reasonable regularization parameters. In practice, the regularization parameters α_i and β_i are initialized and remained constant during AM procedure. We can use the estimated σ_i^2 , $\mathbf{f}^{(0)}$ and $\mathbf{h}_i^{(0)}$ to provides an order-of-magnitude estimate for the regularization parameters [62], [64], [67]. The simulation results show that the algorithm is robust towards different regularization parameters so long as they fall within a reasonable range.

The role of the regularization operator \mathbf{c} is to move the small magnitude term of $\tilde{\mathcal{H}}_i(\omega)$ away from the zeroes, while leaving the large values relatively unchanged. As PSF is generally a low-pass filter, \mathbf{c} should be taken as a high-pass filter or simply as an impulse function such as $\mathbf{C} = \mathbf{I}$, which impose smooth constraints on the images. The analysis on the regularization operator \mathbf{e}_i is similar to \mathbf{c} . In Appendix, an analysis on how the regularization result of (4.6) is affected by the error in the PSFs is investigated.

4.5.2 Forgetting Factor

The introduction of forgetting factor is centered on the observation that when the estimated image converges to the original one, the identified blur will approach the actual PSF in the

alternating minimization scheme. It can be observed from (4.6) that if the forgetting factor is $0 \leq \lambda < 1$, the scheme will diminish the older, less reliable estimated \mathbf{h}_i , and favor the later, more updated estimate. Generally speaking, λ should have small positive value for fast memory, and large positive value for slow memory. In this work, we let

$$\lambda = \zeta^{1/K} \quad (4.18)$$

where ζ is the memory attenuation rate.

4.6 Experimental Results

4.6.1 Multichannel Blind Deconvolution under Noisy Conditions

The effectiveness of the proposed method is illustrated under different blurring conditions. For performance evaluation, PSNR is chosen as the objective performance metric. In Figure 4.3(a), the original “Board” image of sized 256×256 is selected as the test image. The image is blurred by four 5×5 Gaussian blurs, corresponding to different values of $\sigma_i = \{2.0, 2.5, 3.0, 3.5\}$. Further, the blurred image is degraded under different noise levels to produce different SNR values $\{30\text{dB}, 33\text{dB}, 36\text{dB}, 40\text{dB}\}$. Through this, we can simulate four acquisition channels with variable PSFs and noise levels, as shown in Figure 4.3(b).

The proposed MRF algorithm is run to perform blind image deconvolution. All the degraded images are firstly preprocessed using the *edgetaper* function in Matlab to lessen the boundary effect. The forgetting factor is taken as $\lambda = \zeta^{1/K}$, where $\zeta = 0.05$ and $K = 4$. The regularization parameters are calculated according to (4.17), while the regularization operators are simply taken as $\mathbf{C} = \mathbf{I}$ and $\mathbf{D}_i = \mathbf{I}$. The PSFs are initialized to impulse functions, with the support estimated using the MCSC criterion. The outer-loop iteration

number is set to 10, while the CGO iteration for blur identification is 5.

The restored image using the proposed algorithm is shown in Figure 4.3(c). It is observed that the approach is effective in preserving detailed information, as demonstrated by the clear numbers on the board. The satisfactory subjective inspection of the image is supported by objective performance measure as our method offers a PSNR of 21.93 dB, compared to the average of 12.46 dB for the degraded images. Further, the profile of PSNR versus the number of iteration is given in Figure 4.3(d). It is noted that each outer-loop iteration comprises 4 inner-loop iterations for recursive image deconvolution. It can be observed from the figure that the algorithm achieves convergence in 6 iterations.

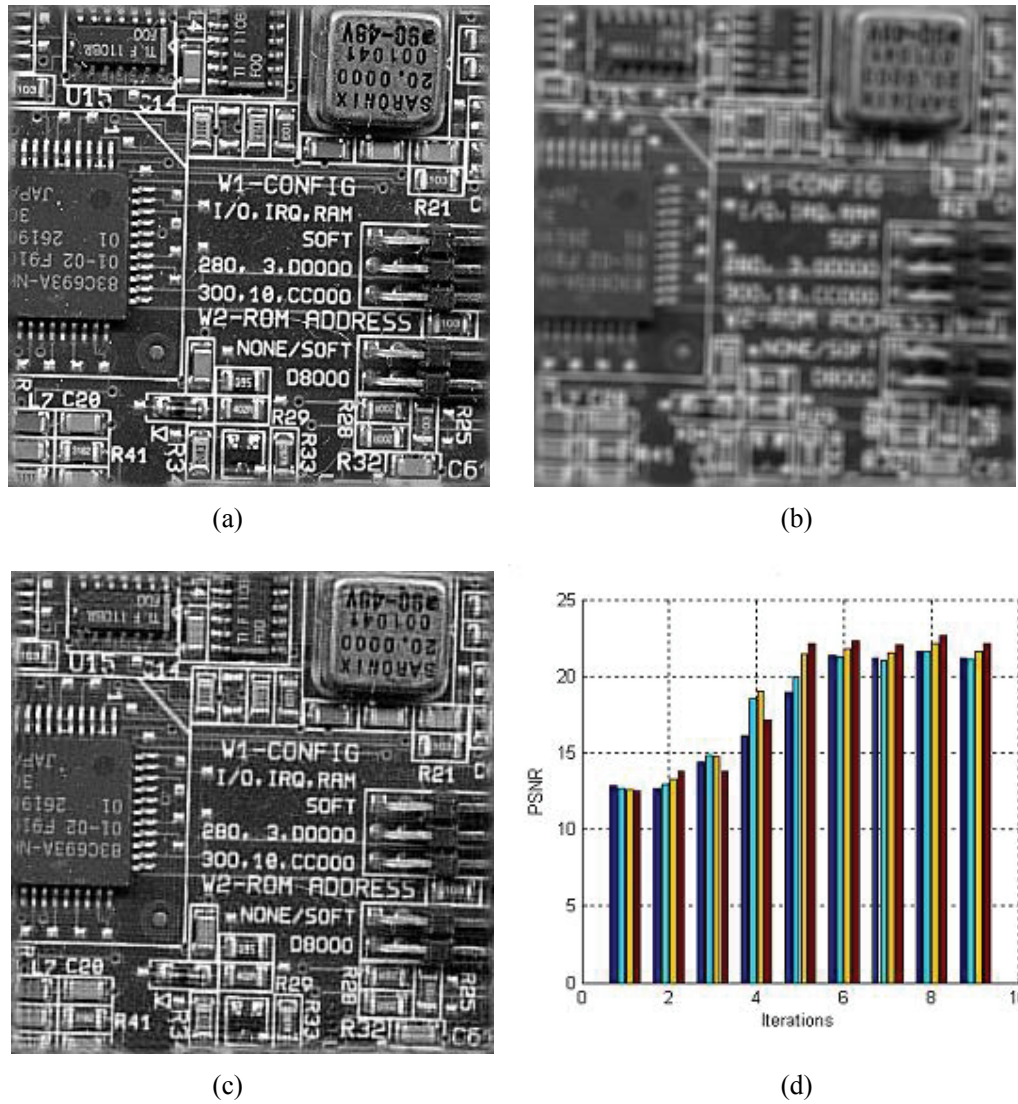


Figure 4.3 Multichannel blind image deconvolution results. (a) Original “Board” image, (b) A sampled blurred image out of the four degraded images, (c) Restored image using the proposed MRF algorithm, (d) The profile of PSNR versus the number of iterations.

4.6.2 Comparison with Other Multichannel Deconvolution Methods

To further evaluate the effectiveness of our algorithm, we compare the proposed algorithm with two iterative multichannel deconvolution methods, namely SDR-AM [62] and TV-AM [64]. Both methods decompose the multichannel blind deconvolution problem into two processes of image deconvolution and blur identification, which are optimized by alternating minimization. Their difference mainly lies in that the SDR-AM adopted symmetric double regularization to minimize the image- and blur- domain cost function, while TV and null-space of blur are incorporated into the TV-AM scheme.

The 256×256 “Satellite image” shown in Figure 4.4(a) is degraded by different blurs of $\sigma_i = \{1.7, 2.4, 3.1, 3.8\}$ under different noisy conditions (30dB and 40dB SNR noise). The proposed MRF, SDR-AM and TV-AM are applied to the blurred image, and the results are given in Figure 4.4 and Table 4.2. By comparing the restored images shown in Figure 4.4(c), (d) and (e), it is clear that our approach is superior in preserving details of the satellite. This is supported by objective performance measure as our method offers PSNR of 29.41 dB, as opposed to 28.70dB and 26.10dB by the SDR-AM and TV-AM methods, respectively. In 30dB SNR condition, our method offers PSNR of 28.58dB, which is better than 27.96 dB and 25.42dB provided by the SDR-AM and TV-AM methods. In addition, it is observed that the proposed method manages to restore image faster than the other two methods. The simulation environments of these methods are: Windows XP, MATLAB 6.5, CPU P4-2.4 GHz, and 512M RAM. It takes 64s in terms of the running time, as compared to 89s and 179s by the CGO-AM and TV-AM methods, respectively. The reason that the proposed method is faster than the CGO-AM and TV-AM methods is due to the efficient recursive updating of the images. This is in contrast to the conventional gradient-descent optimization adopted by the other methods that requires many iterations to converge in the image domain.

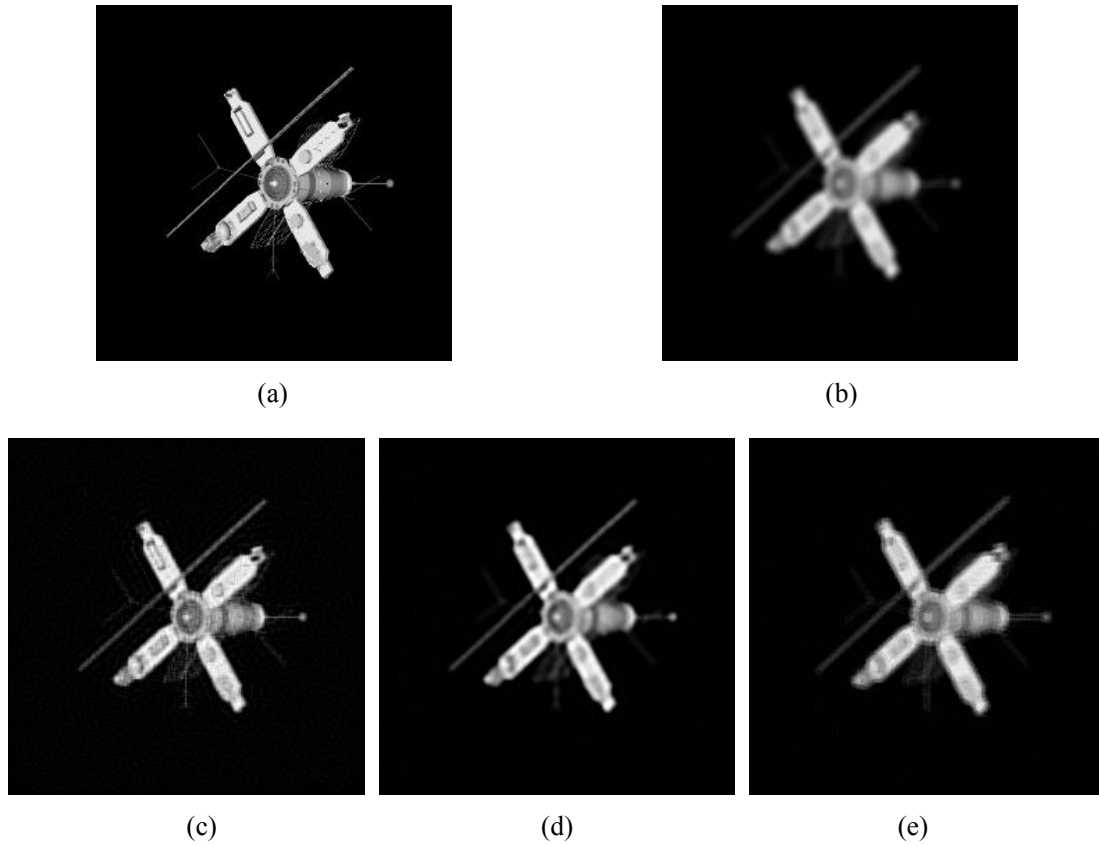


Figure 4.4 Comparison of different deconvolution results in 30dB noise environment. (a) Original “Satellite” image, (b) One of the three degraded images, (c) Restored image using the proposed MRF algorithm, (d) Restored image using the SDR-AM algorithm, (e) Restored image using the TV-AM algorithm.

TABLE 4.2 COMPARISON OF DIFFERENT DECONVOLUTION ALGORITHMS

PSF	Gaussian 7×7 , $\sigma_i = \{2.5, 3.0, 3.5\}$		Time
Noise Level	30dB	40dB	
SDR-AM	27.96dB	28.70dB	89s
TV-AM	25.42dB	26.10dB	179s
Proposed MRF	28.58dB	29.41dB	64s

4.7 Summary

This chapter proposes an iterative blind multichannel image deconvolution algorithm based on recursive filtering. The estimated image is recursively updated from its previous estimate using a regularization framework. The main novelty of this work is the development of a recursive scheme, which can reduce the computational cost through recursive updating in the Fourier transform domain. This allows the new method to be adopted readily in real-life applications. Experimental results show that it is effective in performing multichannel blind deconvolution.

4.8 Appendix A

In this Appendix, the error bound for the regularization scheme is studied. The error bound for the least squares solution to the overdetermined and underdetermined system $\mathbf{Ax} = \mathbf{b}$ is presented in [68]. To examine how the regularization solution is affected by the changes in \mathbf{A} and \mathbf{b} , the regularized solution to the underdetermined/overdetermined system $\mathbf{Ax} = \mathbf{b}$ is investigated.

Proposition: Suppose $\mathbf{A} \in \mathbb{R}^{m \times n}$, $\delta \mathbf{A} \in \mathbb{R}^{m \times n}$, $0 \neq \mathbf{b} \in \mathbb{R}^m$, $\delta \mathbf{b} \in \mathbb{R}^m$, $0 < \alpha \in \mathbb{R}$, and $\text{rank}(\mathbf{A}) = m < n$. Let $\varepsilon = \max\{\varepsilon_A, \varepsilon_b\}$, where $\varepsilon_A = \|\delta \mathbf{A}\|_2 / \|\mathbf{A}\|_2$ and $\varepsilon_b = \|\delta \mathbf{b}\|_2 / \|\mathbf{b}\|_2$.

If \mathbf{x} and $\hat{\mathbf{x}}$ are the regularization solution that satisfy

$$\begin{aligned} \mathbf{x} &= (\mathbf{A}^T \mathbf{A} + \alpha \mathbf{I})^{-1} \mathbf{A}^T \mathbf{b} = \mathbf{A}^T (\mathbf{A} \mathbf{A}^T + \alpha \mathbf{I})^{-1} \mathbf{b} \\ \hat{\mathbf{x}} &= ((\mathbf{A} + \delta \mathbf{A})^T (\mathbf{A} + \delta \mathbf{A}) + \alpha \mathbf{I})^{-1} (\mathbf{A} + \delta \mathbf{A})^T (\mathbf{b} + \delta \mathbf{b}) \end{aligned} \quad (4.19)$$

then

$$\frac{\|\hat{\mathbf{x}} - \mathbf{x}\|_2}{\|\mathbf{x}\|_2} \leq \varepsilon \left\{ \kappa_2(\mathbf{A}) + \frac{\|\mathbf{A}\|_2}{2\sqrt{\alpha}} \left(1 + \frac{\|\mathbf{b}\|_2}{\|\mathbf{A}\|_2 \|\mathbf{x}\|_2} \right) \right\} + O(\varepsilon^2) \quad (4.20)$$

Proof. Let \mathbf{B} and \mathbf{q} be defined by $\delta\mathbf{A}/\varepsilon$ and $\delta\mathbf{b}/\varepsilon$. It follows that the solution $\mathbf{x}(t)$ to

$$((\mathbf{A} + t\mathbf{B})^T (\mathbf{A} + t\mathbf{B}) + \alpha\mathbf{I})\mathbf{x}(t) = (\mathbf{A} + t\mathbf{B})^T (\mathbf{b} + t\mathbf{q}) \quad (4.21)$$

is continuously differentiable for all $t \in [0, \infty)$.

Define $\mathbf{P}_1 = \mathbf{A}^T \mathbf{A} + \alpha\mathbf{I}$ and $\mathbf{P}_2 = \mathbf{A}\mathbf{A}^T + \alpha\mathbf{I}$, we obtain:

$$\begin{aligned} \mathbf{P}_1^{-1} \mathbf{A}^T &= \mathbf{A}^T \mathbf{P}_2^{-1} \\ \|\mathbf{x}\|_2 &= \|\mathbf{A}^T \mathbf{P}_2^{-1} \mathbf{b}\|_2 \geq \sigma_m \|\mathbf{P}_2^{-1} \mathbf{b}\|_2 \\ \|\mathbf{P}_1^{-1}\|_2 &= 1/\alpha \\ \|\mathbf{P}_2^{-1}\|_2 &= 1/(\sigma_m^2 + \alpha) \\ \|\mathbf{P}_1^{-1} \mathbf{A}^T\|_2 &= \max_i (\sigma_i / (\sigma_i^2 + \alpha)) \leq 1/(2\sqrt{\alpha}) \end{aligned}$$

where σ_i is the singular value of \mathbf{A} and $\sigma_1 \geq \sigma_2 \geq \dots \geq \sigma_m > 0$.

By differentiating (4.21) with respect to t and setting $t = 0$ in the result, we obtain:

$$\dot{\mathbf{x}}(0) = \mathbf{P}_1^{-1} \mathbf{A}^T (\mathbf{q} - \mathbf{E}\mathbf{x}) + \alpha \mathbf{P}_1^{-1} \mathbf{E}^T \mathbf{P}_2^{-1} \mathbf{b} \quad (4.22)$$

Since $\mathbf{x} = \mathbf{x}(0)$, $\hat{\mathbf{x}} = \mathbf{x}(\varepsilon)$, the error upper bound is given by:

$$\begin{aligned} \frac{\|\hat{\mathbf{x}} - \mathbf{x}\|_2}{\|\mathbf{x}\|_2} &= \varepsilon \frac{\|\dot{\mathbf{x}}(0)\|_2}{\|\mathbf{x}\|_2} + O(\varepsilon^2) \\ &\leq \varepsilon \left\{ \|\mathbf{A}\|_2 \|\mathbf{P}_1^{-1} \mathbf{A}^T\|_2 \left(\frac{\|\mathbf{q}\|_2}{\|\mathbf{A}\|_2 \|\mathbf{x}\|_2} + \frac{\|\mathbf{E}\|_2}{\|\mathbf{A}\|_2} \right) + \frac{\alpha}{\sigma_m} \|\mathbf{A}\|_2 \|\mathbf{P}_1^{-1}\|_2 \frac{\|\mathbf{E}^T\|_2}{\|\mathbf{A}\|_2} \right\} + O(\varepsilon^2) \quad (4.23) \\ &\leq \varepsilon_A \kappa_2(\mathbf{A}) + \frac{\|\mathbf{A}\|_2}{2\sqrt{\alpha}} \left\{ \varepsilon_A + \varepsilon_b \frac{\|\mathbf{b}\|_2}{\|\mathbf{A}\|_2 \|\mathbf{x}\|_2} \right\} + O(\varepsilon^2) \end{aligned}$$

thereby establishing (4.20).

The extension of error bound to SIMO system in (4.6) when $\mathbf{C} = \mathbf{I}$ is straightforward by setting:

$$\mathbf{A} = \begin{bmatrix} \lambda^n \mathbf{H}_1 \\ \lambda^{n-1} \mathbf{H}_2 \\ \vdots \\ \mathbf{H}_n \end{bmatrix}, \delta \mathbf{A} = \begin{bmatrix} \lambda^n \delta \mathbf{H}_1 \\ \lambda^{n-1} \delta \mathbf{H}_2 \\ \vdots \\ \delta \mathbf{H}_n \end{bmatrix}, \mathbf{b} = \begin{bmatrix} \lambda^n \mathbf{g}_1 \\ \lambda^{n-1} \mathbf{g}_2 \\ \vdots \\ \mathbf{g}_n \end{bmatrix}, \delta \mathbf{b} = \begin{bmatrix} \lambda^n \delta \mathbf{g}_1 \\ \lambda^{n-1} \delta \mathbf{g}_2 \\ \vdots \\ \delta \mathbf{g}_n \end{bmatrix}, \mathbf{x} = \mathbf{f}, \alpha = \sum_{i=1}^n \lambda^{n-i} \alpha_i \quad (4.24)$$

In this case, the regularization operator is taken as impulse function to simplify the analysis. Suppose that the estimated \mathbf{H}_i converges to the actual PSF during the iterative MRF scheme, we will have $\delta \mathbf{H}_n \leq \dots \leq \delta \mathbf{H}_2 \leq \delta \mathbf{H}_1$. Therefore, $\delta \mathbf{A}$ in (4.24) will be reduced as the forgetting factor assigns less weight to larger error of $\delta \mathbf{H}_i$. In this sense, the upper-bound error will be reduced progressively.

4.9 Appendix B

Thorough treatment of convergence analysis on general alternating minimization (AM) is given in [46], [47]. Nevertheless, we will still provide a brief discussion on the convergence analysis of the proposed multichannel method in the following paragraphs.

In order to perform joint blur identification and image deconvolution for multichannel problem, the cost function is formulated over K channels in (4.3). An iterative strategy based on AM is adopted to project the overall cost function $J(\mathbf{f}, \mathbf{h})$ into the image-domain cost function $J(\mathbf{f} | \mathbf{h})$ and the blur-domain cost function $J(\mathbf{h} | \mathbf{f})$. A general procedure of the AM is outlined as follows:

- n th iteration:

Fix \mathbf{h} , estimate $\mathbf{f}^* = \arg \min_{\mathbf{f}} J(\mathbf{f} | \mathbf{h})$ using multichannel recursive filtering

- $(n+1)$ th iteration:

Fix \mathbf{f} , estimate $\mathbf{h}^* = \arg \min_{\mathbf{h}} J(\mathbf{h} | \mathbf{f})$ using conjugate gradient optimization.

Since $\mathbf{h} = \{\mathbf{h}_1, \dots, \mathbf{h}_K\}$, where \mathbf{h}_i is the i th-channel PSF, we have to perform

- $\mathbf{h}_1^* = \arg \min_{\mathbf{h}_1} J(\mathbf{h}_1 | \mathbf{f}, \mathbf{h}_2, \dots, \mathbf{h}_K)$
- $\mathbf{h}_2^* = \arg \min_{\mathbf{h}_2} J(\mathbf{h}_2 | \mathbf{f}, \mathbf{h}_1, \mathbf{h}_3, \dots, \mathbf{h}_K)$
- ...
- $\mathbf{h}_K^* = \arg \min_{\mathbf{h}_K} J(\mathbf{h}_K | \mathbf{f}, \mathbf{h}_1, \dots, \mathbf{h}_{K-1})$

It is worth mentioning that the order of cost function minimization can be exchanged as the proposed flowchart in Figure 4.2. We arrange the order as above for the ease of explanation.

The image- and blur-domain cost functions (i.e. $J(\mathbf{f} | \mathbf{h})$ and $J(\mathbf{h} | \mathbf{f})$) can be shown to be quadratic with respect to \mathbf{f} and \mathbf{h} respectively. Therefore, it follows that $J(\mathbf{f} | \mathbf{h})$ and $J(\mathbf{h} | \mathbf{f})$ are convex. This implies that convergence can be achieved with respect to the image- and blur-domain cost functions, respectively. Throughout the AM procedure, the sequence of cost function is given by:

$$\mathbf{a} = \{\mathbf{a}_n\} = \{a_0, a_1, a_2, \dots, a_{2k}, a_{2k+1}, \dots\} \quad (4.25)$$

where $a_0 = J(\mathbf{f}^{(0)}, \mathbf{h}^{(0)})$, $a_1 = J(\mathbf{f}^{(1)}, \mathbf{h}^{(0)})$, $a_2 = J(\mathbf{f}^{(1)}, \mathbf{h}^{(1)})$, $a_{2k} = J(\mathbf{f}^{(k)}, \mathbf{h}^{(k)})$, $a_{2k+1} = J(\mathbf{f}^{(k+1)}, \mathbf{h}^{(k)})$ will tend to decrease monotonically. $\mathbf{f}^{(k)}$ and $\mathbf{h}^{(k)} = \{\mathbf{h}_1, \dots, \mathbf{h}_K\}$ denote the estimated image and PSFs at the k th iteration.

As $a_k \geq 0$ and $a_k \geq a_{k+1}$ for $k = 1, 2, \dots$, this implies that

$$a_0 \geq a_1 \geq a_2 \geq \dots \geq a_{2k} \geq a_{2k+1} \geq \dots \quad (4.26)$$

The inequality in (4.26) holds true as $J(\mathbf{f}, \mathbf{h})$ are projected and minimized repeatedly with respect to its image and blur domains. This is equivalent to alternating minimization by part of the overall cost function. Therefore, there exists a limit, $\lim_{k \rightarrow \infty} a_k = a_\infty \geq 0$ based on the limit existence theorem. As we have shown that there exists a solution (\mathbf{h}, \mathbf{f}) corresponding to the limit a_∞ , and $J(\mathbf{f} | \mathbf{h}), J(\mathbf{h} | \mathbf{f}) \in \text{Convex}R^N$, it is apparent from the convexity property that the proposed algorithm will converge to a minima, local or global.

Chapter 5

Regularized Interpolation Using Kronecker Product

5.1 Introduction

Image interpolation, also referred to as image resizing and image enlargement, is an important component in image processing. The interpolation problem requires, in general, integer positions in the input image map to fractional (non-integer) positions in the output image. It is desirable to preserve the continuity of curvilinear features and the connectivity of objects within the image. Image interpolation is widely applied in the digital photography, computer graphics, medical imaging, among others [69].

Generally speaking, the process of decreasing the data sample is called decimation and increasing the data sample is termed interpolation. Decimation and interpolation are inverse processes. One image decimation/interpolation model is illustrated in Figure 5.1. The dotted squares denote the HR pixels, while the shaded solid squares represent LR pixels. The decimation factor d is 2 in this example.

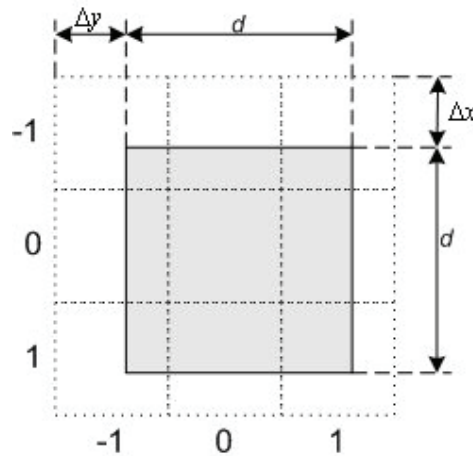


Figure 5.1 The relationship between HR and LR pixels.

From physical viewpoint of image acquisition, the response of each sensor is proportional to the integral of the light projected onto the surface of the sensor. Therefore, the intensity of the LR pixel in Figure 5.1 is determined by the weighted average of the neighbor pixels in the HR image grids.

$$\begin{aligned}
 g(0,0) = & h(-1,-1)f(-1,-1) + h(-1,0)f(-1,0) + h(-1,1)f(-1,1) \\
 & + h(0,-1)f(0,-1) + h(0,0)f(0,0) + h(0,1)f(0,1) \\
 & + h(1,-1)f(1,-1) + h(1,0)f(1,0) + h(1,1)f(1,1)
 \end{aligned} \tag{5.1}$$

where $h(x,y)$ is the weight that is proportional to the area of HR pixels $f(x,y)$ in the LR pixel $g(0,0)$. For example, $h(-1,-1) = (1-\Delta x)(1-\Delta y)$ and $h(-1,0) = (1-\Delta x)$.

To render a HR image, the missing pixel information must be estimated from the surrounding pixels of the observed LR image. This problem can be classified into two categories: (i) image interpolation when only single LR image is available, and (ii) super-resolution when multiple LR images are available.

The rest of this chapter is organized as follows. Section 5.2 reviews the methods for image interpolation. Section 5.3 provides a brief discussion on the interpolation problem. In Section 5.4, the novel algorithm using regularization theory and Kronecker product is presented.

Simulation results are given in Section 5.5. In Section 5.5.3, conclusions and further remarks are drawn.

5.2 Literature Review

Various algorithms have been proposed to address image interpolation over the years [70], [71]. Enhancing image resolution while suppressing artifacts such as blurring and jagged edges is one of the most intriguing challenges in image processing. The fast adaptive interpolation algorithms with perceptual edge enhancement are desired, especially in noisy environment where large magnification is required.

From a numerical analysis viewpoint, the classical polynomial interpolation approaches, e. g. Lagrange interpolation and Newton interpolation, use an n th polynomial to fit a large number of data points. The sequence of interpolations, however, may not converge uniformly to a continuous function. In piecewise polynomial techniques, e.g. B-spline interpolation [72], different polynomials are used in each data interval. Although piecewise polynomial interpolation eliminates the problems of excessive oscillation and non-convergence, the techniques still lead to over-smoothness in the edge and textured regions. An optimal spline-based algorithm is proposed in [73] by using the finite difference method with the idea that integral of a spline is another spline of higher degree. Some adaptive approaches adjust the algorithmic parameters according to the local features. For example, the inverse gradient [74] and warped distance [75] have been employed to determine the weights of bicubic interpolation.

Other edge-directed methods try to modify the polynomial interpolation in order to sharpen the edge perceptually. In [76], the edge information of each local image area is extracted by

using the discrete cosine transform (DCT). Different edge types are identified and used to determine different interpolation strategy for each area. The basic ideal of [77] is to estimate HR local covariance coefficients from the LR counterpart based on their geometric duality. The edge-directed interpolation is tuned based on the covariance. Other techniques, including wavelet [78], [79] and fuzzy [80] algorithms, are employed to produce visibly sharper edges than traditional techniques. These adaptive methods typically employ heuristic reasoning to estimate parameters such as threshold values or filter weights on a pixel-by-pixel basis. Therefore, they require extra computation to determine these local parameters, and the quality of the interpolated images will vary significantly with respect to changes in these parameters.

Interpolation can also be seen as an ill-posed inverse problem of decimation and be considered using statistical framework. By posing the interpolation problem as one where the image belongs to a fixed quadratic image class, the method in [81] provides a procedure for finding explicit and closed-form optimal solutions based on linear partial differential equation models. Based on optimal recovery theory, the algorithm in [82] first determines the local quadratic signal class from local image patches and then applies optimal recovery to estimate the missing samples.

In view of this, we develop a new method to estimate the HR image from the perspective of a whole image, instead of the abovementioned pixel-by-pixel basis. The relationship between the HR and LR images is developed, and the interpolation problem is formulated into optimization of a cost function. The cost function consists of a data fidelity term and a *Tikhonov* regularization functional. The solution to the optimization problem is estimated using a combined framework of Kronecker product and singular value decomposition (SVD). A key feature of the method is its computational efficiency in reconstructing high-fidelity HR image, while alleviating common artifacts encountered by other interpolation techniques. This

allows the new method to be employed readily in the areas of digital photography, computer vision, and medical imaging, among others.

5.3 Interpolation Model

The model between the HR and LR images plays a key role in the formulation of interpolation algorithms. Due to the finite sampling grid of the sensor array, the image acquisition processes can be modeled as low-pass filtering (averaging), followed by decimation [77]-[79].

Let $g(i, j)$ and $f(i, j)$ represent the observed LR image of sized $M \times N$ and the original HR image of sized $dM \times dN$, respectively, where d is the decimation factor. The relationship between the LR and HR images can be modeled as:

$$\begin{aligned} w(x, y) &= \sum_{(m,n) \in S_h} h(m, n) f(x - m, y - n) + n(x, y) \\ g(x, y) &= w(dx, dy) \end{aligned} \quad (5.2)$$

where $w(x, y)$ is the intermediary signal before decimation, $h(x, y)$ is a $S_h : P \times Q$ 2-D low-pass filter characterizing the averaging process from the HR to LR image and $n(x, y)$ is the additive noise.

It is noted that this model is similar to that of classical image restoration except for the additional decimation process. Rewrite (5.2) in the matrix-vector formation, we have:

$$\mathbf{g} = \mathbf{D}\mathbf{H}\mathbf{f} + \mathbf{n} \quad (5.3)$$

where \mathbf{f} and \mathbf{g} are the lexicographically ordered column vector of HR and LR images, respectively, \mathbf{n} is the noise vector, \mathbf{H} and \mathbf{D} are the corresponding matrices constructed from the filtering and decimation processes.

The interpolation problem can, therefore, be formulated as solving the least squares problem

for \mathbf{f} given the observation \mathbf{g} . We employ the *Tikhonov* regularization framework to address this problem, as it is able to offer numerically stable and visually pleasing solution. Under this setting, \mathbf{f}_{opt} is the solution to

$$\mathbf{f}_{opt} = \min_{\mathbf{f}} \|\mathbf{DH}\mathbf{f} - \mathbf{g}\|^2 + \alpha \|\mathbf{f}\|^2 \quad (5.4)$$

where α is the regularization parameter. The closed-form solution to the least squares problem in (5.4) using pseudoinverse is given by

$$\mathbf{f}_{opt} = [(\mathbf{DH})^T(\mathbf{DH}) + \alpha\mathbf{I}]^{-1}(\mathbf{DH})^T \mathbf{g} \quad (5.5)$$

However, this closed-form solution is impractical due to the high computational cost associated with the inversion of the large matrix $[(\mathbf{DH})^T(\mathbf{DH}) + \alpha\mathbf{I}]^{-1}$ (dimension of $d^2MN \times d^2MN$). In view of this, we propose a computationally efficient solution to address this issue.

5.4 Regularized Interpolation Using Kronecker Product

The formulation of the interpolation algorithm as a least squares problem can be found by its counterpart in classical image restoration. The image is processed as a whole-matrix computation rather than pixel-to-pixel estimation individually. The regularized least squares can achieve a well trade-off between edge preservation and noise suppression. Unlike the model of restoration, the interpolation should consider an additional decimation process. Therefore, solving for the direct closed-form solution of the regularized least squares problem is impractical due to huge computational cost involved in large matrix inversion. In view of this, the main contribution of this chapter is the development of a regularized interpolation method with reduced computational cost based on Kronecker product and SVD.

5.4.1 Kronecker Product of Matrices

In image interpolation, the relationship from HR image pixels to LR image pixels is characterized by the averaging effect, which can be mathematically modeled by a low-pass filter in (5.2). Hence the blurring matrix \mathbf{H} in the linear image acquisition model (5.3) has BCCB structure. The separability of the low-pass averaging filter enables the matrix \mathbf{H} to be decomposed into the Kronecker product of two matrices, in a similar fashion to (2.12):

$$\mathbf{H} = \mathbf{H}_u \otimes \mathbf{H}_v = \begin{bmatrix} u_0 & u_{-1} & \cdots & u_1 \\ u_1 & u_0 & \cdots & u_2 \\ \vdots & \vdots & \ddots & \vdots \\ u_{-1} & u_{-2} & \cdots & u_0 \end{bmatrix}_{dM \times dM} \otimes \begin{bmatrix} v_0 & v_{-1} & \cdots & v_1 \\ v_1 & v_0 & \cdots & v_2 \\ \vdots & \vdots & \ddots & \vdots \\ v_{-1} & v_{-2} & \cdots & v_0 \end{bmatrix}_{dN \times dN} \quad (5.6)$$

The structure of the Kronecker product for the decimation matrix \mathbf{D} in (5.3) will depend on the decimation factor d . For instance, the structure of \mathbf{D} when $d = 2$ is given as:

$$\mathbf{D} = \mathbf{D}_u \otimes \mathbf{D}_v = \begin{bmatrix} 1 & 0 & 0 & 0 & 0 \\ 0 & 0 & 1 & 0 & 0 \\ \vdots & \vdots & \vdots & \vdots & \vdots \\ 0 & 0 & 0 & 0 & 1 \end{bmatrix}_{M \times dM} \otimes \begin{bmatrix} 1 & 0 & 0 & 0 & 0 \\ 0 & 0 & 1 & 0 & 0 \\ \vdots & \vdots & \vdots & \vdots & \vdots \\ 0 & 0 & 0 & 0 & 1 \end{bmatrix}_{N \times dN} \quad (5.7)$$

Other decimation matrices with different decimation factors can be constructed in similar fashion to (5.7) by adjusting the spacing between consecutive 1s.

Using (5.6) and (5.7), the Kronecker product of \mathbf{DH} can be expressed as:

$$\mathbf{DH} = (\mathbf{D}_u \otimes \mathbf{D}_v)(\mathbf{H}_u \otimes \mathbf{H}_v) = (\mathbf{D}_u \mathbf{H}_u) \otimes (\mathbf{D}_v \mathbf{H}_v) \quad (5.8)$$

Since the dimensions of $\mathbf{D}_u \mathbf{H}_u$ and $\mathbf{D}_v \mathbf{H}_v$ are $M \times dM$ and $N \times dN$, respectively. They require the computational cost of order $O(d^3 M^3)$ and $O(d^3 N^3)$ to perform SVD:

$$\begin{aligned} \mathbf{D}_u \mathbf{H}_u &= \mathbf{U}_1 [\boldsymbol{\Sigma}_1 | \boldsymbol{\theta}] \mathbf{V}_1^T \\ \mathbf{D}_v \mathbf{H}_v &= \mathbf{U}_2 [\boldsymbol{\Sigma}_2 | \boldsymbol{\theta}] \mathbf{V}_2^T \end{aligned} \quad (5.9)$$

where \mathbf{U}_1 , \mathbf{V}_1 , and $\boldsymbol{\Sigma}_1$ are the standard matrices arising from SVD of $\mathbf{D}_u \mathbf{H}_u$, and \mathbf{U}_2 , \mathbf{V}_2 , and $\boldsymbol{\Sigma}_2$ are that of $\mathbf{D}_v \mathbf{H}_v$. It is noted that the matrix dimension is reduced from $d^2 MN \times d^2 MN$ of \mathbf{DH} to $M \times dM$ and $N \times dN$ of $\mathbf{D}_u \mathbf{H}_u$ and $\mathbf{D}_v \mathbf{H}_v$. Therefore, the computational cost associated with the matrix operations is greatly reduced.

5.4.2 Least Squares Minimization

The minimization of (5.4) can be expressed as the constrained least squares problem:

$$\mathbf{f}_{opt} = \min_f \left\| \begin{bmatrix} \mathbf{DH} \\ \sqrt{\alpha} \mathbf{I} \end{bmatrix} \mathbf{f} - \begin{bmatrix} \mathbf{g} \\ \boldsymbol{\theta} \end{bmatrix} \right\|_2^2 \quad (5.10)$$

As mentioned earlier, since the dimension of \mathbf{DH} is very large, it may not be computationally feasible to solve the problem directly using matrix pseudoinverse. In view of this, we decompose \mathbf{DH} into two smaller matrices using the Kronecker product and SVD in (5.9).

The least squares solution of (5.10) can then be reformulated into

$$\mathbf{y}_{opt} = \min_y \left\| \begin{bmatrix} ([\boldsymbol{\Sigma}_1 | \boldsymbol{\theta}] \otimes [\boldsymbol{\Sigma}_2 | \boldsymbol{\theta}]) \\ \sqrt{\alpha} \mathbf{I} \end{bmatrix} \mathbf{y} - \begin{bmatrix} \mathbf{x} \\ \boldsymbol{\theta} \end{bmatrix} \right\|_2^2 \quad (5.11)$$

where $\mathbf{y} = (\mathbf{V}_1 \otimes \mathbf{V}_2)^T \mathbf{f}$, $\mathbf{x} = (\mathbf{U}_1 \otimes \mathbf{U}_2)^T \mathbf{g}$, and \mathbf{y}_{opt} is the solution to the reformulated problem in (5.11).

Recall the property of Kronecker product for matrices \mathbf{A} , \mathbf{B} , and vector \mathbf{c} in (2.9):

$$(A \otimes B)c = \text{vec}(B \text{ivec}(c) A^T) \quad (5.12)$$

where $\text{vec}(\cdot)$ denotes concatenating the columns of a matrix into a vector, and $\text{ivec}(\cdot)$ is the inverse process of rehashing the vector into the matrix. We can solve (5.11) using the following equations to obtain the least squares solution for image interpolation

$$\begin{aligned} \mathbf{x} &= \text{vec}(U_2^T \text{ivec}(\mathbf{g}) U_1) \\ \mathbf{y}_{opt} &= \left(\begin{bmatrix} \Sigma_1 \\ \mathbf{0} \end{bmatrix} \otimes \begin{bmatrix} \Sigma_2 \\ \mathbf{0} \end{bmatrix} \right) \left(\begin{bmatrix} \Sigma_1^2 \\ \mathbf{0} \end{bmatrix} \otimes \begin{bmatrix} \Sigma_2^2 \\ \mathbf{0} \end{bmatrix} + \alpha I \right)^{-1} \mathbf{x} \\ \mathbf{f}_{opt} &= \text{vec}(V_2 \text{ivec}(\mathbf{y}_{opt}) V_1^T) \end{aligned} \quad (5.13)$$

The derivation of \mathbf{y}_{opt} in (5.13) makes use of the property

$$A^T (AA^T + \alpha I)^{-1} = (A^T A + \alpha I)^{-1} A^T \quad (5.14)$$

The main advantage of utilizing the newly derived equations in (5.13) to solve the least squares problem is the significant reduction in the computational cost achieved. For an image of sized $M \times N$ with decimation factor d , only $O(d^3 M^3 + d^3 N^3)$ operations are needed in the new scheme as compared to $O(d^6 M^6 + d^6 N^6)$ for direct implementation of pseudoinverse for (5.4). Therefore, this makes the algorithm computationally attractive and feasible to be implemented in real-life applications. The new algorithm is able to offer this computational reduction through clever manipulation of properties for SVD and Kronecker products in the context of constrained least square minimization.

5.4.3 Regularization Issue

The regularization technique is instrumental in providing satisfactory results in this work. In this Section, we will outline a simple scheme to estimate the regularization parameter α . We incorporate the generalized cross-validation (GCV) function [67] in our work as it has been

shown to be robust in general regularization schemes:

$$GCV(\alpha) = \frac{\|(\mathbf{I} - \mathbf{DHP}(\alpha))\mathbf{g}\|^2}{[\text{trace}(\mathbf{I} - \mathbf{DHP}(\alpha))]^2} \quad (5.15)$$

where $\mathbf{P}(\alpha) = ((\mathbf{DH})^T(\mathbf{DH}) + \alpha\mathbf{I})^{-1}(\mathbf{DH})^T$. An advantage of GCV is that it allows the selection of the regularization parameter even when the noise power is unknown. We modify the GCV function under the application of Kronecker product and SVD to give:

$$GCV(\alpha) = \sum_{i=1}^M \sum_{j=1}^N \left(\frac{\alpha x_{iM+j}}{\sigma_{1,i}^2 \sigma_{2,j}^2 + \lambda} \right)^2 \bigg/ \left(\sum_{i=1}^M \sum_{j=1}^N \frac{\alpha}{\sigma_{1,i}^2 \sigma_{2,j}^2 + \alpha} \right)^2 \quad (5.16)$$

where $\sigma_{1,i}$ and $\sigma_{2,j}$ are the singular values of Σ_1 and Σ_2 , respectively. x_{iM+j} is the $(iM+j)$ -th entry of the column vector \mathbf{x} in (5.13). In fact, experimental results show that our algorithm is robust towards different values of α so long as it falls within a reasonable range. The relationship between the regularization parameter and interpolation result is discussed in the Appendix.

5.5 Experimental Results

5.5.1 Comparison with Other Interpolation Methods

In this section, the proposed algorithm is run and compared with two conventional methods: Lagrange and bicubic interpolation [69]. Three natural images, “Lena” of sized 256×256 , “F16” and “Boat” of sized 512×512 , are selected as the test images in this experiment, as shown in Figure 5.2. The LR image is produced by filtering the original HR image using a uniform low-pass filter, and decimating it at a rate of $d=2$ in the horizontal and vertical directions. Further, the image is degraded under different noise levels to produce different

SNR values: noiseless (∞ dB), 40dB, and 30dB. The filter should be uniform low-pass filter, which reflects the regions of the HR grid that contribute to the formation of a single pixel in the LR grid [82]. That commonly is $\mathbf{h} = \mathbf{h}_u \mathbf{h}_v^T$, where $\mathbf{h}_u = \mathbf{h}_v = \frac{1}{d} [0.5 \ 1 \cdots 1 \ 0.5]_{d+1}^T$. The proposed algorithm is applied to perform interpolation using (5.9) and (5.13), and the regularization parameter α is chosen as 10^{-4} in this experiment.

Table 5.1 summarizes the results obtained for the test images using different methods. It can be observed that the proposed method outperforms the Lagrange and bicubic methods consistently. In average, the proposed method offers a PSNR improvement of 6.23dB over the Lagrange method, and 0.89dB over the bicubic method. Even though that the average time taken is longer for the proposed method, it is still within a reasonable range, in particular after considering the improvement that it offers over other methods. The extra computational cost is worth the benefit in some applications, where high accuracy of interpolation is the prime consideration, such as digital photography processing. Figure 5.3 shows the enlarged sections of the test images near the edge regions under 40dB noise environment. It can be observed that the proposed method produces superior image quality when compared with other methods. It also preserves the overall sharpness of the interpolated images, in particular near the edge and textured regions. The subjective human evaluation is consistent with the objective performance measure given in Table 5.1.

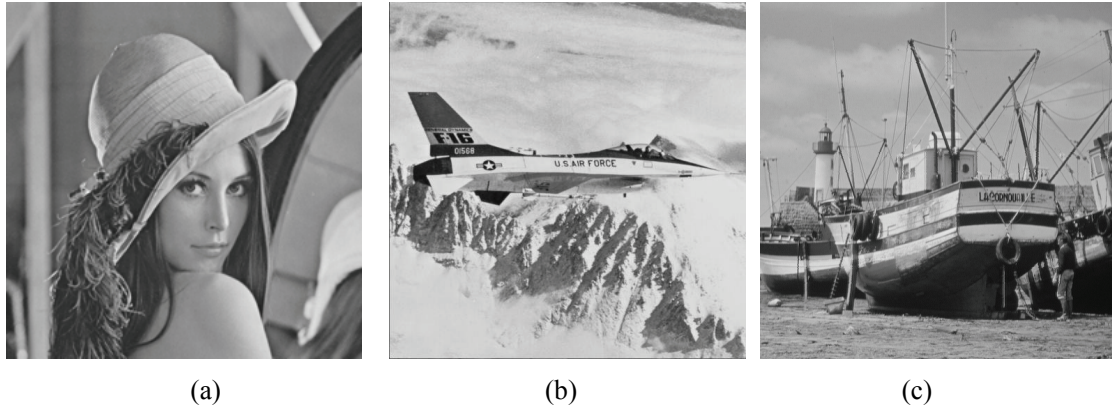


Figure 5.2 Test Images. (a) “Lena” image, (b) “F16” image, (c) “Boat” image.



Figure 5.3 Enlarged sections of interpolated images under 40dB noise. (a) Low-resolution images, (b) Lagrange method, (c) Bicubic method, (d) Proposed method.

TABLE 5.1 COMPARISON OF DIFFERENT INTERPOLATION METHODS IN PSNR

Methods	Lena (256×256)				F16(512×512)			Boat (512×512)			
	30dB	40dB	∞dB	Average Time	30dB	40dB	∞dB	30dB	40dB	∞dB	Average Time
Lagrange	24.88	24.91	24.92	0.06s	26.25	26.28	26.29	25.61	25.64	25.65	0.13s
Bicubic	30.56	30.65	30.66	0.20s	32.41	32.56	32.58	30.52	30.63	30.64	0.56s
Proposed	31.40	31.74	31.77	0.15s	33.11	33.64	33.70	31.06	31.49	31.54	0.29s

5.5.2 Effects of Regularization Parameter

In this section, the impact of the regularization parameter on the interpolation results is investigated. The “Lena” image in Figure 5.2(a) is selected as the test image. The same algorithm as in previous experiment is run but different values of regularization parameter α are used, which range from 10^{-2} to 10^{-5} . In addition, the estimated α based on the GCV function in (5.16) is also adopted. Table 5.2 summarizes the results obtained using different regularization parameters. It can be observed that method provides consistently good results for $\alpha = 10^{-3}$ to 10^{-5} , and for various noisy environments from noiseless to 30dB noise. The estimated α using GCV also offers comparable performance. The results suggest that the proposed algorithm is robust towards different noisy environments and regularization parameters so long as the value of α falls within a reasonable order of magnitude ($\alpha = 10^{-3}$ to 10^{-5}).

TABLE 5.2 COMPARISON OF DIFFERENT REGULARIZATION PARAMETERS IN PSNR

Noise	Proposed Method					
	$\alpha = 10^{-2}$	$\alpha = 10^{-3}$	$\alpha = 10^{-4}$	$\alpha = 10^{-5}$	$GCV(\alpha)$	
30dB	29.49	31.38	31.40	31.41	$\lambda = 8.3 \cdot 10^{-5}$	31.41
40dB	29.66	31.71	31.74	31.74	$\lambda = 6.6 \cdot 10^{-5}$	31.74
Noiseless	29.68	31.74	31.77	31.77	$\lambda = 6.6 \cdot 10^{-5}$	31.77

5.5.3 Computational Complexity Reduction

To reduce the computational cost, we have decided to employ the block-based processing to perform the proposed regularized interpolation. The reason for block processing is that the main computational cost of the proposed method is due to SVD, which is $O(M^3)$ for a $M \times M$ matrix. If the dimensions of matrix is reduced from the image dimension 512×512 to block dimension 16×16 , the computational load of SVD will be greatly reduced.

To reduce the dimensions of matrix, we can divide the image into blocks of sized 16×16 (or 8×8 , 32×32) with 4×4 overlapping to avoid the boundary effect. It is noted that this scheme is similar to the idea of DCT block coding. For each block, the proposed algorithm is applied to perform interpolation. The average processing times for 512×512 images (10 images) are: Lagrange: 0.13 second; Bicubic: 0.56 second; Proposed: 0.29 second. For 256×256 images (10 images): Lagrange: 0.06 second; Bicubic: 0.20 second; Proposed: 0.15 second. It can be seen that the modified proposed method is faster than the bicubic interpolation, but slightly slower than the Lagrange interpolation. It is also observed that the interpolated images have nearly the same visual quality and PSNR as in previous approach without block-processing. The simulation environments of these methods are: Windows XP, MATLAB 7.1, CPU P4-3.4 GHz, and 1G RAM.

5.6 Summary

A novel image interpolation algorithm based on a combined framework of regularization theory, constrained least squares minimization, Kronecker product and SVD is proposed. The computational cost of the scheme is greatly reduced due to careful manipulation of the properties for Kronecker product and SVD. Experimental results show that the algorithm can

provide significant performance improvement over other conventional methods.

The proposed algorithm has difficulty in modeling non-integer decimation factors when compared to conventional kernel-based approaches (polynomial or spline interpolation). Nevertheless, in applications where integer factor interpolation is used, the proposed algorithm will produce satisfactory results. The extension of this method to super-resolution is promising and we hope that this work will stimulate further investigation.

5.7 Appendix

In this appendix, the effect of the regularization parameter on the interpolation result is studied. The direct solution to the constrained least square problem in (5.4) is given as $\mathbf{f}_{opt} = \mathbf{P}(\alpha)\mathbf{g}$, where \mathbf{f}_{opt} is the estimated HR image and $\mathbf{P}(\alpha)$ is given by $\mathbf{P}(\alpha) = ((\mathbf{DH})^T(\mathbf{DH}) + \alpha\mathbf{I})^{-1}(\mathbf{DH})^T$. Substituting (5.8) and (5.9) into \mathbf{DH} and $\mathbf{P}(\alpha)$, we obtain:

$$\begin{aligned}\mathbf{DH} &= \sum_{i=1}^M \sum_{j=1}^N \sigma_{1,i} \sigma_{2,j} \mathbf{u}_{(i-1)M+j} \mathbf{v}_{(i-1)dM+j}^T \\ \mathbf{P}(\alpha) &= \sum_{i=1}^M \sum_{j=1}^N \left[\frac{\sigma_{1,i}^2 \sigma_{2,j}^2}{\sigma_{1,i}^2 \sigma_{2,j}^2 + \alpha} \right] \mathbf{v}_{(i-1)dM+j} \mathbf{u}_{(i-1)M+j}^T\end{aligned}\tag{5.17}$$

where $\Sigma_1 = \text{diag}(\sigma_{1,i})$, $\Sigma_2 = \text{diag}(\sigma_{2,j})$. $\mathbf{v}_{(i-1)dM+j}$ and $\mathbf{u}_{(i-1)M+j}$ are the $[(i-1)dM+j]$ -th and $[(i-1)M+j]$ -th column vectors of the orthogonal matrices $\mathbf{V}_1 \otimes \mathbf{V}_2$ and $\mathbf{U}_1 \otimes \mathbf{U}_2$, respectively, which can be expressed as:

$$\begin{aligned}\mathbf{v}_{(i-1)dM+j} &= \text{vec}(\tilde{\mathbf{v}}_{2,j} \tilde{\mathbf{v}}_{1,i}^T) \\ \mathbf{u}_{(i-1)M+j} &= \text{vec}(\tilde{\mathbf{u}}_{2,j} \tilde{\mathbf{u}}_{1,i}^T)\end{aligned}\tag{5.18}$$

where $\tilde{\mathbf{v}}_{1,i}$, $\tilde{\mathbf{v}}_{2,j}$, $\tilde{\mathbf{u}}_{1,i}$, $\tilde{\mathbf{u}}_{2,j}$ are the column orthonormal basis of \mathbf{V}_1 , \mathbf{V}_2 , \mathbf{U}_1 , \mathbf{U}_2 ,

respectively.

The residual error vector between the original image \mathbf{f} and the interpolation result \mathbf{f}_{opt} is equal to

$$\begin{aligned} \mathbf{r} &= \mathbf{f}_{opt} - \mathbf{f} \\ &= \left(\sum_{i=1}^M \sum_{j=1}^N \left[\frac{\sigma_{1,i}^2 \sigma_{2,j}^2}{\sigma_{1,i}^2 \sigma_{2,j}^2 + \alpha} \right] \mathbf{v}_{(i-1)dM+j} \mathbf{v}_{(i-1)dM+j}^T - \mathbf{I} \right) \mathbf{f} \\ &\quad + \sum_{i=1}^M \sum_{j=1}^N \left[\frac{\sigma_{1,i} \sigma_{2,j}}{\sigma_{1,i}^2 \sigma_{2,j}^2 + \alpha} \right] \mathbf{v}_{(i-1)dM+j} \mathbf{u}_{(i-1)M+j}^T \mathbf{n} \end{aligned} \quad (5.19)$$

If the noise is zero-mean additive white Gaussian with variance σ_n^2 , and independent of the image, then the expected error vector and square error between \mathbf{f}_{opt} and \mathbf{f} are given by:

$$E(\mathbf{r}) = \left(\sum_{i=1}^M \sum_{j=1}^N \left[\frac{\sigma_{1,i}^2 \sigma_{2,j}^2}{\sigma_{1,i}^2 \sigma_{2,j}^2 + \alpha} \right] \mathbf{v}_{(i-1)dM+j} \mathbf{v}_{(i-1)dM+j}^T - \mathbf{I} \right) E(\mathbf{f}) \quad (5.20)$$

$$\begin{aligned} E(\|\mathbf{r}\|^2) &= \sigma_n^2 \sum_{i=1}^M \sum_{j=1}^N \frac{\sigma_{1,i}^2 \sigma_{2,j}^2}{(\sigma_{1,i}^2 \sigma_{2,j}^2 + \alpha)^2} \\ &\quad + E \left[\mathbf{f}^T \left(\mathbf{I} - \sum_{i=1}^M \sum_{j=1}^N \frac{\sigma_{1,i}^4 \sigma_{2,j}^4}{(\sigma_{1,i}^2 \sigma_{2,j}^2 + \alpha)^2} \mathbf{v}_{(i-1)dM+j} \mathbf{v}_{(i-1)dM+j}^T \right) \mathbf{f} \right] \end{aligned} \quad (5.21)$$

It can be observed from (5.20) that the regularization functional has biased the interpolated image, as a trade-off for numerical stability (i.e. $E(\mathbf{r}) \neq 0$ if $\alpha \neq 0$ since

$\sum_{i=1}^M \sum_{j=1}^N \mathbf{v}_{(i-1)dM+j} \mathbf{v}_{(i-1)dM+j}^T = \mathbf{I}$). The expected square error $E(\|\mathbf{r}\|^2)$ consists of two parts: the

noise term and the image term. If the image is preprocessed using zero-mean centering, and assumed to be white, then $E(\mathbf{f}\mathbf{f}^T) = \sigma_f^2 \mathbf{I}$, where $\sigma_f^2 = E(\mathbf{f}^T \mathbf{f}) / M^2$ is the image power.

This idealized assumption is introduced to enable $E(\|\mathbf{r}\|_2^2)$ to be upper-bounded explicitly in terms of α as below:

$$E(\|\mathbf{r}\|^2) \leq \sigma_f^2 MN - \sigma_f^2 \sum_{i=1}^M \sum_{j=1}^N \frac{\sigma_{1,i}^4 \sigma_{2,j}^4}{(\sigma_{1,i}^2 \sigma_{2,j}^2 + \alpha)^2} + \sigma_n^2 \sum_{i=1}^M \sum_{j=1}^N \frac{\sigma_{1,i}^2 \sigma_{2,j}^2}{(\sigma_{1,i}^2 \sigma_{2,j}^2 + \alpha)^2} \quad (5.22)$$

It can be seen from (5.20) and (5.22) that regularization will reduce the impact of noise by effecting a small bias in the interpolated image.

Chapter 6

Bispectrum Subpixel Registration

6.1 Introduction

Image registration is the process of establishing point-to-point correspondence including translations, rotation and scaling between two images of the same scene [83], [84]. This process is needed in various imaging applications, such as stereo depth perception, motion analysis, object recognition, and image fusion, among others. It is interesting to note that image registration requires the images to be registered cover the same parts of a scene, especially when they are allowed to have rotational and scaling differences. Figure 6.1 illustrates an example of two images of the same scene, while Figure 6.1(b) is the shifted and rotated version of the reference image in Figure 6.1(a).

The rest of this chapter is organized as follows. Section 6.2 reviews the methods for image registration. In Section 6.3, the problem of subpixel image registration under noisy conditions is discussed. In Section 6.4, the proposed bispectrum-based method is explained and developed. In Section 6.5, simulation results are given and compared with other methods. In Section 6.6, conclusions are drawn.



Figure 6.1 Two images of the same scene. (a) Reference image, (b) Shifted and rotated image.

6.2 Literature Review

Image registration methods can be classified into several categories including feature-based techniques, gradient approaches, and Fourier methods. In feature-based methods, salient and distinctive objects (e.g. edges, contours, corners) are manually or automatically detected for establishing the correspondence between the observed images [85], [86]. Gradient approaches, originated from optical flow, estimate the motion parameters using a system of linear equations [87], [88]. The idea behind Fourier methods is quite simple as that the cross-correlation between the delayed signal and the reference signal will have a peak at the delayed time. According to Fourier *shift property*, the Fourier transform of a shifted function is just the transform of the unshifted function multiplied by an exponential phase factor. Hence, phase correlation method identifies the translations by taking the IDFT of the normalized cross power spectrum [89]. In addition, rotation and scaling can be reduced to similar problem like translation estimation with the aid of polar Fourier representation [90], [91]. Bypassing the need to transform data from the Cartesian to the polar domain, the rotation is estimated based on the detection of the two orthogonal zero-crossing lines that

stem from the difference of two normalized frequency magnitudes [92]. The main advantages of frequency domain algorithms are: (i) the decoupling of the estimation of the translations from the estimation of rotation and scaling, and (ii) computational convenience due to fast Fourier transform (FFT). Therefore, for estimating global motion parameters, frequency-based methods offer a very attractive alternative to traditional space domain techniques based on feature-based and gradient-based techniques.

This work focuses on high-accuracy image registration, namely subpixel translation estimation, where pixel-level translation estimation is assumed to have been performed in coarse registration step. Rotation and scaling are not within the scope of this chapter, and can be considered as being handled prior to subpixel registration. It is noted that subpixel registration is more complicated than pixel-level registration because the subpixel image intensities are commonly needed to be interpolated. High-accuracy registration is becoming increasingly important in industry such as integrated circuits inspection and optical fiber connection.

Spatial-domain subpixel registration methods interpolate the shifted image with different subpixel parameters, and compare the result with the reference image [93]. The minimum error between the image pair will provide a sound estimate of the actual motion parameters. For example, block-matching motion estimation from the noisy and downsampled frames is studied empirically in [94]. Since standard block motion estimation is accurate in theory to 1 pixel, the method interpolates the image data by a factor of p and performs motion estimation. The estimated motion from the interpolated data will correspond to $1/p$ subpixel of the original image. To reduce the computational complexity associated with the 2-D cross-correlation, the modified Marquardt-Levenberg nonlinear optimization is proposed to speed up this estimation in [94]. The feature-based methods, such as edge matching, find the

congruence that minimizes the error between the features and their targets [96]. The projection-based approach firstly transforms the image into two vector projections by accumulating pixel values along the rows and columns, respectively [97]. The vector projections are in turn used to estimate the individual horizontal and vertical components of the translation by means of a 1-D cross-correlation-based estimator. The underlying shortcoming of correlation-based methods is local convergence due to the interpolation procedure under noisy conditions. Gradient correlation methods use the gradient information to find the extrema of cross-correlation function. The method in [98] attempts to estimate the subpixel motion in the frequency-domain. The multiresolution bidirectional gradient is employed in [99] to improve the performance of the conventional gradient methods. The gradient techniques have degraded performance under noisy conditions due to the fact that the gradient operation amplifies the noise.

The phase correlation approaches utilize the idea of the cross-correlation in the frequency-domain. They identify the translations by taking the inverse discrete Fourier transform (IDFT) of the normalized cross power spectrum. For 3-D medical imaging application, a higher-order singular value decomposition technique is used to decompose the phase correlation between two N -dimensional (N -D) images to independently identify translational displacements with subpixel accuracy [101]. Pixel-level Fourier techniques have been extended to address subpixel registration using two different approaches. The first approach is by estimating the best-fit phase plane in the frequency domain, of which the slope of the plane is used to determine the subpixel translation [100]. The aliasing error due to inadequate sampling is masked out by spectrum cancellation [101]. The second approach is to evaluate the dominant peaks of the IDFT of the normalized cross power spectrum, and proceed to estimate the subpixel translations [102].

Generally speaking, the aforementioned methods perform reasonably well when the noise is AWGN and the noise level is moderate. The precondition, however, is impractical in some applications such as sonar imaging where the SNR is low and the additive noise is correlated between the observed images. Under these circumstances, the performance of these techniques will degrade significantly [104], [105].

In view of this, we propose a new bispectrum technique to address the problem of subpixel image registration. The proposed method is motivated by the observation that the n -th joint cumulants of the Gaussian random process are equal to zero for $n > 2$ [106]. Therefore, the phase information between the image pair can be estimated reliably from the higher-order statistics such as bispectrum, as they are robust towards correlated Gaussian noise and low SNR environments.

6.3 Problem Formulation

6.3.1 Subpixel Translation Estimation

Let s be the original image, and $f_i \{i = 1, 2\}$ be two images that are shifted versions of s :

$$f_i(x, y) = s(x + \delta_{x,i}, y + \delta_{y,i}), \quad i = 1, 2 \quad (6.1)$$

where $(\delta_x, \delta_y) = (\delta_{x,2} - \delta_{x,1}, \delta_{y,2} - \delta_{y,1})$ is the relative translations between the image pair, which is restricted to subpixel level $[0, 1)$ in this work. In the absence of noise and aliasing, the *shift property* of Fourier transform gives:

$$\tilde{f}_1(\omega_x, \omega_y) = \tilde{f}_2(\omega_x, \omega_y) e^{-j(\omega_x \delta_x + \omega_y \delta_y)} \quad (6.2)$$

where $\tilde{f}_i = \mathcal{F}[f_i]$ is the Fourier transform of $f_i \{i = 1, 2\}$. Therefore, the normalized cross

power spectrum is given by:

$$\tilde{P}(\omega_x, \omega_y) = \frac{\tilde{f}_1(\omega_x, \omega_y) \tilde{f}_2(\omega_x, \omega_y)^*}{|\tilde{f}_1(\omega_x, \omega_y) \tilde{f}_2(\omega_x, \omega_y)^*|} = e^{-j(\omega_x \delta_x + \omega_y \delta_y)} \quad (6.3)$$

The phase information of $\omega_x \delta_x + \omega_y \delta_y$ plays a critical role in the estimation of subpixel translations. For instance, the best-fit plane method estimates the subpixel translations as the slopes of the phase plane [100].

6.3.2 Noise Effect

In most imaging applications, noise exists in the captured images up to a certain level. The noise is commonly due to factors such as photoelectric noise, film grain noise, and quantization noise, among others. Moreover, the imaging sensor array, usually the charged-coupled device (CCD), is subject to various sources of noise, including thermal noise and shot noise. The noisy effect is particularly evident under low lighting when the camera gain is high.

In the presence of additive noise, the images $f_i \{i = 1, 2\}$ in (6.1) are modeled as

$$f_i(x, y) = s(x + \delta_{x,i}, y + \delta_{y,i}) + n_i(x, y), \quad i = 1, 2 \quad (6.4)$$

where n_i is the additive noise that arises during the image formation process. Conventional Fourier method ignores the noise in their formulation, and hence will experience performance deterioration in noisy environments. Assuming n_i is independent of s , the normalized cross power spectrum of (6.3) can be expressed as:

$$\begin{aligned}
\tilde{P}(\omega_x, \omega_y) &= \frac{\mathcal{F}[R_{f_2 f_1}(\tau_x, \tau_y)]}{\mathcal{F}[R_{f_1 f_1}(\tau_x, \tau_y)]} \\
&= \frac{\mathcal{F}[R_{ss}(\tau_x - \delta_x, \tau_y - \delta_y)] + \mathcal{F}[R_{n_1 n_2}(\tau_x, \tau_y)]}{\mathcal{F}[R_{ss}(\tau_x, \tau_y)] + \mathcal{F}[R_{n_1 n_1}(\tau_x, \tau_y)]} \\
&= \frac{e^{-j(\omega_x \delta_x + \omega_y \delta_y)} + \tilde{R}_{n_1 n_2}(\omega_x, \omega_y) / \tilde{R}_{ss}(\omega_x, \omega_y)}{1 + \tilde{R}_{n_1 n_1}(\omega_x, \omega_y) / \tilde{R}_{ss}(\omega_x, \omega_y)}
\end{aligned} \tag{6.5}$$

where $R_{f_2 f_1}(\tau_x, \tau_y) \triangleq E[f_2(x, y)f_1(x + \tau_x, y + \tau_y)]$ is the correlation function between f_2 and f_1 . It is observed that $\tilde{P}(\omega_x, \omega_y)$ can be approximated as $e^{-j(\omega_x \delta_x + \omega_y \delta_y)}$ only when $\tilde{R}_{n_1 n_1}(\omega_x, \omega_y)$ and $\tilde{R}_{n_1 n_2}(\omega_x, \omega_y)$ are negligible compared to $\tilde{R}_{ss}(\omega_x, \omega_y)$. This requires the SNR to be high ($\tilde{R}_{n_1 n_1}(\omega_x, \omega_y) \approx 0$) and the two noise processes to be uncorrelated ($\tilde{R}_{n_1 n_2}(\omega_x, \omega_y) \approx 0$). These preconditions, however, are restrictive in some applications, such as sonar imaging where the noise level is high and their sources are correlated. In view of this, we develop a bispectrum algorithm to address this difficulty. Of course, we assume that the techniques of pixel-level registration can still work to provide accurate translation estimation under such noisy conditions.

6.4 Subpixel Registration under Noisy Conditions

6.4.1 Proposed Cross Bispectrum Method

Higher-order spectra defined in terms of higher-order cumulant contains additional information that is not conveyed by the signal's correlation or power spectrum. It is useful in suppressing additive Gaussian noise (white and color noise) because all joint cumulants of order > 2 are equal to zero for Gaussian random processes [106]. Hence, in circumstances where the observed signal consists of non-Gaussian signal of interest and is corrupted by

additive Gaussian noise, there are clear advantages in estimating the desired signal through higher-order spectra.

In this work, we assume that the original image s in (6.4) follows non-Gaussian distribution with nonzero skewness (i.e. $E[s^3] \neq 0$, which indicates the existence of non-trivial bispectrum). This assumption is in agreement with most observations that images are indeed non-Gaussian distributed. We further assume that \mathbf{n}_1 and \mathbf{n}_2 are zero-mean Gaussian, signal independent random noise, which are potentially cross-correlated. It is noted that these assumptions are valid in many general applications [105]-[107]. We remove the mean from the images to perform zero-mean centering, and restrict the translations (δ_x, δ_y) to be within the interval $[0, 1)$ for subpixel registration.

The third-order auto- and cross-cumulants of the observed images f_1 and f_2 are defined as:

$$\begin{aligned} R_{f_1 f_1 f_1}(\tau_x, \tau_y, v_x, v_y) &\triangleq E[f_1(x, y) f_1(x + \tau_x, y + \tau_y) f_1(x + v_x, y + v_y)] \\ &= R_{sss}(\tau_x, \tau_y, v_x, v_y); \\ R_{f_2 f_1 f_2}(\tau_x, \tau_y, v_1, v_2) &\triangleq E[f_2(x, y) f_1(x + \tau_x, y + \tau_y) f_2(x + v_x, y + v_y)] \\ &= R_{sss}(\tau_x - \delta_x, \tau_y - \delta_y, v_x, v_y) \end{aligned} \quad (6.6)$$

where $R_{sss}(\tau_x, \tau_y, v_x, v_y) \triangleq E[s(x, y) s(x + \tau_x, y + \tau_y) s(x + v_x, y + v_y)]$ is the third-order auto-cumulant of the desired signal s .

It is worth mentioning that (6.6) holds because \mathbf{n}_1 and \mathbf{n}_2 are zero-mean Gaussian noise, hence all their joint cumulants of order > 2 are equal to zero. Thus we can estimate the desired signal s from (6.6) without the interference of Gaussian noise.

The bispectrums are computed by taking the DFT of the cumulants:

$$\begin{aligned}\tilde{R}_{f_1 f_1 f_1}(\omega_x, \omega_y, \nu_x, \nu_y) &\triangleq \mathcal{F}[R_{f_1 f_1 f_1}(\tau_x, \tau_y, \nu_x, \nu_y)] = F_{sss}(\omega_x, \omega_y, \nu_x, \nu_y); \\ \tilde{R}_{f_2 f_1 f_2}(\omega_x, \omega_y, \nu_x, \nu_y) &\triangleq \mathcal{F}[R_{f_2 f_1 f_2}(\tau_x, \tau_y, \nu_x, \nu_y)] = F_{sss}(\omega_x, \omega_y, \nu_x, \nu_y) e^{-j(\omega_x \delta_x + \omega_y \delta_y)}\end{aligned}\quad (6.7)$$

where $\tilde{R}_{sss}(\omega_x, \omega_y, \nu_x, \nu_y) \triangleq \mathcal{F}[R_{sss}(\tau_x, \tau_y, \nu_x, \nu_y)]$ is the auto-bispectrum of \mathbf{s} .

Therefore, the phase information of $\omega_x \delta_x + \omega_y \delta_y$ is given by the normalized cross bispectrum:

$$\begin{aligned}\tilde{P}(\omega_x, \omega_y, \nu_x, \nu_y) &= \frac{\tilde{R}_{f_2 f_1 f_2}(\omega_x, \omega_y, \nu_x, \nu_y) \tilde{R}_{f_1 f_1 f_1}(\omega_x, \omega_y, \nu_x, \nu_y)^*}{|\tilde{R}_{f_2 f_1 f_2}(\omega_x, \omega_y, \nu_x, \nu_y) \tilde{R}_{f_1 f_1 f_1}(\omega_x, \omega_y, \nu_x, \nu_y)^*|} \\ &= e^{-j(\omega_x \delta_x + \omega_y \delta_y)}\end{aligned}\quad (6.8)$$

Compared to the cross power spectrum in (6.5), the normalized cross bispectrum in (6.8) provides more robust phase information in noisy environments. This is because that the normalized cross bispectrum is independent of the noise distortion terms $\tilde{R}_{n_1 n_1}(\omega_x, \omega_y)$ and $\tilde{R}_{n_1 n_2}(\omega_x, \omega_y)$. This enables reliable subpixel registration when incorporating the *Dirichlet* estimation scheme in [102] to give:

$$\begin{aligned}P(x, y) &= \mathcal{F}^{-1}[\tilde{P}(\omega_x, \omega_y, \nu_x, \nu_y)] \\ &= \mathcal{F}^{-1}[e^{-j(\omega_x \delta_x + \omega_y \delta_y)}] \\ &= \frac{1}{MN} \frac{\sin(\pi(x - \delta_x))}{\sin(\pi(x - \delta_x)/M)} \frac{\sin(\pi(y - \delta_y))}{\sin(\pi(y - \delta_y)/N)}\end{aligned}\quad (6.9)$$

where $M \times N$ is the length of IDFT. The *Dirichlet* function in (6.9) is approximated by *sinc* function as

$$P(x, y) \approx \text{sinc}(x - \delta_x) \text{sinc}(y - \delta_y) \quad (6.10)$$

where the denominator is approximated by $\lim_{t \rightarrow 0} \sin t \approx t$, i.e.

$$\begin{aligned}\lim_{M \rightarrow \infty} \sin\left(\frac{\pi(x - \delta_x)}{M}\right) &= \frac{\pi(x - \delta_x)}{M}; \\ \lim_{N \rightarrow \infty} \sin\left(\frac{\pi(y - \delta_y)}{N}\right) &= \frac{\pi(y - \delta_y)}{N}\end{aligned}\quad (6.11)$$

Expressing $\sin t$ using *Taylor* series expansion, we have:

$$\sin t = \sum_{k=1}^{\infty} (-1)^{k-1} \frac{t^{2k-1}}{(2k-1)!} \quad (6.12)$$

It is obvious that the smaller the value of t , the less the error of approximation for $\lim_{t \rightarrow 0} \sin t \approx t$. Further, the function of $P(x, y) \approx \text{sinc}(x - \delta_x) \text{sinc}(y - \delta_y) / MN$ has dominant values centered near $(x, y) = (\delta_x, \delta_y)$ where $0 \leq \delta_x, \delta_y \leq 1$. Therefore, a simple yet effective method of estimating (δ_x, δ_y) can be achieved by solving the nonlinear equations (6.10) at coordinates of (0,0), (0,1), (1,0) and (1,1), which correspond to the main peaks. The intermediate steps are given as:

$$\begin{aligned}\frac{P(0,0)}{P(1,0)} &= \frac{P(0,1)}{P(1,1)} = \frac{\sin(\pi(1 - \delta_x)/M)}{\sin(\pi\delta_x/M)} \approx \frac{1 - \delta_x}{\delta_x}; \\ \frac{P(0,0)}{P(0,1)} &= \frac{P(1,0)}{P(1,1)} = \frac{\sin(\pi(1 - \delta_y)/N)}{\sin(\pi\delta_y/N)} \approx \frac{1 - \delta_y}{\delta_y}\end{aligned}\quad (6.13)$$

The final estimated motion shift or translations $(\hat{\delta}_x, \hat{\delta}_y)$ can then be deduced directly by using

$$\begin{aligned}\hat{\delta}_x &= \frac{1}{2} \left(\frac{P(1,0)}{P(1,0) + P(0,0)} + \frac{P(1,1)}{P(1,1) + P(0,1)} \right); \\ \hat{\delta}_y &= \frac{1}{2} \left(\frac{P(0,1)}{P(0,1) + P(0,0)} + \frac{P(1,1)}{P(1,1) + P(1,0)} \right)\end{aligned}\quad (6.14)$$

It is worth mentioning that if a more accurate estimate for $(\hat{\delta}_x, \hat{\delta}_y)$ is required, we can approximate $\sin t \approx t - t^3/6$, and solve for $(\hat{\delta}_x, \hat{\delta}_y)$ accordingly. A brief analysis on the

higher-order estimate is provided in the Appendix.

6.4.2 Complexity Reduction

Conventional techniques for computation of power spectrum include (i) the direct method, which involves calculation of the power of the Fourier transform, and (ii) indirect method, which computes the Fourier transform of the correlation function of the data (i.e. periodogram). In a similar fashion to periodogram, the cumulants in (6.6) can be calculated by dividing the image into C segments, and obtaining the average cumulant as below (ergodicity is implicitly assumed) [106]:

$$R_{f_1 f_1 f_1}(\tau_x, \tau_y, \nu_x, \nu_y) = \frac{1}{C} \sum_{i=1}^C \hat{R}_{f_1 f_1 f_1}(\tau_x, \tau_y, \nu_x, \nu_y) \quad (6.15)$$

where $\hat{R}_{f_1 f_1 f_1}(\tau_x, \tau_y, \nu_x, \nu_y)$ is the cumulant of each segment. The main advantage of this procedure is to reduce the computational cost of cumulant estimation.

Moreover, it is observed that the $\tilde{P}(\omega_x, \omega_y, \nu_x, \nu_y)$ in (6.8) is independent of the frequency parameters (ν_x, ν_y) . Therefore, we do not have to compute the entire 4-dimensional bispectrum. Instead, we may simply choose several low frequency slices, for example $(\nu_x = 0, 1, 2; \nu_y = 0, 1, 2)$, in the computation of $\tilde{P}(\omega_x, \omega_y, \nu_x, \nu_y)$. The simulation environments of the experiments are as follows: Windows XP, MATLAB 7.1, CPU P4-3.4 GHz, and 1G RAM. The average computational time for the images in Figure 6.3 is 14.13 second, compared to 124.30 second before the block processing technique. Therefore, the computational load is greatly reduced.

The schematic diagram of the proposed algorithm is given in the following flowchart:

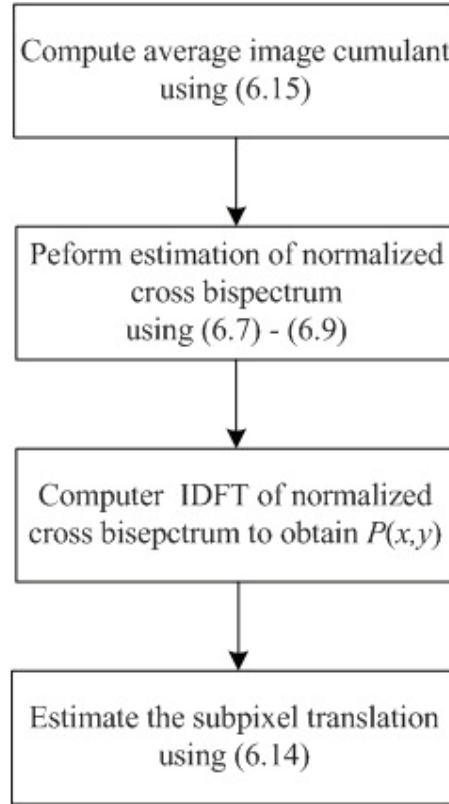


Figure 6.2 Schematic diagram of the proposed algorithm.

6.5 Experimental Results

The effectiveness of the proposed method is demonstrated using different images under noisy conditions. In addition, we compare the proposed algorithm with well-known phase correlation method by *Foroosh et. al.* [102]. In order to verify the algorithm experimentally, the image pair $f_i \{i = 1, 2\}$ are generated in line with the procedures given in [93], [102]. The images in Figure 6.3 are translated by different shift sizes (at pixel level) for three different images. After that, each shifted image is filtered and downsampled at a rate that is larger than the maximum shift so that the relative translations between image pair are maintained at a subpixel level. Different levels of noises are then added to the shifted, downsampled images

to simulate the noisy image pair.



Figure 6.3 Test Images. (a) “Pentagon” image, (b) “Castle” image, (c) “NTU” image.

6.5.1 Image Degraded By AWGN

The 1024×1024 “Pentagon” image shown in Figure 6.3(a) is shifted by different pixel values (a, b) , and downsampled by a factor of 4×4 to generate an image pair with subpixel translations of $(a/4, b/4)$. Further, the images are degraded under different noise levels to produce different SNR environments: 40dB, 30dB, 20dB, and 10dB. In this experiment, we perform the registration procedures given in Section 6.4 for two sets of subpixel translations $(0.25, 0.75)$ and $(0.75, 0.25)$. Table 6.1 summarizes the results obtained using the *Foroosh* method and the proposed algorithm. It can be observed that the proposed method provides satisfactory performance for subpixel translation estimation under different noisy conditions. Further, it is clear that the proposed method consistently outperforms the *Foroosh* methods, especially under low SNR or noisy environments. The results show that the method is more effective in suppressing Gaussian noise, hence giving rise to superior subpixel image registration.

It is worth noting that bispectrum method requires a higher computational cost compared to

the normal spectrum approach. In the above experiment, the running time by the proposed method is nearly 100s, which is longer than 10s of spectrum-based method. However, in selected applications where high-accuracy registration is the prime consideration, the extra computational cost can be considered as well justified.

TABLE 6.1 RESULTS OF SUBPIXEL REGISTRATION IN AWGN

SNR	(0.25, 0.75)		(0.75, 0.25)	
	Foroosh	Proposed	Foroosh	Proposed
10dB	(0.38, 0.65)	(0.29, 0.68)	(0.64, 0.36)	(0.68, 0.30)
20dB	(0.31, 0.71)	(0.28, 0.74)	(0.71, 0.31)	(0.74, 0.29)
30dB	(0.30, 0.73)	(0.27, 0.74)	(0.74, 0.30)	(0.74, 0.28)
40dB	(0.29, 0.74)	(0.27, 0.74)	(0.74, 0.29)	(0.75, 0.28)

6.5.2 Image Degraded by Cross-Correlated Noise

The 1704×1704 “Castle” image shown in Figure 6.3(b) is shifted and downsampled by a factor 8×8 to produce the image pair. In this experiment, however, the noise is correlated across two channels, e.g. \mathbf{n}_1 is assumed to be AWGN, while \mathbf{n}_2 is generated from \mathbf{n}_1 using:

$$n_2(x, y) = \sum_{i=-3}^3 \sum_{j=-3}^3 h(i, j) n_1(x+i, y+j) \quad (6.16)$$

where $h(i, j) = \exp(-(i^2 + j^2)/2)$ is a low-pass filter used to ensure that the noise \mathbf{n}_1 and \mathbf{n}_2 are correlated [106]. In this study, we use two sets of subpixel translations (0.125, 0.125) and (0.375, 0.75), and consider different noise power ranging from 10dB- 40 dB SNR environments. We repeat the procedures as before to estimate the subpixel translations. The results obtained are shown in Table 6.2. It is observed that proposed method again provides satisfactory performance in all cases. Again, it is noticed that the bispectrum method provides

superior performance when compared to the conventional phase correlation method. These results clearly demonstrate the effectiveness of the proposed method in dealing with cross-correlated channel noise.

TABLE 6.2 RESULTS OF SUBPIXEL REGISTRATION IN CORRELATED NOISE

SNR	(0.125, 0.125)		(0.375, 0.75)	
	Foroosh	Proposed	Foroosh	Proposed
10dB	(0.267, 0.255)	(0.151, 0.170)	(0.378, 0.571)	(0.330, 0.609)
20dB	(0.205, 0.199)	(0.135, 0.132)	(0.403, 0.677)	(0.347, 0.736)
30dB	(0.152, 0.150)	(0.132, 0.129)	(0.406, 0.722)	(0.380, 0.770)
40dB	(0.139, 0.137)	(0.128, 0.127)	(0.410, 0.731)	(0.377, 0.774)

6.5.3 Image Registration for Pixel and Subpixel Translations

In this experiment, image registration is implemented for the situations that images are not only translated by subpixel but also shifted by pixels. A real-life image of sized 480×640 pixels is captured using a digital camera (Cannon IXUS v3). The image in Figure 6.3(c) shows the graduate hall of Nanyang Technological University. The HR image is shifted by different pixels that are larger than the maximum decimation rate. Thus the overall translations between the registered images consist of both pixel and subpixel translations. Further, these images are degraded by AWGN at different levels. The two-stage coarse-to-fine algorithm for estimation of the translational displacement is run. The coarse step uses the classical phase correlation to identify the pixel level shift, while the fine step uses the proposed bispectrum method for subpixel registration. The results obtained are shown in Table 6.3. In coarse registration, conventional techniques can determine the pixel-level translations for low SNR images. However, in fine registration step, conventional subpixel registration methods cannot provide satisfactory results. It is shown that the proposed method

again provides satisfactory results under noisy conditions.

TABLE 6.3 RESULTS OF PIXEL AND SUBPIXEL REGISTRATION

SNR	(2.25, 1.50)		(3.66, 4.33)	
	Foroosh	Proposed	Foroosh	Proposed
10dB	(2.40, 1.64)	(2.30, 1.59)	(3.86, 4.67)	(3.76, 4.47)
20dB	(2.34, 1.61)	(2.29, 1.56)	(3.77, 4.48)	(3.78, 4.38)
30dB	(2.33, 1.61)	(2.27, 1.55)	(3.68, 4.44)	(3.68, 4.32)
40dB	(2.26, 1.54)	(2.26, 1.52)	(3.68, 4.34)	(3.64, 4.32)

6.6 Summary

This chapter proposes a new bispectrum technique to address subpixel image registration. Its main features include the capability to perform reliable image registration under low SNR environments as well as cross-correlated channel noise. This is because that the method utilizes higher-order spectra of the observed images to suppress Gaussian noise. Experimental results show that the proposed method is effective in identifying subpixel translations under different noise levels and environments. It also outperforms the conventional second-order phase correlation technique in image registration.

Time average and ensemble average will not be exactly the same in practical situations. The high order cumulants of the noise term are not exactly zero with limited number of realizations. In the experiments, the assumption of ergodicity is adopted and the difference between time average and ensemble average is minimized by proper selection of the window size.

6.7 Appendix

In the event that a higher precision for the shift estimate δ_x is desired, we can employ 3rd-order Taylor expansion $\sin t = t - t^3/6 + O(t^5)$ in our estimation. Therefore, the estimation of δ_x is given by

$$k = \frac{P(0,0)}{P(1,0)} = \frac{P(0,1)}{P(1,1)} = \frac{\sin(\rho(1-\delta_x))}{\sin(\rho\delta_x)} \approx \frac{(1-\delta_x) - \frac{1}{6}\rho^2(1-\delta_x)^3}{\delta_x - \frac{1}{6}\rho^2\delta_x^3} \quad (6.17)$$

where $\rho = \pi/M$. In order to compute δ_x , we simply need to solve the implicit equation below:

$$\rho^2(1+k)\delta_x^3 - 3\rho^2\delta_x^2 + (3\rho^2 - 6k - 6)\delta_x + 6 - \rho^2 = 0 \quad (6.18)$$

Chapter 7

Blind Multiframe Super-Resolution

7.1 Introduction

Super-resolution (SR) is the process of combining multiple LR images to form a higher resolution one. The technology of SR has been an active research area in image processing over the last two decades [108]-[111]. This cutting-edge technology has already yielded several commercial software products, including the Salient Stills' "VideoFOCUS" [112], QE lab's "QE SuperResolution"[113], Cognitech's "Video Investigator" [114]. The technology of SR enables the user to easily process sequential video frames in order to produce high-quality still images with more detail, greater dynamic range, less noise, fewer artifacts and higher resolution.

The basic model for SR is illustrated in Figure 7.1, where the upper HR image is reconstructed from three lower LR images. LR images represent the downsampled and aliased view of the same scene. And there exists relative global motion between LR images, including rotation and translations. It is noted that if the LR images are shifted by integer pixels, then each image contains the same information excluding the boundary, and thus there is no new information that can be used to reconstruct the image. Therefore, only the subpixel displacements make it possible to reconstruct a HR image.

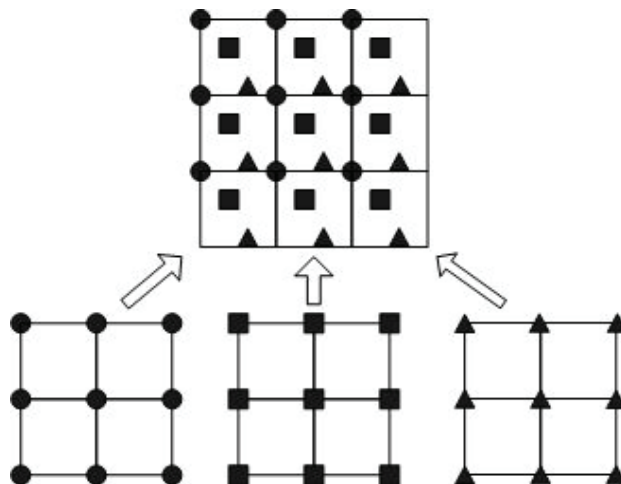


Figure 7.1 Basic model for super-resolution.

The rest of this chapter is organized as follows. Section 7.2 reviews the methods for SR. Section 7.3 provides a brief discussion on the spatial-domain SR problem. In Section 7.4, the development of blind multiframe SR reconstruction algorithm is presented. Simulation results are given in Section 7.5. In Section 0, conclusions are drawn.

7.2 Literature Review

The earliest work carried out by Tsai and Huang in [115] is in the frequency domain that centered on the shifting and aliasing properties of the continuous and discrete Fourier transform. It formulates a set of linear equations to estimate the Fourier coefficients of the HR image using least-squares criterion. An extension of this idea using recursive least squares is proposed in [116]. Further, to address the issue of the ill-posed nature of the inverse problem, regularization is employed in the recursive reconstruction procedure [117]. The frequency-based methods are simple and computationally efficient. Nevertheless, they are sensitive towards imprecision arising from subpixel image registration, and do not take the potential blurring effect into consideration.

There have been some successful works on the development of SR in the spatial domain,

which exploit and extend the progresses made in the field of image restoration. These techniques develop a cost function using a framework of constrained least squares minimization, such as iterative back-projection (IBP) [118], [119] and projection-onto-convex-sets (POCS) [120], [121]. The IBP method provides an initial estimate to the HR image, and simulates the image formation process to obtain a set of LR images. An error function between the actual and simulated LR images is then minimized iteratively in order to estimate the HR image progressively. The POCS method, on the other hand, limits the feasible solution space of SR into an intersection of constraint sets. These include criteria corresponding to data fidelity, finite energy, and bounded support. In enhanced POCS, the discretization of the continuous image formation model is improved to explicitly allow for higher order interpolation methods to be used. And the constraint sets are modified to reduce the amount of edge ringing presented in the estimated HR image [122]. Another extension that incorporates the regularization theory for edge preservation and noise suppression has also been proposed in [123].

The probabilistic techniques employ the Bayes' framework to seek the maximum *a posteriori* (MAP) estimate [124], [125]. The Bayesian framework with consideration of the hybrid motion-compensation and transform-based coding is extended to SR [126], [127]. It is appealing for the compressed video with moderate bit rates. The probabilistic reconstruction techniques need more computations than POCS method. Neural network has also been applied to solve SR reconstruction problem [128]. Training-based algorithm is proposed for the particular image-based rendering application that the object texture is known [129]. Nevertheless, it is hard to reconstruct the complex, real-world objects freely.

Other SR schemes, which model the relationship between the HR and LR images using geometric warping, blurring and decimation process with additive noise, have also shown

promising results. These methods function by first finding the blurred HR image from the LR measurements, followed by image deconvolution to deblur the image [130], [131]. The data fusion for HR image reconstruction based on Delaunay triangulation with smoothness constraints has also been proposed in [132]. The main drawback of the aforementioned restoration-based methods is that the identification of the PSFs in the context of SR reconstruction has not been addressed adequately. In other words, they assume that the PSFs are known *a priori*, which is not practical in many real-world applications. Therefore, it is necessary to incorporate blur identification into the SR image reconstruction. Currently, there are relatively few works on blind SR image reconstruction, namely, simultaneous reconstruction of the HR image and identification of the unknown blurs from the observed LR images. A recent technique for blind SR has been reported in [133], which is based on generalized cross-validation and Gauss quadrature theory. The method, nevertheless, works only for parametric blur, thereby restricting its flexibility.

In view of this, we propose a novel algorithm for SR under the blind condition, i.e. the blurs are unknown and will be identified jointly with the HR image reconstruction. It is noted that the algorithm can be considered as a joint interpolation-restoration strategy. The main contribution of this chapter is the development of multichannel blind restoration to estimate the unknown PSFs, and its integration into the SR scheme to render HR images. A joint blur identification and HR image reconstruction strategy is proposed using AM. It involves recursive updating of the estimated HR image from the previous estimate. The blurs are identified iteratively using CGO. A key feature of the method is that the quality of the estimated blurs and consequently the HR image improves progressively throughout the process. Therefore, this allows the user to monitor and terminate the SR reconstruction flexibly once the quality of the HR image becomes satisfactory to the user.

7.3 Spatial-Domain Super-Resolution

Consider the general SR model that consists of K measured LR images, that are related to the desired HR image through a series of mappings comprising geometric warping (i.e. translations, rotation), blurring, decimation, together with potential additive noise. The i th LR image can be modeled as [108]-[111]:

$$\mathbf{g}_i = \mathbf{D}_i \mathbf{H}_i \mathbf{S}_i \mathbf{f} + \mathbf{n}_i, \quad i = 1, 2, \dots, K \quad (7.1)$$

where \mathbf{f} , \mathbf{g}_i and \mathbf{n}_i represent the lexicographically ordered column vectors of the HR image, the i th LR image, and the i th channel noise, respectively. \mathbf{S}_i and \mathbf{H}_i stand for the i th channel geometric warping and blurring operators, which are matrices constructed from the warping vector \mathbf{s}_i and PSF \mathbf{h}_i , respectively. \mathbf{D}_i denotes the decimation operator. In this work, we focus on space-invariant blur and translational geometric warps. Therefore, \mathbf{S}_i and \mathbf{H}_i can be represented by BCCB matrices. In addition, the decimation operators are assumed to be the same across all channels (i.e. $\forall i, \mathbf{D}_i = \mathbf{D}$). This is a reasonable assumption as it is fairly common that a single imaging device is used to capture multiple observations, hence the resolution and subsequently the decimation factors are similar across different channels.

To tackle the ill-posed nature of SR, the following regularized cost function are commonly employed:

$$J(\mathbf{f}) = \sum_{i=1}^K (\|\mathbf{g}_i - \mathbf{D} \mathbf{H}_i \mathbf{S}_i \mathbf{f}\|^2) + R(\mathbf{f}) \quad (7.2)$$

The first term in (7.2) represents the data fidelity criterion, while the second term $R(\mathbf{f})$ is the regularization functional. The least-square fidelity and the regularization terms function

together to provide a numerically stable solution that bears close visual fidelity to the original HR image. In other words, the minimum of the cost function in (7.2) will provide a numerically stable yet visually pleasing estimate to the desired HR image. It is worth noting that the formation of the cost function in (7.2) is similar to that in the image deconvolution problem. However, most existing image restoration algorithms cannot be applied readily to address the SR problem due to extra complexities arising from geometric warping, decimation process, and multiple observations of LR images.

Generally, the SR schemes consist of three stages: image registration, interpolation, and restoration. These steps can be implemented separately or simultaneously, depending on the conditions of the problem, thereby yielding algorithms with different levels of complexities and sophistications. A general overview of conventional SR algorithms can be described as follows:

(1) Image registration

This is used to identify the geometric warps between the HR and LR images.

(2) Image interpolation (data fusion)

This is used to estimate the blurred HR image from the observed LR images. Assume that the blur operators across all channels are the same (i.e. $\forall i, \mathbf{H}_i = \mathbf{H}$). Let the blurred version of the desired HR image be $\mathbf{y} = \mathbf{H}\mathbf{f}$. Since \mathbf{S}_i and \mathbf{H} are block-circulant matrices, they satisfy the commutivity property $\mathbf{S}_i\mathbf{H} = \mathbf{H}\mathbf{S}_i$. Therefore, (7.2) can be rewritten as

$$J(\mathbf{y}) = \sum_{i=1}^K (\|\mathbf{g}_i - \mathbf{D}\mathbf{S}_i\mathbf{y}\|^2) + R(\mathbf{y}) \quad (7.3)$$

The blurred version of the HR image (i.e. \mathbf{y}) can be obtained by minimizing the cost function.

(3) Image restoration

This is used to estimate the HR image \mathbf{f} from its blurred version \mathbf{y} using image deconvolution techniques.

$$J(\mathbf{f}) = \|\mathbf{y} - \mathbf{H}\mathbf{f}\|^2 + R(\mathbf{f}) \quad (7.4)$$

Conventional SR algorithms outlined above require the assumption that $\forall i, \mathbf{H}_i = \mathbf{H}$. This precondition, however, is elusive in many applications such as remote sensing and microscopy imaging, where the blurring conditions for different channels may differ. Further, the SR algorithms assume that the blur is known prior to SR image reconstruction. This assumption, unfortunately, is impractical in many real-world applications, hence restricting the flexibility of classical SR algorithms. In view of this, we propose a novel algorithm for SR image reconstruction under the blind condition, i.e. the blurs are unknown and will be identified jointly with the HR image reconstruction.

7.4 Blind Multiframe Super-Resolution Scheme

7.4.1 Joint Interpolation-Restoration Framework

In this work, we focus on an important aspect of SR, namely the interpolation-restoration step. The warping vectors of $\mathbf{s}_i (i = 1, 2, \dots, K)$ are assumed to have been successfully estimated in the registration step using methods found in [83]-[102]. We propose a novel SR scheme for performing joint interpolation-restoration as follows:

- (1) Image registration
- (2) Single-channel image interpolation

The LR images are first interpolated to obtain the blurred, shifted versions of the required HR image as:

$$\mathbf{y}_i = \text{interp}(\mathbf{g}_i) \quad (7.5)$$

where $\text{interp}(\cdot)$ denotes the conventional interpolation operation, such as the Bicubic or edge-directed algorithms [70]-[77].

(3) Multichannel image restoration

In contrast to SISO restoration in (7.4), we propose the following new cost function to perform joint multichannel blind deconvolution:

$$J(\mathbf{f}, \mathbf{h}_1, \dots, \mathbf{h}_K) = \sum_{i=1}^K \|\mathbf{y}_i - \mathbf{S}_i \mathbf{H}_i \mathbf{f}\|^2 + R(\mathbf{f}) + R(\mathbf{h}_1, \dots, \mathbf{h}_K) + S(\mathbf{h}_1, \dots, \mathbf{h}_K) \quad (7.6)$$

where $R(\mathbf{f})$ is the image-domain regularization functional. $R(\mathbf{h}_1, \dots, \mathbf{h}_K)$ and $S(\mathbf{h}_1, \dots, \mathbf{h}_K)$ are blur-domain regularization functional and soft learning term. The objective of using $S(\mathbf{h}_1, \dots, \mathbf{h}_K)$ is to introduce reinforcement learning based on inter-channel blurring model. Further details will be explained in Subsection 7.4.2.

The main feature of the proposed model in (7.6) is that it is a SIMO process. As opposed to SISO SR algorithms in [130], [131], the SIMO technique can produce better results as the inadequate information in one channel can be compensated by the other channels. Moreover, the blurring conditions need not be exactly the same for all the LR images (channels), hence alleviating one of the constraints encountered by conventional SISO schemes. We will outline the development of the joint multichannel blind deconvolution and HR image reconstruction algorithm in the following paragraphs.

Let $(\delta_{x,i}, \delta_{y,i})$ be the relative translations along the X - and Y -axis between the i th LR image and the reference LR image, which is restricted to a subpixel value of $[0, 1)$. In the case of pixel-level translations, we can simply shift the image by the corresponding integer pixels to

make the above assumption valid. It is noted that if the LR images are shifted by integer units only, each image will contain essentially the same information, and thus no useful information can be derived for SR.

Considering the HR image with the decimation factor of d , the warping vector is then given by $\mathbf{s}_i = (d\delta_{x,i}, d\delta_{y,i})$. The warped HR images are denoted by:

$$\mathbf{z}_i = \mathbf{f} \langle \mathbf{s}_i \rangle \quad (7.7)$$

where \mathbf{z}_i and \mathbf{f} are the warped and reference HR images, respectively. $\langle \rangle$ denotes the warping process as defined by $z_i(x, y) = f(x + d\delta_{x,i}, y + d\delta_{y,i})$. The imaging process, which characterizes the blurring and warping operations, but without the decimation is given by:

$$\begin{aligned} y_i(x, y) &= \iint h_i(p, q) z_i(x - p, y - q) dp dq \\ &= \iint h_i(p + d\delta_{x,i}, q + d\delta_{y,i}) f(x - p, y - q) dp dq \\ &= \iint q_i(p, q) f(x - p, y - q) dp dq \end{aligned} \quad (7.8)$$

Let us define $\mathbf{q}_i = \mathbf{h}_i \langle \mathbf{s}_i \rangle$ as the warped blur, it can be observed that the process of blurring a warped image is equivalent to blurring the reference image using a warped blur. Therefore, the cost function in (7.6) can be re-expressed in terms of \mathbf{q}_i as:

$$J(\mathbf{f}, \mathbf{q}_1, \dots, \mathbf{q}_K) = \sum_{i=1}^K \|\mathbf{y}_i - \mathbf{q}_i * \mathbf{f}\|^2 + R(\mathbf{f}) + R(\mathbf{q}_1, \dots, \mathbf{q}_K) + S(\mathbf{q}_1, \dots, \mathbf{q}_K) \quad (7.9)$$

It is noted that the minimization of (7.9) does not require the information of the warped vector if we consider \mathbf{q}_i as the effective blur instead of \mathbf{h}_i . Therefore, the step of subpixel image registration can be circumvented, theoretically, if the minimization of (7.9) lead to a convergent solution. However, as SR tends to be ill-posed, we will still extract and integrate the subpixel translation information into the learning term $S(\mathbf{q}_1, \dots, \mathbf{q}_K)$ to provide a stable

solution. As a result, our scheme is more robust as it is less sensitive towards the impact of inaccurate subpixel registration.

The cost function in (7.9) consists of multivariate arguments of \mathbf{f} and $\mathbf{q}_i \{i=1, \dots, K\}$. As it is computationally intensive to perform simultaneous optimization of all arguments, AM is adopted again as previous chapters to perform projection-based optimization. AM projects the overall cost function $J(\mathbf{f}, \mathbf{q}_1, \dots, \mathbf{q}_K)$ into the image-domain cost function $J(\mathbf{f} | \mathbf{q}_1, \dots, \mathbf{q}_K)$ and the blur-domain cost function $J(\mathbf{q}_1, \dots, \mathbf{q}_K | \mathbf{f})$, and minimize them iteratively until convergence or a maximum number of iteration is reached. The proposed iterative SR strategy can be summarized as below:

- (1) Perform image registration to estimate $\mathbf{s}_i (i=1, 2, \dots, K)$.
- (2) Perform image interpolation as (7.5) to obtain $\mathbf{y}_i (i=1, 2, \dots, K)$.
- (3) Perform joint blind multiframe restoration by optimizing (7.9) using AM:
 - (i) Initialize $\mathbf{f} = \mathbf{0}$, $\mathbf{q}_i \{i=1, \dots, K\}$ as impulse function.
 - (ii) For the k th iteration:

For the n th LR image ($n=1, \dots, K$):

- (a) Minimize the n th blur-domain cost function, namely, perform n th channel blur identification using conjugate gradient optimization, to be explained in greater details in Section 7.4.2.

$$\begin{aligned}
 \mathbf{q}_n &= \arg \min_{\mathbf{q}_n} J(\mathbf{q}_1, \dots, \mathbf{q}_K | \mathbf{f}) \\
 &= \arg \min_{\mathbf{q}_n} \left(\sum_{i=1}^K \| \mathbf{y}_i - \mathbf{q}_i * \mathbf{f} \|^2 + R(\mathbf{q}_1, \dots, \mathbf{q}_K) + S(\mathbf{q}_1, \dots, \mathbf{q}_K) \right)
 \end{aligned} \tag{7.10}$$

- (b) Minimize the n th image-domain cost function, namely, perform the HR image

estimation using recursive multichannel restoration, to be explained in greater details in Section 7.4.3.

$$\begin{aligned} \mathbf{f} &= \arg \min_{\mathbf{f}} J(\mathbf{f} | \mathbf{q}_1, \dots, \mathbf{q}_K) \\ &= \arg \min_{\mathbf{f}} \left(\sum_{i=1}^K \|\mathbf{g}_i - \mathbf{q}_i * \mathbf{f}\|^2 + R(\mathbf{f}) \right) \end{aligned} \quad (7.11)$$

(iii) Repeat step (ii) until convergence or a maximum number of iterations is reached.

7.4.2 Channel Blur Identification

PSF is the transfer function that is used to characterize the blurring process. Image blurring is commonly due to causes by inner optical system (e.g. lens defocusing, optical system aberration) and outer environmental factors (e.g. relative motion between camera and objects, atmospheric turbulence). Taking these factors into consideration, the blurs across different channels in SR will share certain similar characteristics, e.g. they commonly belong to the same parametric model. In other words, the blur of each LR frame (channel) is similar to each other up to a certain extent. These scenarios are relatively common in many applications such as video recording which experience same lens focusing artifact, or image capturing with similar settings. This notion is used to determine the weighted mean blur estimate \mathbf{h}_i^* from all the channel blurs \mathbf{h}_j as:

$$\mathbf{h}_i^* = \frac{\sum_{j=1, j \neq i}^K w_j \mathbf{h}_j}{\sum_{j=1, j \neq i}^K w_j} \quad (7.12)$$

where w_j is the weight of the j th channel blur.

The inter-frame similarity model for the warped blur \mathbf{q}_i^* can be computed as

$$\mathbf{q}_i^* = \mathbf{h}_i^* \langle \mathbf{s}_i \rangle = \frac{\sum_{j=1, j \neq i}^K w_j \mathbf{q}_j \langle \mathbf{s}_j - \mathbf{s}_i \rangle}{\sum_{j=1, j \neq i}^K w_j} \quad (7.13)$$

This inter-frame blur model will be incorporated into the HR reconstruction procedure to improve the convergence performance. We propose a new blur-domain cost function of (7.10) to integrate this modeling term:

$$J(\mathbf{q}_1, \dots, \mathbf{q}_K | \mathbf{f}) = \sum_{i=1}^K \left(\|\mathbf{g}_i - \mathbf{q}_i * \mathbf{f}\|^2 + \beta_i \|\mathbf{e}_i * \mathbf{q}_i\|^2 + \gamma_i \|\mathbf{q}_i - \mathbf{q}_i^*\|^2 \right) \quad (7.14)$$

where β_i are the regularization parameters that offer a compromise between least-square fidelity error and the regularity of the solution. \mathbf{e}_i are the regularization operators, which usually take the form of high-pass filter. The third term serves as a reinforcement learning term to integrate the potentially useful parametric structure of the blur, where γ_i are the learning parameters.

The main objective of this arrangement is to assess the relevance of the current blur \mathbf{q}_i with respect to the inter-frame blur model, and integrates this knowledge progressively into the scheme whenever appropriate. If the current blur \mathbf{q}_i resembles \mathbf{q}_i^* closely, suggesting a strong likelihood that \mathbf{q}_i indeed belongs to a desired common structure, then the modeling term $\|\mathbf{q}_i - \mathbf{q}_i^*\|^2$ will induce learning towards \mathbf{q}_i^* . In contrast, if \mathbf{q}_i differs from \mathbf{q}_i^* significantly, then $\|\mathbf{q}_i - \mathbf{q}_i^*\|^2$ will be small, and there will be little learning towards \mathbf{q}_i^* . This mechanism represents a flexible reinforcement learning paradigm. It is noted that this idea is inspired by the successful PDR approach, which introduce a soft modeling term into the SDR

scheme in Chapter 3. The optimal solution of \mathbf{q}_i can be obtained using CGO outlined in Subsection 3.5.1.

7.4.3 Recursive Multichannel Image Restoration

The overall cost function in (7.9) consists of two sets of unknown variables: image and blur. As explained earlier, we project $J(\mathbf{f}, \mathbf{q}_1, \dots, \mathbf{q}_K)$ into the image-domain cost function $J(\mathbf{f} | \mathbf{q}_1, \dots, \mathbf{q}_K)$ by fixing the blurs to give:

$$J(\mathbf{f} | \mathbf{q}_1, \dots, \mathbf{q}_K) = \sum_{i=1}^K (\|\mathbf{g}_i - \mathbf{q}_i * \mathbf{f}\|^2 + \alpha_i \|\mathbf{c} * \mathbf{f}\|^2) \quad (7.15)$$

where \mathbf{c} and α_i are the regularization operator and parameter, respectively. We employ recursive filtering to minimize the cost function as detailed in Subsection 4.4.1.

7.5 Experimental Results

7.5.1 Super-Resolution of Simulated Images

The effectiveness of the proposed algorithm is illustrated through using different images under various conditions. The original HR image is translated by different shift sizes at pixel-level. After that, each shifted image is blurred and downsampled such that the translations between the LR and the reference frames is maintained at a subpixel level. In addition, we compare the proposed algorithm with the well-known bicubic interpolation [134] and the benchmarked IBP method [119].

The ‘‘Satellite’’ image is selected as the test image in Figure 7.2(a). The HR image is shifted by translations of (0,0), (0,1), (1,0), (1,1), and blurred by four different 5×5 Gaussian blurs

$\sigma_i = \{2.0, 2.2, 2.4, 2.6\}$, respectively. The decimation factor d is taken as 2 and the images are degraded by additive noise to produce SNR at 40dB, as show in Figure 7.2(b). For the purpose of subjective comparison later, one of the four LR frames in Figure 7.2(b) is upsampled and shown in Figure 7.2(c). The proposed algorithm is run to perform blind SR image reconstruction. The forgetting factor is taken as $\lambda = 0.5$. The regularization parameters are $\alpha_i = 0.00025$, $\beta_i = \gamma_i = 10^6$, while the regularization operators \mathbf{c} and \mathbf{e}_i are simply taken as the impulse functions. The weight for computing \mathbf{q}_i^* is set to $w_i = 1$. The maximum iteration number is set to 5. The reconstructed HR image using the proposed algorithm is shown in Figure 7.2(d). It can be observed that the reconstructed image in Figure 7.2(d) has recovered most visual information of the original HR image in Figure 7.2(a) from four LR images. By comparing the reconstructed HR images shown in Figure 7.2(d)-(f), it is clear that the proposed method is superior in rendering high-quality images while preserving various details of the image. The satisfactory subjective inspection of the image is supported by objective performance measure as our method offers a PSNR of 28.83 dB, as opposed to 26.27dB and 26.50dB offered by the bicubic and IBP methods, respectively.

The second experiment is based on a real aerial image of “Singapore” in Figure 7.3(a). The observed LR frames are obtained as the same as the previous experiment where the subpixel translations are (0,0), (0.25,0.25), (0.5, 0.5), (0.75,0.75). The proposed method is implemented with the following parameters: $\lambda = 0.7$, $\alpha = 0.005$, $\beta_i = \gamma_i = 10^6$, \mathbf{c} and \mathbf{e}_i are taken as Laplacian high-pass filter. The enlarged section of the LR image and the reconstructed HR images are shown in Figure 7.3(b)-(f). The PSNR of the reconstructed HR images using the proposed method, bicubic interpolation, and the IBP methods are 24.37dB, 22.12dB, and 22.52dB, respectively. It is clear from both visual inspection of the figures as well as the objective PSNR indicator that our method provides a superior reconstructed HR

image when compared with that obtained using the other two methods.

7.5.2 Super-Resolution of Real-Life Images

This experiment is to demonstrate SR when considering static scenes, where snapshots of a static object are taken in a quick succession. A set of four real-life color images of sized 640×480 pixels are captured using a digital camera (Cannon IXUS v3), as shown in Figure 7.4(a). In the captured LR images, there are some texts that are region of interest (ROI) required enhancing, as shown in Figure 7.4(b). We use the two-stage coarse-to-fine algorithm for identification of the global translational displacement. The coarse step uses the classical phase correlation to identify the pixel-level shift, while the fine step uses the bispectrum method in Chapter 6 to estimate the subpixel-level translations. We observe that there does not exist any pixel-level translations among the captured images in the coarse step. Taken the first LR frame as the reference image, the subpixel translations are given in Table 7.1.

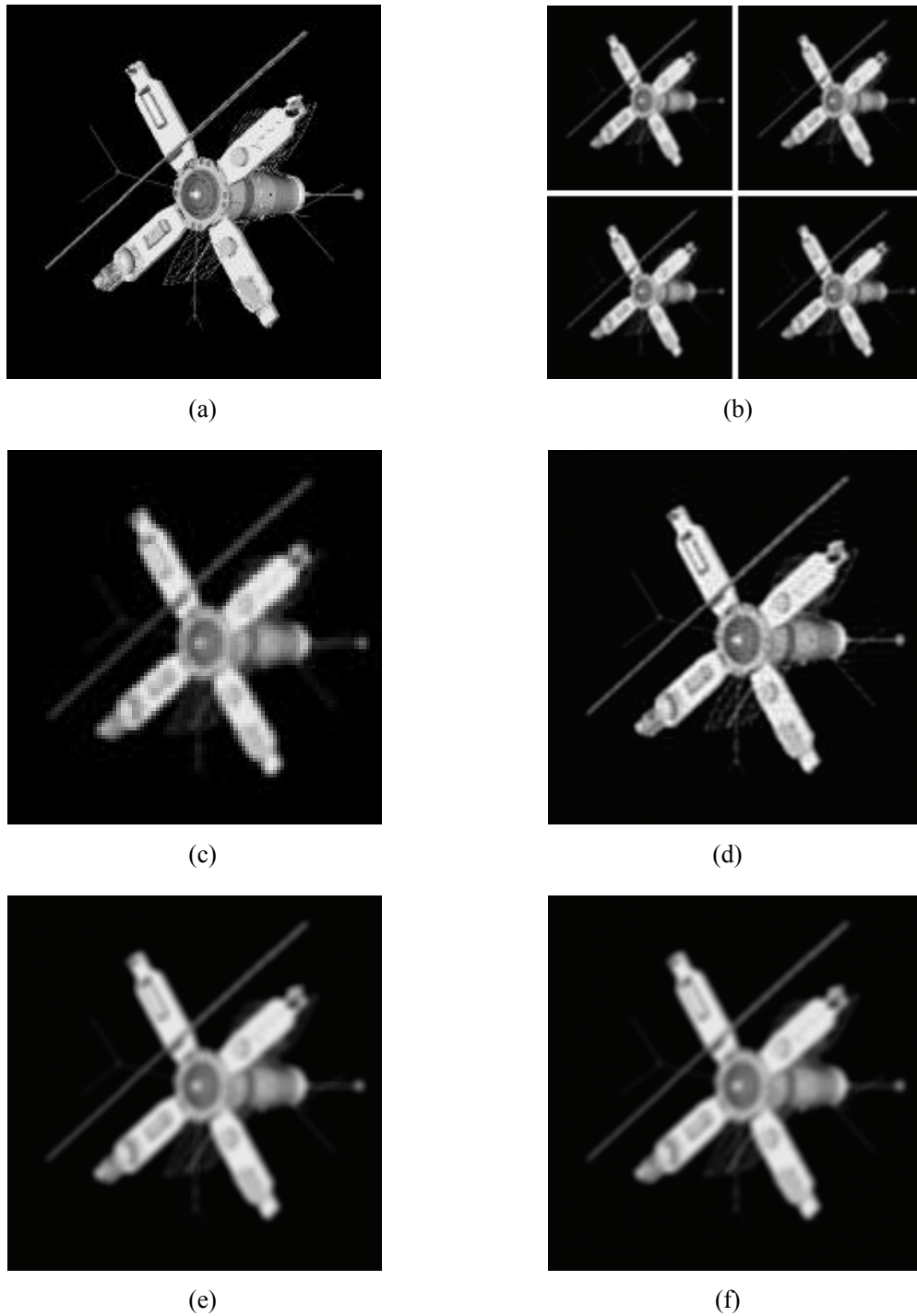


Figure 7.2 Blind super-resolution image reconstruction results. (a) Original “Satellite” image, (b) Four LR images, (c) One of the upsampled LR frames, (d) Proposed algorithm, (e) Bicubic interpolation, (f) IBP method.

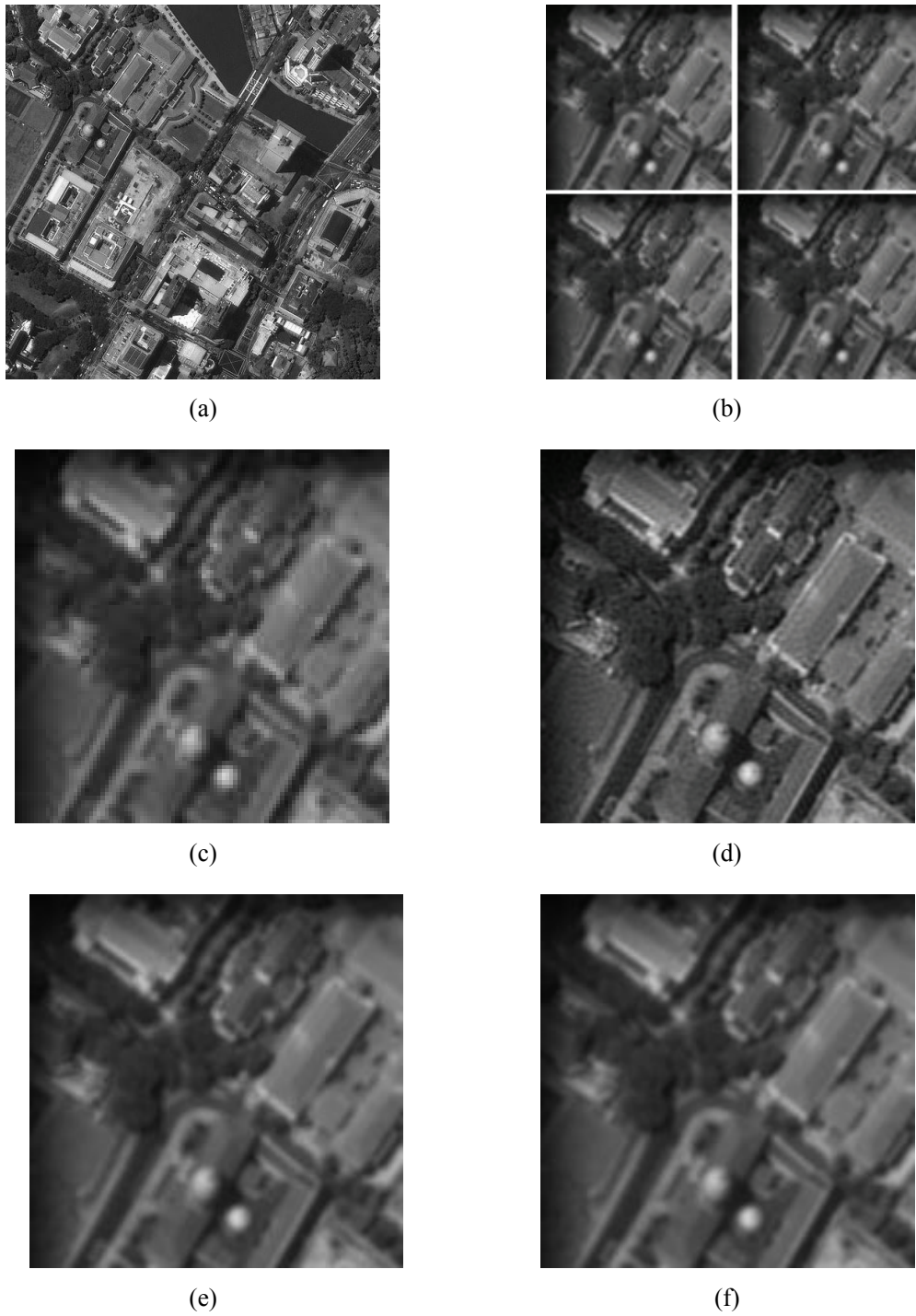


Figure 7.3 Blind super-resolution image reconstruction results. (a) Original “Singapore” image, (b) Section of LR frames, (c) One of the upsampled LR frames, (d) Proposed algorithm, (e) Bicubic interpolation, (f) IBP method.



Figure 7.4 Blind super-resolution image reconstruction results. (a) One of LR frame, (b) Section of LR frame, (c) Upsampled section, (d) Reconstruction result.

TABLE 7.1 RESULTS OF SUBPIXEL REGISTRATION

LR images	Red channel	Green channel	Blue channel
1	(0,0)	(0,0)	(0,0)
2	(0.200, -0.136)	(0.183, -0.101)	(0.200, -0.096)
3	(0.289, 0.107)	(0.246, 0.135)	(0.309, 0.168)
4	(0.449, -0.353)	(0.441, -0.363)	(0.461, -0.278)

Using the captured four LR images, a HR image is constructed through the proposed SR algorithm. After comparing Figure 7.4(c) and (d), we observe that the resolution and quality of the image has been increased, especially for some blurred words. This illustrates that the proposed method is helpful in handling real-life HR image reconstruction.

7.6 Summary

In the proposed SR method, the blurs do not need to be known *a priori* as they can be identified iteratively using the proposed AM scheme. If the PSFs are known *a priori*, the proposed method still will yield better performance as the number of unknown parameters is reduced. We formulate the SR problem as a framework of joint interpolation-restoration scheme. The main contribution of this chapter is the development of multichannel blind restoration to estimate the unknown PSFs, and its integration into the SR scheme to render HR images. A joint blur identification and HR image reconstruction is proposed using AM. It involves recursive updating of the estimated HR image from the previous estimate. The blurs are identified iteratively with the utilization of inter-frame blur similarity. Experimental results show that the method is effective in performing blind SR image reconstruction.

Chapter 8

Conclusion and Recommendations

8.1 Conclusion

Enabling machines to observe, interpret, and interact with the world has long been a goal of computer vision and machine vision. A computer can monitor the world through various sensors, such as still and video cameras, or through more advanced sensors, such as radar, sonar, infra-red cameras, and medical imaging devices. A critical need that has not been adequately addressed so far is the ability to reconstruct object of interest at sufficient resolution with more fine details observable. This cutting-edge technology consists of probabilities and stochastic processes, statistical signal processing, optimization theory, and computational intelligence.

This thesis has investigated the problem of combining information contained in a single or multiple views of a scene into a HR still image. There are three main parts to this investigation: image deconvolution, interpolation, and super-resolution.

8.1.1 Image Deconvolution

We have proposed a new PDR approach to blind image restoration based on soft integration of manifold blur parametric modeling. As opposed to other blind algorithms, the proposed technique is flexible, as it does not require assumptions such as (i) known blur supports, and

(ii) stringent stochastic image modeling.

The efficient discrete spatial techniques for blur support identification are developed and implemented in Chapter 2. The method is formulated with consideration of the image and PSF characteristics. The efficiency and validity are demonstrated based on ARMA image modeling. The criterion involves the design of an adaptive filter, which is derived from the degraded image. The method provides robust estimation of the support size for 1-D blurs as well as 2-D blurs. The simplicity of our criterion is a main advantage in algorithmic formulation. Experimental results show that the technique is effective in identifying blur size under different circumstances, namely different images, blur types, and noise levels.

A MSPM algorithm has been proposed to generate the manifold parametric blur models and determine the final blur estimate in Chapter 3. The PDR scheme integrates the parametric information of the blur structures progressively throughout restoration. The blind restoration problem is formulated into an AM procedure of blur identification and image restoration. This improves the convergence greatly, leading to significant reduction in computational cost. Experimental results show that the PDR method is robust in blind restoration of images degraded under different blur structures and noise levels.

An iterative algorithm based on multichannel recursive filtering is proposed to address multichannel deconvolution in Chapter 4. The estimated image is recursively updated from its previous estimates using a regularization framework. The multichannel blurs are identified iteratively using CGO. A key feature of the method is its computational simplicity and efficiency. This allows the method to be adopted readily in real-life applications.

8.1.2 Image Interpolation

The image interpolation is formulated as a regularized least squares solution of a cost function in Chapter 5. The cost function consists of a data fidelity term and a *Tikhonov* regularization functional. It is processed as a whole matrix computation rather than pixel-to-pixel estimation individually. Because solving for the direct closed-form solution is impractical due to huge computational cost involved in large matrix inversion, we derive the optimal solution using a combined framework of Kronecker product and SVD to reduce the computational cost.

The regularized least squares can achieve a good trade-off between edge preservation and noise suppression. A key feature of the method is its computational efficiency in reconstructing high-fidelity HR image through clever manipulation of Kronecker product and SVD. This allows the new method to be employed readily in the areas of digital photography, computer vision, and medical imaging, among others.

8.1.3 Image Super-Resolution

The implementation of SR image reconstruction has been discussed in Chapter 6 and 7, focusing on image registration and multiframe reconstruction scheme.

The conventional registration techniques for rotation, translations and scaling are reviewed briefly. For subpixel registration, a major shortcoming of conventional spectrum technique is its sensitivity towards noise. A higher-order statistics method is proposed to estimate subpixel translations between two images. The new bispectrum algorithm utilizes the characteristics of bispectrum to suppress Gaussian noise. It is robust towards noise, thereby leading to significant performance improvements in low SNR environments or in the presence of cross-correlated channel noise.

A novel blind SR algorithm to enhance image resolution without the knowledge of the PSFs is developed. It is based on a new framework of joint interpolation-deconvolution scheme. It combines the advantages of PDR and MRF. The primary motivation for developing the blind algorithm is due to the observation that most existing SR methods assume the blurs are known *a priori*, which may not be true in many real-world applications. The main contribution is the development of multichannel blind deconvolution to estimate the unknown PSFs, and its integration into the SR scheme to render HR images.

8.2 Recommendations for Further Research

As medical imaging and surveillance systems are becoming more and more ubiquitously deployed, a critical need that has not been adequately addressed so far is to utilize the HR technology in these real-life applications. A new promising direction will be the development of more realistic observation models, more accurate degradation identification methods, and more powerful optimization frameworks with computational intelligence leading to ultimate improvements in reconstructed image quality.

8.2.1 High-Resolution Reconstruction for Color Image

Color images are typically expressed in multichannel models such as RGB (red, green, blue), HSI (hue, saturation, intensity), and $YCrCb$ (luminance, chrominance, chrominance). Among them, the RGB model is the most well-known color space, consisting of red, green, and blue channels. There are many practical factors that prevent accurate measurement of color images. For example, in single-chip CCD sensor array, color filter array (CFA) is commonly placed between the lens and the sensors for acquisition of color images [135], [136]. As CFA

has one color filter element for each sensor unit, this causes the captured image to have a mosaic pattern of observed pixels from different color channels. To render full-resolution images, the missing color information must be estimated from the surrounding pixels.

Color images can be considered as a special case of the multiple-input multiple-output (MIMO) model. However, the color channels are not independent but rather highly correlated. For example, a change of intensities in red channel usually corresponds to an edge in blue/green at the same location. Therefore, how to fully exploit this property for reconstructing a clearer and sharper HR image is of interest [137], [138].

Currently, there is relatively little work addressing color HR image reconstruction, and most common solutions involve applying monochrome deconvolution and SR to each color channel separately. However, the correlations between the color channels should be utilized during the reconstruction process. Bolmgren and Chan extend the TV norm to vector color images in order to achieve edge preservation and noise suppression [139]. Using the Beltrami framework, a color image can be considered as a 2-D surface embedded in a five-dimensional “spatial-feature”[140]. It is promising that if all color channels can be restored simultaneously via color image deconvolution [141], [142], the performance of the SR reconstruction scheme can be improved accordingly.

8.2.2 High-Resolution Reconstruction for Medical Imaging

In recent years, there are significant advances in the medical imaging ranging from the research laboratory to the clinical examination. However, efficient HR reconstruction softwares for medical imaging, including ultrasound, CT, MRI, x-ray, are still needed to facilitate the routine clinical imaging system [143]-[146]. For example, the major advantages of medical ultrasound imaging include the capability of real-time imaging, no radiation, and

usage of small, movable scanner. However, the commonly captured medical ultrasound images have much lower spatial resolution than the corresponding x-ray, CT, and MRI. Moreover, ultrasound images are degraded by speckle noise [147]. On the other hand, diagnostic decisions often require accurate measurements of organ volume. Unreliable volume measurement techniques may potentially lead to inaccurate decisions in diagnosis. Therefore, using computer to reconstruct a HR medical image by combining the available multiple degraded images is important. Its main goals are (i) image enhancement to increase image quality and to lessen the need for highly experienced doctors, and (ii) extraction of diagnostic information about tissue and incorporation of this information into automated diagnostic system.

8.2.3 Super-Resolution Considering Dynamic Scenes

Conventional SR algorithms are based on the model that there exist relative global motion between two consecutive images, including rotation and translations [148], [149]. This is applicable for the controlled camera where the scene is static and the movement of camera is well-defined [150]. However, there are relatively few works on spatial-temporal images observed in dynamic scenes. It is meaningful to discuss the SR when using a still camera to capture the dynamic object, especially in video surveillance applications [151], [152].

For dynamic scenes, motion object detection is necessary to detect the moving object of interest. For example, a human face tracker that can locate and segment the frontal face should be integrated in the face recognition system [153], [154]. It is useful for feature extraction of moving targets [155]. The assumption, which should be satisfied for dynamic scenes, is that all the changes that the moving object undergoes are rigid. Obviously, this assumption is more or less strictly valid for a surveillance video. Therefore, in some

surveillance applications dealing with human motion, manual selection is needed to pick out those most relevant frames for further processing.

8.3 Summary

In this thesis, we have developed a set of complete and efficient algorithms for HR image reconstruction. The algorithms presented here can serve as the foundation for further work. The future of high-resolution image reconstruction technology appears to be very bright, although much work remains to be done for it to reach a mature technology.

Author's Publications

Journal

- [1] Li Chen and Kim-Hui Yap, "Efficient discrete spatial techniques for blur support identification in blind image deconvolution," *IEEE Trans. Signal Processing*, vol. 54, no. 4, pp. 1557-1562, April 2006.
- [2] Li Chen and Kim-Hui Yap, "A soft double regularization approach to parametric blind image deconvolution," *IEEE Trans. Image Processing*, vol. 14, no. 5, pp. 624-633, May 2005.
- [3] Li Chen, Kim-Hui Yap, and Yu He, "Subband synthesis for color filter array demosaicking," Submitted to *IEEE Trans. Systems, Man, and Cybernetics, Part A: Systems and Humans*.
- [4] Li Chen and Kim-Hui Yap, "An effective bispectrum technique to subpixel image registration under noisy conditions," Submitted to *IEEE Trans. Systems, Man, and Cybernetics, Part A: Systems and Humans*.
- [5] Li Chen and Kim-Hui Yap, "An efficient regularization method for image interpolation using Kronecker product," Submitted to *IEEE Trans. Signal Processing*.
- [6] Li Chen, Kim-Hui Yap, and Yu He, "Efficient recursive multichannel blind image restoration," Submitted to *EURASIP Journal on Applied Signal Processing*.
- [7] Li Chen and Kim-Hui Yap, "Blind multiframe super-resolution image reconstruction," Submitted to *IEEE Trans. Image Processing*.

- [8] Yu He, Kim-Hui Yap, Li Chen, and Lap-Pui Chau, "A novel hybrid model framework to blind color image deconvolution," Submitted to *IEEE Trans. Systems, Man, and Cybernetics, Part B: Cybernetics*.

Conference

- [9] Yu He, Kim-Hui Yap, and Li Chen, and Lap-Pui Chau, "Blind super-resolution image reconstruction using a maximum a posteriori estimation," in *Proc. IEEE Int. Conf. Image Processing*, Atlanta, 2006.
- [10] Kim-Hui Yap and Li Chen, "A bispectrum technique to subpixel image registration under noisy conditions," accepted for publication in *Proc. IEEE Int. Conf. Acoustics, Speech, and Signal Processing*, Toulouse, France, 2006.
- [11] Li Chen and Kim-Hui Yap, "Regularized interpolation using Kronecker product for still images," in *Proc. IEEE Int. Conf. Image Processing*, Genova, Italy, pp. 1014-1017, Sept. 2005.
- [12] Li Chen, Kim-Hui Yap, and Yu He, "Color filter array demosaicking using wavelet-based subband synthesis," in *Proc. IEEE Int. Conf. Image Processing*, Genova, Italy, pp. 1002-1005, Sept. 2005.
- [13] Yu He, Kim-Hui Yap, and Li Chen, and Lap-Pui Chau, "Blind color image deconvolution based on wavelet decomposition," in *Proc. IEEE Int. Conf. Image Processing*, Genova, Italy, pp. 766-769, Sept. 2005.
- [14] Li Chen and Kim-Hui Yap, "Identification of blur support size in blind image deconvolution", in *Proc. Int. Conf. on Information, Communications and Signal Processing and Pacific-Rim Conference on Multimedia*, Singapore, vol. 1, pp.503-507, Dec. 2003.

- [15] Li Chen and Kim-Hui Yap, "A fuzzy k-nearest-neighbor algorithm to blind image deconvolution", in *Proc. IEEE Int. Conf. Systems, Man, and Cybernetics*, Washington D.C., pp. 2049-2054, Oct. 2003.

Bibliography

- [1] H. C. Andrews and B. R. Hunt, *Digital Image Restoration*. Upper Saddle River, NJ: Prentice-Hall, 1977.
- [2] M. R. Banham and A. K. Katsaggelos, "Digital image restoration," *IEEE Signal Processing Magazine*, vol. 14, no. 2, pp. 24-41, Mar. 1997.
- [3] R. L. Lagendijk and K. Biemond, *Iterative Identification and Restoration of Images*. Boston, MA: Kluwer, 1990.
- [4] D. Kundur and D. Hatzinakos, "Blind image deconvolution," *IEEE Signal Processing Magazine*, vol. 13, no. 3, pp. 43-64, May 1996.
- [5] [Online] <http://news.bbc.co.uk/1/hi/uk/4706421.stm>
- [6] G. Pavlović and A. M. Tekalp, "Maximum likelihood parametric blur identification based on a continuous spatial domain model," *IEEE Trans. Image Processing*, vol. 1, no. 4, pp. 496-504, Oct. 1992.
- [7] R. L. Lagendijk, J. Biemond, and D. E. Boekee, "Blur identification using the expectation maximization algorithm," in *Proc. IEEE Int. Conf. Acoustics, Speech, and Signal Processing*, pp. 1397-1400, 1989.
- [8] S. J. Reeves and R. M. Mersereau, "Blur identification by the method of generalized cross-validation," *IEEE Trans. Image Processing*, vol. 1, no. 3, pp. 301-311, July 1992.
- [9] A. E. Savakis and H. J. Trussell, "Blur identification by residual spectral matching," *IEEE Trans. Image Processing*, vol. 2, no. 2, pp. 141-151, Apr. 1993.

- [10] M. Cannon, "Blind deconvolution of spatially invariant image blurs with phase," *IEEE Trans. Acoustics, Speech, and Signal Processing*, vol. 24, no.1, pp. 58-63, Feb. 1976.
- [11] M. M. Chang, A. M. Tekalp, and A. T. Erdem, "Blur identification using the bispectrum," *IEEE Trans. Acoustics, Speech, and Signal Processing*, vol. 39, no. 10, pp. 2323-2325, Oct. 1991.
- [12] A. M. Tekalp, H. Kaufman, and J. W. Woods, "Identification of image and blur parameters in the restoration of noncausal blurs," *IEEE Trans. Acoustics, Speech, and Signal Processing*, vol. 34, no. 8, pp. 963-972, Aug. 1986.
- [13] Y. Yitzhaky and N. S. Kopeika, "Identification of blur parameters from motion blurred images," *CVGIP: Graphical Models and Image Processing*, vol. 59, no. 5, pp. 321-332, Sept. 1997.
- [14] Y. -L. You and M. Kaveh, "A regularization approach to joint blur identification and image restoration," *IEEE Trans. Image Processing*, vol. 5, no. 3, pp. 416-428, Mar. 1996.
- [15] A. K. Jain, "Advances in mathematical models for image processing," *Proceedings of the IEEE*, vol. 69, no. 5, pp. 502-528, May 1981.
- [16] J. W. Woods, "Markov image modeling," *IEEE Trans. Automat. Contr.*, vol. 23, pp. 846-850, Oct. 1978.
- [17] R. Kashyap, "Characterization and estimation of two-dimensional ARMA models," *IEEE Trans. Information Theory*, vol. 30, no. 5, pp. 736-745, Oct. 1984.
- [18] A. Graham, *Kronecker Products and Matrix Calculus With Applications*. NY: J. Wiley and Sons, 1981.
- [19] J. Kamm and J. G. Nagy, "Kronecker product and SVD approximations in image restoration," *Linear Algebra Appl.*, vol. 284, pp. 177-192, 1998.

- [20] G. Jacovitti and R. Cusani, "An efficient technique for high correlation estimation," *IEEE Trans. Acoustics, Speech, and Signal Processing*, vol. 35, no.5, pp. 654-660, May 1987.
- [21] S. M. Kay, *Fundamentals of Statistical Signal Processing: Estimation Theory*. Upper Saddle River, NJ: Prentice-Hall, 1993.
- [22] P. C. Hansen, "Analysis of discrete ill-posed problems by means of the L-curve", *SIAM Review*, vol. 34, no. 4, pp. 561-580, Dec. 1992.
- [23] K. T. Lay and A. K. Katsaggelos, "Image identification and restoration based on expectation-maximization algorithm," *Opt. Eng.*, vol. 29, no. 5, pp. 436-445, May 1990.
- [24] G. R. Ayers and J. C. Dainty, "Iterative blind image deconvolution method and its applications," *Optics Letters*, vol. 13, pp. 547-549, July 1988.
- [25] D. Kundur and D. Hatzinakos, "A novel blind deconvolution scheme for image deconvolution using recursive filtering," *IEEE Trans. Signal Processing*, vol. 46, no. 2, pp. 375-390, Feb. 1998.
- [26] C. A. Ong and J. A. Chambers, "An enhanced NAS-RIF algorithm for blind image deconvolution," *IEEE Trans. Image Processing*, vol. 8, no. 7, pp. 988-992, July 1999.
- [27] M. K. Ng, R. J. Plemmons, and S. Qiao, "Regularization of RIF blind image deconvolution," *IEEE Trans. Image Processing*, vol. 9, no. 6, pp. 1130-1134, June 2000.
- [28] A. K. Katsaggelos, J. Biemond, R. W. Mersereau, and R.W. Schaefer, "Nonstationary iterative image deconvolution," in *Proc. IEEE Int. Conf. Acoustics, Speech, and Signal Processing*, pp. 696-699, 1985.
- [29] —, "A regularized iterative image restoration algorithm," *IEEE Trans. Signal Processing*, vol. 39, no. 4, 914-929, Apr.1991.
- [30] R. G. Lane, "Blind deconvolution of speckle images," *Journal of the Optical Society of America A*, vol. 9, no. 9, pp. 1508-1514, Sept. 1992.

- [31] Y. Yang, N. P. Galatsanos, and H. Stark, "Projection based blind deconvolution," *Journal of the Optical Society of America A*, vol. 11, no. 9, pp. 2401-2409, Sept. 1994.
- [32] Y. -L. You and M. Kaveh, "Blind image restoration by anisotropic regularization," *IEEE Trans. Image Processing*, vol. 8, no. 3, pp. 396-407, Mar. 1999.
- [33] L. Rudin, S. Osher, and E. Fatemi, "Nonlinear total variation based noise removal algorithms," *Physica D*, vol. 60, pp. 259-258, 1992.
- [34] C. R. Vogel and M. E. Oman, "Fast, robust total variation-based reconstruction of noisy, blurred images," *IEEE Trans. Image Processing*, vol. 7, no. 6, pp. 813-824, Jun. 1998.
- [35] T. F. Chan and C. -K. Wong, "Total variation blind deconvolution," *IEEE Trans. Image Processing*, vol. 7, no. 5, pp. 370-375, Mar. 1998.
- [36] Y. -T. Zhou, R. Chellappa, A. Vaid, and B. K. Jenkins, "Image restoration using a neural network," *IEEE Trans. Acoustics, Speech, and Signal Processing*, vol. 36, no. 7, pp. 1141-1151, July 1988.
- [37] J. K. Paik and A. K. Katsaggelos, "Image restoration using a modified Hopfield network," *IEEE Trans. Image Processing*, vol. 1, no. 1, pp. 49-63, Jan 1992.
- [38] L. Guan, J. A. Anderson, and J. P. Sutton, "A network of networks processing models for image regularization," *IEEE Trans. Neural Networks*, vol. 8, no. 1, pp. 169-174, Jan. 1997.
- [39] S. W. Perry and L. Guan, "Weight assignment for adaptive image restoration by neural networks," *IEEE Trans. Neural Networks*, vol. 11, no. 1, pp. 156-170, Jan. 2000.
- [40] K. -H. Yap, L. Guan and W. Liu, "A recursive soft-decision approach to blind image deconvolution," *IEEE Trans. Signal Processing*, vol. 51, no. 2, pp. 515-526, Feb. 2003.
- [41] K. -H. Yap, and L. Guan, "A computational reinforced learning scheme to blind image deconvolution," *IEEE Trans. Evolutionary Computation*, vol. 6, no. 1, pp. 2-15, Feb. 2002.

- [42] J. M. Keller, M. R. Gray and J. A. Givens Jr., "A fuzzy k -nearest neighbor algorithm," *IEEE Trans. Systems, Man and Cybernetics*, vol. 15, no. 4, 580-585, Apr. 1985.
- [43] N. Zahid, O. Abouelala, M. Limouri and A. Essaid, "Fuzzy clustering based on k -nearest-neighbours rule," *Fuzzy Sets and Systems*, vol. 120, no. 2, pp. 239-247, Jun. 2001.
- [44] K. Hattori and M. Takahashi, "A new nearest-neighbor rule in the pattern classification problem," *Pattern Recognition*, vol. 32, no.3, pp. 425-432, Mar. 1999.
- [45] R. W. Hamming, *Digital Filters*. Upper Saddle River, NJ: Prentice-Hall, 1989.
- [46] T. F. Chan and C. -K. Wong, "Convergence of the alternating minimization algorithm for blind deconvolution," *Linear Algebra Appl.*, vol. 316, pp. 259-285, Sept. 2000.
- [47] J. B. Hiriart-Urruty and C. Lemarecal, *Convex Analysis and Minimization Algorithms I*. New York: Springer-Verlag, 1993.
- [48] M. T. Heath, *Scientific Computing: An Introductory Survey*, 2nd Edition, NY: McGraw-Hill, 2002.
- [49] B. P. Hunt and O. Kubler, "Karhunen-Loeve multispectral image deconvolution, part I: theory," *IEEE Trans. Acoustics, Speech, and Signal Processing*, vol. 32, no. 3, pp.592-600, June 1984.
- [50] N. P. Galatsanos and R. T. Chin, "Digital restoration of multichannel images," *IEEE Trans. Acoustics, Speech, and Signal Processing*, vol. 37, no. 3, pp. 415-421, March 1989.
- [51] G. Angelopoulos and I. Pitas, "Multichannel Wiener filters in color image restoration," *IEEE Trans. Circuits and Systems for Video Technology*, vol. 4, no. 1, pp. 83-87, Feb. 1995.

- [52] N. P. Galatsanos, A. K. Katsaggelos, R.T. Chin, and A.D. Hillery, "Least squares restoration of multichannel images," *IEEE Trans. Signal Processing*, vol. 39, no. 10, pp. 2222-2236, Oct. 1991.
- [53] M. G. Kang and A. K. Katsaggelos, "Simultaneous multichannel image restoration and estimation of the regularization parameters," *IEEE Trans. Image Processing*, vol. 6, no. 5, pp. 774-778, May. 1997.
- [54] Y. P. Guo, H. P. Lee, and C. L. Teo, "Multichannel image restoration using an iterative algorithm in space domain," *Image and Vision Computing*, vol. 14, no. 6, pp. 389-400, 1996.
- [55] M. G. Kang, "Generalized multichannel image deconvolution approach and its applications," *Opt. Eng.*, vol. 37, no. 11, pp. 2953-2964, 1998.
- [56] R. Molina and J. Mateos, "Multichannel image restoration in Astronomy," *Vistas in Astronomy*, vol. 41, no. 3, pp. 373-379, 1997.
- [57] R. R. Schultz and R. L. Stevenson, "Stochastic modeling and estimation of multispectral image data," *IEEE Trans. Image Processing*, vol. 4, no. 8, pp. 1109-1119, Aug. 1995.
- [58] S. U. Pillai and B. Liang, "Blind image restoration using a robust GCD approach," *IEEE Trans. Image Processing*, vol. 8, no. 2, pp. 295-301, Feb. 1999.
- [59] G. Harikumar and Y. Bresler, "Perfect blind restoration of images blurred by multiple filters: theory and efficient algorithms," *IEEE Trans. Image Processing*, vol. 8, no. 2, pp. 202-219, Feb. 1999.
- [60] G. B. Giannakis and R. W. Heath, "Blind identification of multichannel FIR blurs and perfect image deconvolution," *IEEE Trans. Image Processing*, vol. 9, no. 11, pp. 1877-1896, Nov. 2000.
- [61] H. T. Pai and A. C. Bovik, "On eigenstructure-based direct multichannel blind image restoration," *IEEE Trans. Image Processing*, vol. 10, no. 10, pp. 1434-1446, Oct. 2001.

- [62] T. W. S. Chow, X. -D. Li, and K.-T. Ng, "Double-regularization approach for blind restoration of multichannel imagery," *IEEE Trans. Circuits and Systems I: Fundamental Theory and Applications*, vol. 48, no. 9, pp. 1075-1085, Sept. 2001.
- [63] R. Molina, J. Mateos, A. K. Katsaggelos, and M. Vega, "Bayesian multichannel image restoration using compound Gauss-Markov random fields," *IEEE Trans. Image Processing*, vol. 12, no. 12, pp. 1642-1654, Dec. 2003.
- [64] F. Sroubek and J. Flusser, "Multichannel blind iterative image restoration," *IEEE Trans. Image Processing*, vol. 12, no. 9, pp. 1094-1106, Sept. 2003.
- [65] G. Panci, P. Campisi, S. Colonnese, and G. Scarano, "Multichannel blind image deconvolution using the Bussgang algorithm: spatial and multiresolution approaches," *IEEE Trans. Image Processing*, vol. 12, no. 11, pp. 1324-1336, Nov. 2003.
- [66] S. Haykin, *Adaptive Filter Theory*, 4th Edition, Upper Saddle River, NJ: Prentice-Hall, 2002.
- [67] N. P. Galatsanos and A. K. Katsaggelos, "Methods for choosing the regularization parameter and estimating the noise variance in image restoration and their relation," *IEEE Trans. Image Processing*, vol. 1, no. 3, pp. 322-336, July 1992.
- [68] G. H. Golub and C. F. Van Loan, *Matrix Computations*, 3rd Edition, MD: Johns Hopkins University Press, 1996.
- [69] K. R. Castleman, *Digital Image Processing*. Upper Saddle River, NJ: Prentice-Hall, 1996.
- [70] T. M. Lehmann, C. Gonner, and K. Spitzer, "Survey: interpolation methods in medical image processing," *IEEE Trans. Medical Imaging*, vol. 18, no. 11, pp. 10490-1074, Nov. 1999.
- [71] T. Blu, P. Thevenaz, and M. Unser, "Linear interpolation revitalized," *IEEE Trans. Image Processing*, vol. 13, no. 5, pp. 710-719, May 2004.

- [72] H. S. Hou and H. C. Andrews, "Cubic splines for image interpolation and digital filtering," *IEEE Trans. Acoustics, Speech, and Signal Processing*, vol. 26, no. 6, pp. 508-517, Dec. 1978.
- [73] A. Munoz, T. Blu, and M. Unser, "Least-squares image resizing using finite difference," *IEEE Trans. Image Processing*, vol. 10, no. 9, pp. 1365-1378, Sept. 2001.
- [74] J. W. Hwang and H. S. Lee, "Adaptive image interpolation based on local gradient features," *IEEE Signal Processing Letters*, vol. 11, no. 3, pp. 359-362, Mar. 2004.
- [75] G. Ramponi, "Warped distance for space-variant linear image interpolation," *IEEE Trans. Image Processing*, vol. 8, no. 5, pp. 629-639, May 1999.
- [76] K. P. Hong, J. K. Paik, H. J. Kim, and C. H. Lee, "An edge-preserving image interpolation system for a digital camcorder," *IEEE Trans. Consumer Electronics*, vol. 42, no.3, pp. 279-284, Aug. 1996.
- [77] X. Li and M. T. Orchard, "New edge-directed interpolation," *IEEE Trans. Image Processing*, vol. 10, no. 10, pp. 1521-1527, Oct. 2001.
- [78] W. K. Carey, D. B. Chuang, and S. S. Hemami, "Regularity-preserving image interpolation," *IEEE Trans. Image Processing*, vol. 8, no. 9, pp. 1293-1297, Sept. 1999.
- [79] R. Chan, T. Chan, L. Shen, and Z. -W. Shen, "Wavelet algorithms for high-resolution image reconstruction," *SIAM Journal on Scientific Computing*, vol. 24, no. 4, pp. 1408-1432, Apr. 2003.
- [80] P. -S. Tsai, T. Acharya, and A. K. Ray, "Adaptive fuzzy color interpolation," *Journal of Electronic Imaging*, vol. 11, no. 3, pp. 293-305, July 2002.
- [81] G. Chen and R. J. P. de Figueiredo, "A unified approach to optimal image interpolation problems based on linear partial differential equation models," *IEEE Trans. Image Processing*, vol. 2, no. 1, pp. 41-49, Jan. 1993.

- [82] D. D. Muresan and T. W. Parks, "Adaptive quadratic (aqua) image interpolation," *IEEE Trans. Image Processing*, vol. 13, no. 5, pp. 690-698, May 2004.
- [83] L. G. Brown, "A survey of image registration techniques," *ACM Computing Surveys*, vol. 24, no. 4, pp. 325-376, Dec. 1992.
- [84] B. Zitova and J. Flusser, "Image registration methods: a survey," *Image and Vision Computing*, vol. 21, no. 11, pp. 977-1000, Nov. 2003.
- [85] S. Ranade and A. Rosenfeld, "Point pattern matching by relaxation," *Pattern Recognition*, vol. 12, no. 4, pp. 269-275, 1980.
- [86] H. S. Alhichri and M. Kamel, "Virtual circles: a new set of features for fast image registration," *Pattern Recognition Letters*, vol. 24, no. 9-10, pp. 1181-1190, June 2003.
- [87] B. Lucas and T. Kanade, "An iterative image registration technique with an application to stereo vision," in *Proc. DARPA Image Understanding Workshop*, pp. 121-130, Apr. 1981.
- [88] B. K. P. Horn and B. G. Schunck, "Determining optical flow," *Artificial Intelligence*, vol. 17, no. 1, pp. 185-203, Aug. 1981.
- [89] C. D. Kuglin and D. C. Hines, "The phase correlation image alignment method," in *Proc. IEEE Int. Conf. Cybernetics and Society*, pp. 163-165, Sept. 1975.
- [90] B. S. Reddy and B. N. Chatterji, "An FFT-based technique for translations, rotation, and scale-invariant image registration," *IEEE Trans. Image Processing*, vol. 5, no. 8, pp. 1266-1271, Aug. 1996.
- [91] Y. Keller, A. Averbuch, and M. Israeli, "Pseudopolar-based estimation of large translations, rotations, and scalings in images," *IEEE Trans. Image Processing*, vol. 14, no. 1, pp. 12-22, Jan. 2005.

- [92] L. Lucchese and G. M. Gortelazzo, "A noise robust frequency domain technique for estimating planar roto-translations," *IEEE Trans. Signal Processing*, vol. 48, no.6, pp. 1769-1786, June 2000.
- [93] D. I. Barnea and H. F. Silverman, "A class of algorithms for fast digital image registration," *IEEE Trans. Computers*, vol. 21, no. 2, pp. 179-186, 1972.
- [94] S. Borman, M. A. Robertson, and R. L. Stevenson, "Block-matching sub-pixel motion estimation from noisy, under-sampled frames-An empirical performance evaluation," *Visual Communications and Image Processing*, San Jose, CA, SPIE vol. 3653, pp. 1442-1451, 1999.
- [95] P. Thévenaz, U. E. Ruttimann, and M. Unser, "A pyramid approach to subpixel registration based on intensity," *IEEE Trans. Image Processing*, vol. 7, no. 1, pp. 27-41, Jan. 1998.
- [96] I. J. Cox, J. B. Kruskal, and D. A. Wallach, "Prediction and estimation the accuracy of a subpixel registration algorithm," *IEEE Trans. Pattern Analysis and Machine Intelligence*, vol. 12, no. 8, pp. 721-733, Aug. 1990.
- [97] S. Cain, M. Hayat, and E. Armstrong, "Projection-based image registration in the presence of fixed-pattern noise," *IEEE Trans. Image Processing*, vol. 10, no. 12, pp. 1860-1872, Dec. 2001.
- [98] V. Argyriou and T. Vlachos, "Using gradient correlation for sub-pixel motion estimation of video sequences", in *Proc. IEEE Int. Conf. Acoustics, Speech, and Signal Processing*, vol. 3, pp. 329-332, 2004.
- [99] Y. Keller and A. Averbuch, "Fast motion estimation using bidirectional gradient," *IEEE Trans. Image Processing*, vol. 13, no. 8, pp. 1042-1054, Aug. 2004.

- [100] H. S. Stone, M. T. Orchard, E. -C. Chang, and S. A. Martucci, "A fast direct Fourier-based algorithm for subpixel registration of images," *IEEE Trans. Geoscience and Remote Sensing*, vol. 39, no. 10, pp. 2235-2243, Oct. 2001.
- [101] S. P. Kim and W. Y. Su, "Subpixel accuracy image registration by spectrum cancellation," in *Proc. IEEE Int. Conf. Acoustics, Speech and Signal Processing*, pp. 153-156, Apr. 1993.
- [102] H. Foroosh, J. B. Zerubia, and M. Berthod, "Extension of phase correlation to subpixel registration," *IEEE Trans. Image Processing*, vol. 11, no. 3, pp. 188-200, Mar. 2002.
- [103] W. S. Hoge and C.-F. Westin, "Identification of translational displacements between N-dimensional data sets using the high order SVD and phase correlation," *IEEE Trans. on Image Processing*, vol. 14, no.7, pp.884-889, July, 2005.
- [104] D. Robinson and P. Milanfar, "Fundamental performance limits in image registration," *IEEE Trans. Image Processing*, vol. 13, no. 9, pp. 1185-1199, Sept. 2004.
- [105] J. M. M. Anderson and G. B. Giannakis, "Image motion estimation algorithms using cumulants," *IEEE Trans. Image Processing*, vol. 4, no. 3, pp. 346-357, Mar. 1995.
- [106] C. L. Nikias and A. P. Petropulu, *Higher-Order Spectral Analysis: A Nonlinear Signal Processing Framework*. Upper Saddle River, NJ: Prentice-Hall, 1993.
- [107] M. J. Hinich and G. R. Wilson, "Time delay estimation using the cross bispectrum," *IEEE Trans. Signal Processing*, vol. 40, no. 11, pp. 106-113, Jan. 1992.
- [108] S. Borman and R. L. Stevenson, "Spatial resolution enhancement of low-resolution image sequences a comprehensive review with directions for future research," *Technical Report*, Department of Electrical Engineering, University of Notre Dame, USA, July 1998.
- [109] S. C. Park, M. K. Park, and M. G. Kang, "Super-resolution image reconstruction: a technical overview," *IEEE Signal Processing Magazine*, vol. 20, pp. 21-36, May 2003.

- [110] M. K. Ng and N. K. Bose, "Mathematical analysis of super-resolution methodology," *IEEE Signal Processing Magazine*, vol. 20, no. 3, pp. 62-74, May 2003.
- [111] D. Capel and A. Zisserman, "Computer vision applied to super resolution," *IEEE Signal Processing Magazine*, vol. 20, no. 3, pp. 75-86, May 2003.
- [112] [Online] <http://www.salientstills.com/>
- [113] [Online] <http://www.qelabs.com/>
- [114] [Online] <http://www.cognithech.com/>
- [115] R. Y. Tsai and T. S. Huang, "Multiframe image restoration and registration," in *Advances in Computer Vision and Image Processing*, T. S. Huang, Eds., vol. 1, pp. 317-339. CT: JAI Press, 1984.
- [116] S. P. Kim, N.K. Bose, and H. M. Valenzuela, "Recursive reconstruction of high resolution image from noisy undersampled multiframes," *IEEE Trans. Acoustics, Speech, and Signal Processing*, vol. 38, no. 6, pp. 1013-1027, June 1990.
- [117] S. P. Kim and W. -Y. Su, "Recursive high-resolution reconstruction of blurred multiframe images," *IEEE Transactions on Image Processing*, vol. 2, pp. 534-539, Oct. 1993.
- [118] D. Keren, S. Peleg, and R. Brada, "Image sequence enhancement using subpixel displacements," in *Proc. IEEE Int. Conf. Computer Vision and Pattern Recognition*, pp. 742-746, June 1988.
- [119] M. Irani and S. Peleg, "Motion analysis for image enhancement: resolution, occlusion, and transparency," *Journal of Visual Communications and Image Representation*, vol. 4, no. 4, pp. 324-335, Dec. 1993.
- [120] H. Stark and P. Oskoui, "High-resolution image recovery from image-plane arrays, using convex projections," *Journal of the Optical Society of America A*, vol. 6, no. 11, pp. 1715-1726, Nov. 1989.

- [121] A. M. Tekalp, M. K. Ozkan, and M. I. Sezan, "High-resolution image reconstruction from lower-resolution image sequences and space-varying image restoration," in *Proc. IEEE Int. Conf. Acoustics, Speech, and Signal Processing*, San Francisco, vol. 3, pp.169-172, Mar. 1992.
- [122] A. J. Patti and Y. Altunbasak, "Artifact reduction for set theoretic super resolution image reconstruction with edge adaptive constraints and higher-order interpolants," *IEEE Trans. Image Processing*, vol. 10, no. 1 pp. 179-186, Jan. 2001.
- [123] E. S. Lee and M. G. Kang, "Regularized adaptive high-resolution image reconstruction considering inaccurate subpixel registration," *IEEE Trans. Image Processing*, vol. 12, no. 7, pp. 826-837, July 2003.
- [124] R. R. Schultz and R. L. Stevenson, "Improved definition image expansion," in *Proc. IEEE Int. Conf. Acoustics, Speech and Signal Processing*, San Francisco, CA, vol. 3, pp. 173-176, Mar. 1992.
- [125] —, "A Bayesian approach to image expansion for improved definition," *IEEE Transactions on Image Processing*, vol. 3, no. 3, pp. 233-242, May 1994.
- [126] C. A. Segall, A. K. Katsaggelos, and R. Molina, "High-resolution images from low-resolution compressed video," *IEEE Signal Processing Magazine*, vol. 20, no. 3, pp. 37-48, May 2003.
- [127] C. A. Segall, A. K. Katsaggelos, R. Molina, and J. Mateos, "Bayesian resolution enhancement of compressed video," *IEEE Trans. Image Processing*, vol. 13, no. 7, pp. 898-911, July 2004.
- [128] F. M. Candocia and J. C. Principe, "Super-resolution of images based on local correlations," *IEEE Trans. Neural Networks*, vol. 10, no. 2, pp.372-380, Mar. 1999.
- [129] W. T. Freeman, T. R. Jones, and E. C. Pasztor, "Example-based super-resolution," *IEEE Trans. Computer Graphics and Applications*, vol. 22, no. 2, pp. 56-65, Mar. 2002.

- [130] M. Elad and Y. Hel-Or, "A fast super-resolution reconstruction algorithm for pure translational motion and common space-invariant blur," *IEEE Trans. Image Processing*, vol. 10, no. 8, pp. 1187-1193, Aug. 2001.
- [131] S. Farsiu, M. D. Robinson, M. Elad, and P. Milanfar, "Fast and robust multiframe super resolution," *IEEE Trans. Image Processing*, vol. 13, no. 10, pp. 1327-1344, Oct. 2004.
- [132] S. Lertrattanapanich and N. K. Bose, "High resolution image formation from low resolution frames using Delaunay triangulation," *IEEE Trans. Image Processing*, vol. 11, no. 12, pp. 1427-1441, Dec. 2002.
- [133] N. Nguyen, P. Milanfar, and G. Golub, "Efficient generalized cross-validation with applications to parametric image restoration and resolution enhancement," *IEEE Trans. Image Processing*, vol. 10, no. 9, pp. 1299-1308, Sept. 2001.
- [134] P. Vandewalle, S. Süssstrunk, and M. Vetterli, "A frequency domain approach to registration of aliased images with application to super-resolution," *EURASIP Journal on Applied Signal Processing (Special Issue on Super-Resolution)*, 2005.
- [135] B. Gunturk, Y. Altunbasak, and R. M. Merserea, "Color plane interpolation using alternating projections," *IEEE Trans. Image Processing*, vol. 11, pp. 997-1013, Sept. 2002.
- [136] W. Lu and Y. -P Tan, "Color filter array demosaicking: new method and performance measures," *IEEE Trans. Image Processing*, vol. 12, no. 10, pp. 1194-1210, Oct. 2003.
- [137] H. Altunbasak and H. J. Trussell, "Colorimetric restoration of digital images," *IEEE Trans. Image Processing*, vol. 10, no. 3, pp. 393-402, Mar. 2001.
- [138] J. Bescos and J. H. Altamirano, "Digital restoration models for color imaging," *Applied Optics*, vol. 27, no. 2, pp. 419-425, Jan. 1988.
- [139] P. Blomgren and T. F. Chan, "Color TV: Total variation methods for restoration of vector valued images," *IEEE Trans. Image Processing*, vol. 7, pp. 304-309, Mar. 1998.

- [140] R. Kimmel, R. Malladi, and N. Sochen, "Images as embedding maps and minimal surfaces: movies, color, and volumetric medical images," in *Proc. IEEE Int. Conf. Computer Vision and Pattern Recognition*, pp. 350-355, June 1997.
- [141] B. C. Tom and A. Katsaggelos, "Resolution enhancement of monochrome and color video using motion compensation," *IEEE Trans. Image Processing*, vol. 10, no. 2, pp. 278-287, Feb. 2001.
- [142] N. R. Shah and A. Zakhori, "Resolution enhancement of color video sequences," *IEEE Trans. Image Processing*, vol. 8, no. 6, pp. 879-885, June 1999.
- [143] Y. Murakami, A. Takahashi, and S. Terashima, "Magnetic super-resolution," *IEEE Trans. Magnetics*, vol. 31, no. 6, pp. 3215-3220, Nov. 1995.
- [144] G. Wang, M. W. Vannier, M. W. Skinner, M. G. P. Cavalcanti, and G. W. Harding, "Spiral CT image deblurring for cochlear implantation," *IEEE Trans. Medical Imaging*, vol. 17, no. 2, pp. 251-262, Apr. 1998.
- [145] H. Greenspan, G. Oz, N. Kiryati, and S. Peled, "MRI inter-slice reconstruction using super-resolution," *Magnetic Resonance Imaging*, vol. 20, no. 5, pp. 437-446, June 2002.
- [146] P. Barone and G. Sebastiani, "A new method of magnetic resonance image reconstruction with short acquisition time and truncation artifact reduction," *IEEE Trans. Medical Imaging*, vol. 11, no. 2, pp. 250-259, June 1992.
- [147] T. Taxt and R. Jirik, "Superresolution of ultrasound images using the first and second harmonic signal," *IEEE Trans. Ultrasonic, Ferroelectrics, and Frequency Control*, vol. 51, no. 2, pp. 163-175, Feb. 2004.
- [148] Y. Altunbasak, A. J. Patti, and R. M. Mersereau, "Super-resolution still and video reconstruction from MPEG-coded video," *IEEE Trans. Circuits and Systems for Video Technology*, vol. 10, no. 4, pp. 217-226, Apr. 2002.

- [149] M. Elad and A. Feuer, "Super-resolution reconstruction of image sequences," *IEEE Trans. Pattern Analysis and Machine Intelligence*, vol. 21, no. 9, pp.817-834, Sept. 1999.
- [150] M. Ben-Ezra, A. Zomet, and S. K. Nayar, "Video super-resolution using controlled subpixel detector shifts," *IEEE Trans. Pattern Analysis and Machine Intelligence*, vol. 27, no. 6, pp. 977-987, June 2005.
- [151] E. Shechtman, Y. Caspi, and M. Irani, "Space-time super-resolution," *IEEE Trans. Pattern Analysis and Machine Intelligence*, vol. 27, no. 4, pp. 531-545, Apr. 2005.
- [152] S. Chaudhuri and D. R. Taur, "High-resolution slow-motion sequencing: how to generate a slow-motion sequence from a bit stream," *IEEE Signal Processing Magazine*, vol. 22, no. 2, pp. 16-24, May 2005.
- [153] S. Baker and T. Kanade, "Limits on super-resolution and how to break them," *IEEE Trans. Pattern Analysis and Machine Intelligence*, vol. 24, no. 9, pp. 1167-1183, Sept. 2002.
- [154] B. K. Gunturk, A. U. Batur, Y. Altunbasak, M. H. Hayes, and R. M. Mersereau, "Eigenface-domain super-resolution for face recognition," *IEEE Trans. Image Processing*, vol. 12, no. 5, pp. 597-606, May 2001.
- [155] N. Z. Jiang, R. B. Wu, and J. Li, "Super resolution feature extraction of moving targets," *IEEE Trans. Aerospace and Electronic Systems*, vol. 37, no. 3, pp.781-793, July 2001.